

AMERICAN UNIVERSITY OF BEIRUT

INTELLIGENT ENERGY MANAGEMENT
SYSTEM FOR HYBRID ELECTRIC
VEHICLES

by

DIMA AMINE FARES

A dissertation
submitted in partial fulfillment of the requirements
for the degree of Doctor of Philosophy
to the Department of Electrical and Computer Engineering
of the Faculty of Engineering and Architecture
at the American University of Beirut

Beirut, Lebanon
February 2015

AMERICAN UNIVERSITY OF BEIRUT

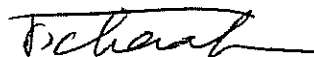
INTELLIGENT ENERGY MANAGEMENT
SYSTEM FOR HYBRID ELECTRIC
VEHICLES

by
DIMA AMINE FARES

Approved by:

Dr. Farid Chaaban, Professor
Electrical and Computer Engineering

Chair of Committee



Dr. Riad Chedid, Professor
Electrical and Computer Engineering

Advisor



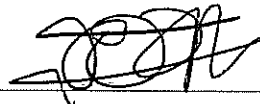
Dr. Sami Karaki, Professor
Electrical and Computer Engineering

Member of Committee



Dr. Rabih Jabr, Professor
Electrical and Computer Engineering

Member of Committee



Dr. Ferdinand Panik, Professor
Univeristy of Applied Sciences, Esslingen, Germany

Member of Committee

9/6 

Dr. Hugo Gabele, Assistant Professor

Member of Committee

University of Applied Sciences, Esslingen, Germany

40 

Date of dissertation defense: February 5th, 2015

AMERICAN UNIVERSITY OF BEIRUT

THESIS, DISSERTATION, PROJECT RELEASE FORM

Student Name: $\frac{\text{FARES}}{\text{Last}} \quad \frac{\text{DIMA}}{\text{First}} \quad \frac{\text{AMINE}}{\text{Middle}}$

Masters Thesis Masters Project Doctoral Dissertation

I authorize the American University of Beirut to: (a) reproduce hard or electronic copies of my thesis, dissertation, or project; (b) include such copies in the archives and digital repositories of the University; and (c) make freely available such copies to third parties for research or educational purposes.

I authorize the American University of Beirut, **three years after the date of submitting my thesis, dissertation, or project**, to: (a) reproduce hard or electronic copies of it; (b) include such copies in the archives and digital repositories of the University; and (c) make freely available such copies to third parties for research or educational purposes.

Signature

Date

Dedicate to my mother Iman, whose love and support helped me finish this
dissertation

Acknowledgements

I would like to thank my advisor Prof. Riad Chedid for helping me throughout the thesis work and providing me with his knowledge and expertise to complete the dissertation. I would also like to thank my co-advisor Prof. Ferdinand Panik from the university of applied sciences in Germany who added to my knowledge in the vehicle electrification field and who provided all resources needed to complete the work. I would like to thank my committee members Prof. Farid Chaaban, Prof. Sami Karaki and Prof. Rabih Jabr.

I would like to thank my hidden soldiers in the ECE department for their continuous support, Mrs. Rabab Abi Shakra and Mr. Khaled Joujou. Special thanks to my friends Lise, Zareh, Ahmad, Manal, Rawad and Jihad.

I would like to thank my family, my inlaws Farouk and Samar, my sister in law Rima and my brother Bilal.

Thanks to my husband Kareem who supported me and bore with me and handled my meltdowns. I could not have done it without him. Thanks to my daughter Vera who gave me the warmest hugs when I needed them.

Last but not least, I would like to thank my mother Iman, who believed in me from the first day, who raised me and nurtured me to be the person I am today. I owe everything to her and this dissertation is dedicated to her.

An Abstract of the Dissertation of

Dima Amine Fares for Doctor of Philosophy
Major: Electrical and Computer Engineering

Title: Intelligent Energy Management System for Hybrid Electric Vehicles

Hybrid electric vehicles positively influence the transportation industry with regards to reducing the use of fossil fuels and minimizing emissions. A class of such vehicles incorporates fuel cells and energy storage systems as alternatives to the internal combustion engines. The energy management system in these vehicles locates the power split between the available sources while adhering to operational and component requirements. This dissertation develops an efficient energy management system for fuel cell hybrid vehicles for the purpose of achieving a sub-optimal power allocation between the energy sources while adhering to component requirements and maintaining the required operational performance. A power train configuration model based on a Simulink model of the electric vehicle is used for testing the energy management system.

The dissertation addresses two stage control methodologies, pre-driving off-line optimization using an improved dynamic programming algorithm and on-line optimization using PID controller. In the first stage, the optimization strategies depend on the degree of knowledge of the driving cycle. If the cycle is known before hand, then the improved dynamic programming technique is used to find the sub-optimum power allocation for the whole cycle. Weighted improved dynamic programming algorithm analyses the effect of changing the relative cost of the battery with respect to the fuel cell. Stochastic estimation of the driving cycle is adopted if apriori knowledge of the cycle is not accurately known. On-line optimization is performed using a complete Simulink designed model of the fuel cell hybrid vehicle. The numerical outcomes of the off-line optimization are used to test the efficiency of the improved dynamic programming algorithm in lowering operational cost while ensuring drivability. PID controller is used to minimize

the error between the actual and the approximated vehicle speeds during on-line optimization.

A looped improved dynamic programming technique is tested during on-line operation, to tweak deviations from pre-set cycles by updating the optimal power allocation matrix during the trip and to cater for special events. The performance criteria are based on the overall operational cost as well as the hydrogen consumption per trip when compared to an existing state machine rule based method. Moreover, battery state of charge and system efficiencies are also measured and analyzed.

Contents

Contents	ix
List of Figures	xii
List of Tables	xv
1 Introduction	1
1.1 Optimum Power Allocation in FCHV	2
1.1.1 Rule Based Energy Management Systems	3
1.1.2 Adaptive Control	4
1.1.3 Optimization based Energy management systems	4
1.2 Thesis Contribution	7
1.3 Organization of the Dissertation	9
1.4 Abbreviations	9
2 Modeling the FCHV PowerTrain	10
2.1 Fuel Cell System Modeling	13
2.1.1 Fuel Cell Dynamic Model	15
2.1.2 Fuel Cell Simulink Model	15
2.2 Battery System	18
2.2.1 Battery Control System	19
2.2.2 Battery Simulink Model	20
2.2.3 Drivers Model Subsystems	25
2.3 Vehicle Dynamics Subsystem	26
2.3.1 Vehicle-Driving Resistance	27
2.3.2 Vehicle-Braking Force	28
2.3.3 Vehicle-Traction Force	28
2.4 Electric Motor	28
2.5 The Transmission System Unit	29
2.6 Auxiliaries	31
2.7 The Power Conditioning System Block	31
2.8 The Energy Management System Block	31
2.9 Summary	33

3	Efficient Energy Management System	35
3.1	Approximation of the Off-line Power Demand	36
3.1.1	FC System Characteristics	38
3.1.2	Battery Storage System Characteristics	40
3.2	Linear Programming	42
3.2.1	System Constraints	43
3.3	Dynamic Programming	44
3.3.1	IDP General Formulation	45
3.4	IDP Formulation for FCHV EMS	48
3.4.1	Linearized IDP Formulation for FCHV EMS	49
3.4.2	Weighted IDP Formulation for FCHV EMS	50
3.5	Looped Dynamic Programming Algorithm	52
3.6	State Machine Control Algorithm for Comparison Methodology	57
3.7	Stress Analysis using Haar Wavelet	58
4	Improved Dynamic Programming Algorithm for Known Driving Cycles	60
4.1	Algorithm Validation	60
4.2	Sample Driving Cycle	61
4.3	Optimum Power Allocation using IDP	63
4.3.1	Highway Driving Cycle	64
4.3.2	FUDS Cycle	67
4.4	Weighted Improved Dynamic Programming	69
4.4.1	Battery Weight Analysis	69
4.4.2	Comparative Modes	71
4.5	IDP and RB Comparative Analysis	73
5	Improved Dynamic Programming Algorithm for Analogous, Unknown and Special Event Driving Cycle	77
5.1	Analogous Driving Cycles	77
5.1.1	Stochastic Approximation of a Driving Cycle	78
5.2	Two-minutes Cycle derivation	80
5.2.1	Analogous Cycle Derivation Procedure	80
5.3	Analogous Cycle Derivation Example	82
5.3.1	Speed Curves and corresponding Load Profiles	83
5.4	Driving Cycles with Special events	85
5.5	Special Events Formulation	88
5.6	Unknown Driving Cycles Looping Mechanism	90
6	Real Time Testing	97
6.1	Real Time System Model	98
6.2	Fuel Cell System Model	99
6.3	Battery System Model	101

6.4	Inverter BFC2000	102
6.5	Power Supply	104
6.6	Real Time System Characteristics	105
	6.6.1 Load Profile Modification	105
	6.6.2 Off-line Optimization Variables	106
6.7	Real Time System Testing, Analysis and Results	108
	6.7.1 Real time Comparative Results	108
	6.7.2 Real time/Off-line Comparative Results	112
6.8	Summary	117
7	Conclusions	118
	7.1 Contributions	118
	7.2 Future Work	120
A	Abbreviations and Notations	121
	A.1 Abbreviations	121
	A.2 Notations	121
	Bibliography	127

List of Figures

1.1	Dissertation outline.	9
2.1	FCHV Topological Model.	11
2.2	Fuel Cell System.	14
2.3	Fuel Cell Simulink Block Diagram.	16
2.4	Fuel Cell Net Current Curve.	17
2.5	Fuel Cell Polarization Curve.	17
2.6	Hydrogen Fuel Consumption Rate.	18
2.7	Battery Equivalent Circuit Model.	19
2.8	Battery SOC Range.	20
2.9	Battery Simulink Model.	21
2.10	Battery OCV-SOC Dependency.	22
2.11	Battery Resistance-SOC Dependency during Charging.	22
2.12	Battery Resistance-SOC Dependency during Discharging.	23
2.13	Battery Resistance dependency on Temperature.	23
2.14	PID Controller.	26
2.15	Wheel Swirl Resistance.	28
2.16	Electric Motor System Efficiency Map.	30
2.17	Transmission System Model.	30
2.18	EMS Simulink.	33
2.19	EMS Topological Model.	34
3.1	Power Train Losses.	37
3.2	Fuel Cell - Hydrogen consumption Map.	40
3.3	Battery Q Maps.	41
3.4	Improved Dynamic Programming Sketch.	47
3.5	Improved Dynamic Programming Sketch.	48
3.6	Improved Dynamic Programming Forward Algorithm.	50
3.7	Looped Dynamic Programming Sketch.	55
4.1	Sample Driving Cycle.	62
4.2	Chain of analysis.	64
4.3	Highway Power Profile.	64

4.4	Highway Cycle using IDP.	65
4.5	FUDS Cycle using IDP.	67
4.6	Highway Cycle - SOC Profiles for Weighted Battery Cost.	70
4.7	FUDS Cycle - SOC Profiles for Weighted Battery Cost.	71
4.8	IDP RB Comparative Results.	76
5.1	Steady State Speed Probability Distribution.	79
5.2	Two Minutes Highway Speed Profile.	80
5.3	Two Minutes Highway Power Profile.	81
5.4	Two Minutes Urban Speed Profile.	81
5.5	Two Minutes Urban Power Profile.	82
5.6	5 Minutes Road Profile.	84
5.7	19 Minutes Road Profile.	84
5.8	5 Minutes Power Allocation Profile.	85
5.9	5 Minutes SOC Profile.	86
5.10	5 Minutes Speed-Torque Profile.	86
5.11	Episode - 19 Minutes Power Allocation Profile.	87
5.12	19 Minutes SOC Profile.	87
5.13	19 Minutes Speed-Torque Profile.	88
5.14	Wheel Speed Before and After the Special Event.	89
5.15	The optimal power allocation for the Episode Occurrence.	90
5.16	The Battery SOC for the Episode Occurrence.	90
5.17	The Power Behavior with and without the Episode Occurrence.	91
5.18	The Power Behavior During the Episode Occurrence.	91
5.19	Looping Method.	92
5.20	Fuel Cell Power Profile Comparison.	94
5.21	SOC Profile Comparison.	95
5.22	HW Profile Comparison.	96
6.1	Labview Command Panel.	100
6.2	Labview Fuel Cell Panel.	100
6.3	Labview Schematic Panel.	101
6.4	Labview Sources Panel.	101
6.5	Ballard Nexa Fuel Cell.	102
6.6	Load Curves for Hc Cycle.	106
6.7	Load Curves for Uc Cycle.	107
6.8	Nexa FC Hydrogen Consumption Curve.	107
6.9	FC IDP/RB Comparative Curves during Online operation for Hc Cycle.	108
6.10	Window - FC IDP/RB Comparative Curves during Online operation for Hc Cycle.	110
6.11	Window - FC IDP/RB Comparative Curves during Online operation for Uc Cycle.	110

6.12	FC IDP/RB Comparative Curves during Online operation for Uc Cycle.	112
6.13	Battery IDP/RB Comparative Curves during Online operation for Hc Cycle.	113
6.14	Battery IDP/RB Comparative Curves during Online operation for Uc Cycle.	113
6.15	FC IDP online/offline Comparative Curves for Hc Cycle.	115
6.16	FC IDP online/offline Comparative Curves for Uc Cycle.	115
6.17	SOC IDP online/offline Comparative Curves for Hc Cycle.	116
6.18	SOC IDP online/offline Comparative Curves for Uc Cycle.	116

List of Tables

2.1	FCHV Subsystems.	11
2.2	Fuel Cell Characteristics.	16
2.3	Battery Characteristics.	24
2.4	Drivers Model Characteristics.	26
2.5	Vehicle Model Characteristics.	27
2.6	Motor System Characteristics.	29
2.7	Auxiliaries Power.	31
2.8	Power Conditioning Characteristic Data.	32
3.1	FC Experimental Data.	39
3.2	Battery LifeCycle Estimation.	41
4.1	Comparative Results for LP and LIDP.	61
4.2	Vehicle Parameters.	63
4.3	Highway Driving Cycle Results.	67
4.4	FUDS Driving Cycle Results.	69
4.5	WIDP Results.	72
4.6	IDP/RB Comparative Results.	74
5.1	Traffic Coefficients.	83
5.2	5 Minutes Road Data Characteristics.	83
5.3	19 Minutes Road Data Characteristics.	83
5.4	After 500 seconds Cost and Hydrogen Consumption Comparison.	89
6.1	FCHV Test Bench Subsystems.	99
6.2	Nexa Fuel Cell Characteristics.	103
6.3	Serial Battery Characteristics.	103
6.4	Electronic Load Characteristics.	104
6.5	Power Supply Characteristics.	104
6.6	Data Characteristics.	105

Chapter 1

Introduction

Going Green is becoming one of the main mottos of this era. There is an increasing awareness regarding the dangers of polluting emissions and the depletion of energy resources. Global greenhouse gas emissions are contaminating our environment by causing temperature changes and depleting the ozone layer. This has led to an excessive investment in research for alternative and clean energy resources. One of the main sectors contributing to the emissions of such pollutants is the transportation sector. Therefore, trends are adopted in-order to develop new policies and trigger technological improvements in an attempt to surmount these effects. According to a report published for the new center on global climate changes, emissions can be lowered up to 65% from their level in 2010, by the year 2050 [1]. Moreover, the automotive industry ACEA should lower the amount of CO_2 emissions from 190g/km in 1995 to 120g/km in 2010 [2].

These improvements can be achieved by switching to emission free fuels and enhancing electric vehicles operations and efficiencies. Research in the automotive industry is heading towards replacing the internal combustion engine (ICE) of the vehicle with energy sources that have nearly zero polluting emissions such as fuel cells (FC) and energy storage systems. Fuel cell hybrid vehicle (FCHV) is one promising candidate. FCHV with battery storage systems have low emissions, high energy efficiency and independence on fossil fuel based resources. However, they have a high cost of production which is around 88% higher than ICE based vehicles [3]. According to a test performed on a three wheeled vehicle, FC based vehicles have better performance and fuel economy than ICE based vehicle. However, it will cost around \$10,000 to convert a vehicle into a FC based one [4].

The propulsion system of FCHV is equipped with fuel cells supplemented with a hydrogen tank and energy storage components. The addition of such power peaking sources results in further degree of freedom in the allocation of power resources as well as solving the transient power effects on FC. FC and battery systems aid each other to provide cruising power. The battery system is responsible to provide additional accelerating power as well as absorbing re-

generative braking power. Therefore, the FC size will decrease because FC can only be sized to take cruising power demands while high loads can be supplied by storage devices. This will lower the cost of the FCHV and will improve the life of the FC [5]. FCHV have proven their advantageous performance in various demonstration programs under all operating conditions including cold-starts, but there is still a room for further improvement in order to reach the target costs in production and operation as well as lifetime requirements.

Research is heading towards improving different components of the FCHV system such as the design of the FC [6] [7], chemistry of the battery [8] [9] [10], hybridization topology [11], the technology and efficiency of the converters [12] [13] [14]. Moreover, they are indulged in the design and optimization of the energy management system (EMS) [15] [16]. Of importance is to find the best fit in scaling and managing the different power sources and storage units. The next section presents a detailed literature review of the different EMS studied for FCHV.

1.1 Optimum Power Allocation in FCHV

FCHV employ energy management systems to identify the power allocation among the different sources. The EMS addresses the power distribution among the different vehicle power sources in an attempt to meet the load demand while adhering to operational and component constraints. EMS algorithms range from simple rule based methods and heuristic approaches to complex optimization algorithms. The key element is the degree of knowledge of the driving cycle and the computational complexity of the algorithm [17].

There is a wealth of paper that addresses the design of the energy management systems in FCHV. A comprehensive review of the state of art of FCHV architectures along with the most tackled approaches in EMS is presented in [3] [18] [19]. A comparative analysis between the different methods for the optimal power allocation is presented by Motapon el al [20]. EMS is tested for different driving scenarios such as highway driving cycle, urban driving cycle, fast acceleration and maximum driving distance [21]. In addition, EMS is designed to satisfy the five different modes of operation in FCHV which are starting, cruising, passing, braking and stopping.

Two kinds of EMS controllers are addressed, off-line controllers and on-line controllers [22]. On-line controllers are real time controllers, which use PI controllers, frequency decoupling strategies or rule based controllers.

Off-line controllers use intelligent or non-intelligent approaches in order to find the optimal power split between energy sources in an attempt to minimize hydrogen fuel consumption or system cost. Optimization approaches can use linear programming techniques [23], dynamic programming [24], stochastic dynamic programming [21], game theory [25], genetic algorithm [26], load shifting [27], equivalent consumption minimization strategy, control theory [28] [29],

neural networks [30] [31] [32], predictive controllers [33] [34], adaptive optimal control [35], thermostat and power follower controls [36] [37] and H-infinity control [38].

In load shifting [27], a rule based method is defined in order to assure drivability. The demanded load is shifted between the FC and battery according to the SOC of the battery. Seven different SOC set points are defined and load shifts between power generation, regenerative braking, and continuous boosting to dynamic boosting. Hegazy et al [39] used genetic algorithm as well as particle swarm optimization mechanism to minimize the cost, mass and volume of a FCHV. Higher vehicle performance was achieved along with better sizes. Classic PI controllers monitor the performance of the main variables of the FCHV on-line. The variables can be the battery state of charge or the voltage at the DC bus. These controllers do not depend on previous knowledge of an expert nor on the driving cycle [40] [41] [42]. This method allows the FC to supply a steady load for the power demand and the energy storage component to deliver the extra power required. Frequency decoupling strategy splits the demand into low and high frequency. The FC provides the low frequency part of the demand and the other components provide the high frequency component. This is done using low pass filters, wavelets [43] or fast Fourier transforms [11]. The advantage of such a strategy is to prolong the lifetime of the FC system by preventing dynamic stresses. Therefore, the FC always supplies the base load and other sources supply the extra load or absorb the energy when demand is below base load value. The detailed modeling of the FCHV powertrain reveals high levels of non-linearity. In [44], the authors optimized a FC system by minimizing hydrogen consumption. The method is formulated as an NLP aiming at minimizing the stack current subject to non-linear constraints depending on the net power of the fuel cell and the oxygen excess ratio. Then they generate look-up tables that hold the optimum variables for each specified demand. The method is solved by an NLP simulator called gams.

1.1.1 Rule Based Energy Management Systems

Rule based EMS excels in real time applications because it does not require prior knowledge of the driving cycle. It is easy and simple however it is based on heuristics, designer expertise and engineering intuition. Rule based methods can be either fuzzy or deterministic approaches such as state machine control.

State machine control is based on person's expertise as well as heuristic approaches [45] and [46] [47]. The performance of such a method is highly dependent on the approach and the efficiency of the rules. For example, one can formulate a set of states and choose the power required from the FC according to battery SOC level and demanded load. The main drawback is the hysteresis component that results from the switching between the states. This component is usually hard to control. Deterministic rule based EMS are usually based on

look-up tables where demand actions are known. Fernandz et al [48], adopted the method of state machines to a tramway composed of four electric motors and FC and battery systems. The control mechanism determines the degree of hybridization depending on the load demand, the tramway speed and battery SOC.

Fuzzy logic power allocation is based on membership functions and if-then statements. The method can be tuned to achieve better results than the state machine control method, however it still relies on conditional statements which are derived from person expertise in the subject [49] [50] [51], [32]. Li et al. [32] optimized the width and centers of membership functions in order to find the optimal degree of hybridization between FC and battery system. The response is usually faster than that of state machine control, and with higher precision. Ravey et al [22], adopted a fuzzy logic for the control of a FCHV. The control strategy uses SOC based membership functions that demand the state of the power from FC. For known driving cycles, genetic algorithm is used to find the optimal parameters of the membership function to result in minimum hydrogen consumption. Trapezoidal membership function of the battery SOC can be employed along with a series of if-then statements in-order to determine the fuel cell power supply. The fuzzy rule based EMS address the nonlinearity of the automotive power management problem and is adaptive to different operational modes. EMS have been tested under conventional [30], adaptive [16] and predictive [52] fuzzy control strategies.

1.1.2 Adaptive Control

Dalvi et al [15] presented an adaptive gradient based control. They revealed the challenges that face engineers when designing a controller for FC systems. Namely, the interaction between the compressor and FC stack. These two components have different response to dynamics and thus may lead to errors in output values. The electrolyte and catalyst surface of the FC can be damaged completely if they are subjected to low oxygen concentrations. During transients, the demanded current is higher so the controller should increase the flow of oxygen to the FC in order to maintain oxygen partial pressure. The compressor takes more time to supply the oxygen to the cathode when more current is demanded from the FC. So an oxygen stoichiometry dip is revealed along with a decrease in the voltage. This is due to the fact that higher oxygen pressure leads to lower voltage losses. To avoid oxygen starvation, the oxygen excess ratio is stabilized around 2.

1.1.3 Optimization based Energy management systems

Optimization strategies [53] [54] are complex methods with high computational processing which causes problems in the response time of the energy management

system. They minimize an objective function addressing cost, emissions, power levels or others. The optimal solution converges while satisfying the demand and enhancing vehicle efficiency. Some methods can be adopted in real time simulations [55] [56].

Global Optimization

Yu [57] proposed a FC, battery and super-capacitor hybrid electric vehicle based on active power flow control strategy which aimed to meet vehicle demand, minimize total cost, optimize battery life and reduce volume and mass of components. The proposed method tuned global optimization parameters to be applied to real time systems. They used a weighted cost function that force SOC to be closed to a predefined limit and force the FC to operate around rated power so as to improve its efficiency. Weights are re-adjusted depending on the cycle. With urban cycles where the power demand is usually low, higher weight is associated with FC power so as to minimize hydrogen fuel consumption. On the contrary during highway cycles, lower weights accompany the FC power so as to protect the battery from over discharging.

Equivalent Consumption Minimization Strategy

Equivalent fuel consumption minimization strategy (ECMS) minimizes the cost function which includes the hydrogen fuel consumption of the FC and an equivalent energy consumption method of the storage component [53] [54] [58] [20]. It is an optimization method used to approximate the optimal allocation of power and could be adaptable to real time situations. It is an optimization method used to find an approximate value for the optimal split. It is based on formulating the problem by setting the battery power as equivalent hydrogen fuel consumption. This method approximates the power needed from the sources. In [44], the authors optimized a FC system by minimizing hydrogen consumption. The method is formulated as an NLP aiming at minimizing the stack current subject to non-linear constraints depending on the net power of the fuel cell and the oxygen excess ratio.

Rodatz et al [53], formulated the problem by minimizing the total sum of power supplied by the FC and super-capacitor system. The battery power is penalized by a certain factor based on ECMS principle. They used a lookup table indexed with the electrical energy used by the super-capacitor and electric energy consumed by hydrogen. To make the method adaptable to real time situations, they used a probabilistic approach to find the feasible value for the penalty factor based on the lookup tables and the charging/discharging mechanisms of the super-capacitor system. The probability function is a fraction of the sum of the storage energy and demanded energy from the available FC energy. It avoids deviations of SOC from minimum and maximum limits. The method proved to

work well in real time situations because the penalty factor can be easily tuned as well as the method is self-adaptive. Geng et al [29] also minimized the cost function of plug in FCHV using ECMS. The battery in the cost function is modeled as a weighted factor multiplied by the battery power and divided by the lower heat value of hydrogen. Sciarretta et al [56] employed an equivalent probabilistic factor for the battery energy in the minimization function. The algorithm is based on ECMS and is independent on the driving cycle. At each step in time, the vehicle speed and acceleration are measured and the torque at the wheels is calculated. Then the energy from the FC and battery are computed for different values of the split and the one leading to a minimum cost is selected. It is noted that the weighted coefficient of the battery energy takes into consideration the SOC limitations.

Linear Programming

Tate et al used linear programming [23] techniques to optimize the split of power between an internal combustion engine (ICE) and a battery system. The method is formulated as a convex problem and then approximated as a large linear program. To account for the change in battery efficiencies during charging and discharging, they implemented them as two separate variables. On the other hand, the whole power train is modeled on efficiency basis. The authors in [59], adopted the same methodology to a FCHV and implemented a controller based on linear programming technique. The main issue with linear programming is that it can give us a gist of the control while mainly to model the components in the FCHV power train high levels of non-linearity is involved.

Dynamic Programming

Dynamic programming (DP) is a popular technique of choice for the optimal power allocation of FCHV. It is widely used and adopted to control the degree of hybridization between the vehicle sources whether ICE based [24] or purely electrical. It is used for solving recursive problems and it ensures optimality within certain tolerance and depicts ease of implementation [60]. The main problem with DP is the curse of dimensionality where the number of states increases exponentially with time [61]. Moreover, DP relies on the previous knowledge of the driving cycle. It has been used to optimize the power split between the different energy resources in hybrid electric vehicles (HEV) [62]. It was tackled by many researchers and applied to different types of HEV. In [62], the HEV power sources are the internal combustion engine (ICE) and the battery system. DP is used to test the effect of battery weight and storage capacity on the operational cost. The analysis leads to the selection of the most feasible battery capacity to lower system costs. Vinot et al [63] used DP for an electric vehicle with ICE. The outcome of the program locates the optimal split factor between the engine and

the motor. As well as locating the optimum operating point of the engine. Xu et al [64] developed a controller based on dynamic programming where the cost of FC and battery are minimized while subjected to limit constraints. The authors introduced a penalty factor on the SOC where the cost increases cubically if SOC is outside the limit margin. Dokuyucu et al [65] formulated a controller based on dynamic programming to find the torque split between the internal combustion engine and the electric motor. The control signal considered is the battery SOC which is bounded between 0.4 and 0.7. Results show that during low torque demands, the vehicle operates in motor mode and charging is favored. While during high torque demands, both the battery and the ICE assist in feeding the load. They analyzed two different series parallel architectures for the HEV. They used an electric variable transmission concept which leads to slightly higher fuel consumption range, but it can be tweaked by using a gear between the engine and motor. To address the dimensionality constraint limitation of DP, improved dynamic programming technique (IDP) is used. This novel method considers a tunnel of fixed states rather than an exponential increase in the number of states. In [66], power levels of fuel cell are considered in the state vector while in [67] the authors take SOC levels as state vectors. Both latter papers consider the improved DP and the results are not far from using the regular DP. To overcome the problem of previous knowledge of the driving cycle, stochastic dynamic programming (SDP) is adopted where the control laws can directly be implemented. Using SDP, the system is modeled as a Markov chain and an optimal policy based on fuel minimization is defined. The optimal path is located by minimizing the cost, which corresponds to the optimal policy [68]. Lin et al presented in [69] a control for a hybrid electric truck based on SDP. The power demanded is modeled as a Markov process. Two state variables are studied which are the battery SOC and the wheel speed. The power demand and the wheel speed are assumed to take discrete values. The authors' goal is to minimize the fuel consumption along with the emissions. To achieve that, they developed an optimal EMS to manage the power flow between the vehicle engine and the electric motor [70]. Kim et al in [21], combined the optimization of the hybrid FC system components along with optimizing the control of power. The goal is to minimize the cost of the system using SDP. To obtain that, the authors started by modeling the future load as a probability function based on tested driving cycles. SDP constructs optimal strategies for each Markov state and those are employed as lookup tables.

1.2 Thesis Contribution

Modern engineering is investing extensive research on the development of hybrid vehicles which are effective alternatives to fossil fuel based vehicles. One of the challenges facing fuel cell hybrid vehicles is to implement a control strategy to find the optimal split of power between the different power sources. The dissertation

tackles contemporary issues in the energy management system of the FCHV. The configuration addresses two stage control methodologies, pre-driving optimization algorithms and on-line optimization using PID controller.

In the first stage, an improved version of dynamic programming is adopted to find the sub-optimal power split between the fuel cell and the battery during a certain driving cycle. This technique proves convergence faster than the normal dynamic programming algorithms which suffer from dimensionality problems. Battery weighting factor is added to the existing cost function to have different versions for the battery utilization profiles.

The improved dynamic programming is one of the powerful optimization algorithms, however it needs apriori knowledge of the driving cycle. A looping version of the technique is used to cater for totally unknown driving cycles and special event occurrences. Stochastic approximation of the driving cycle is adopted if apriori knowledge of the cycle is not accurately known.

On-line optimization is performed using a complete Simulink designed model of the fuel cell hybrid vehicle; improved dynamic programming is used to test the efficiency of such algorithm in lowering operational cost while ensuring drivability. A PID controller minimizes the error between the actual and approximated vehicle speeds. A looped improved dynamic programming technique is tested during on-line operation, to tweak deviations from pre-set cycles by updating the weighted IDP algorithm as the vehicle accelerates.

A final objective of this dissertation is to investigate real time testing which is held on a stationary miniature model of the FCHV in UAS labs in Germany. The driving cycles chosen mimic those tested in the off-line and on-line operations discussed in the previous paragraph. The only difference is in the sample time which is downsized to match the capacity of the stationary system sources.

The performance criteria are based on the overall operational cost as well as the hydrogen consumption per trip. Moreover, battery state of charge and system efficiencies are also measured and analyzed. To measure the life-cycle of the FCHV subsystems, an approximation based on a wavelet transform of instantaneous power of the system components is considered. The proposed dissertation is expected to yield several outcomes. The achievement of the said outcomes is expected to result in lower system cost, improved efficiency of the drive train and prolonged life of FC and battery. Comparison with an existing EMS will highlight the distinct features of the intelligent EMS. Comparison is done between a controller using the optimization algorithms for the whole driving cycle and a controller using state machine rule based techniques. Results indicate a reduction in system cost and in hydrogen fuel consumption. Moreover, the results highlight the importance of using optimizing algorithms in urban driving cycles since reduction in hydrogen consumption is much higher compared to highway cycles.

The approach is based on solving several problems. It is divided into theoretical and experimental modules. The theoretical part is developed at the

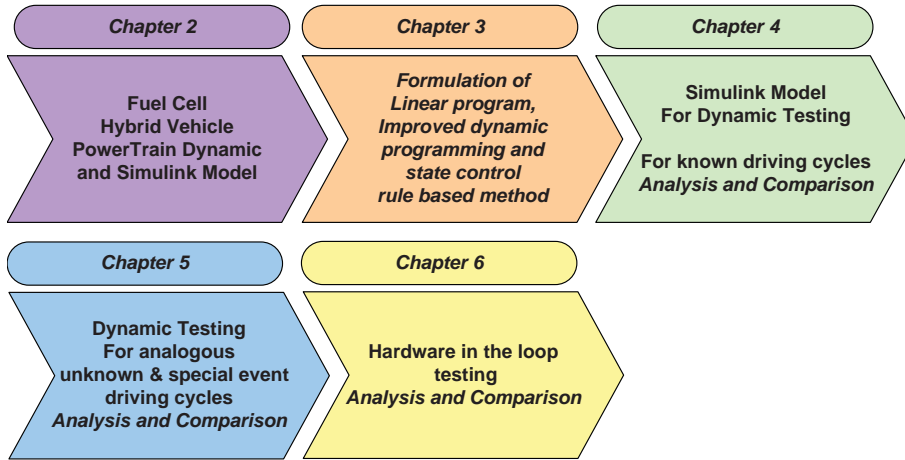


Figure 1.1: Dissertation outline.

American University of Beirut (AUB) under the supervision of professors from AUB and the University of Applied Sciences at Esslingen in Germany. The experimental part is carried out in collaboration with the University of Applied Science (UAS) in Germany. UAS provided both FCHV lab facilities and technical expertise. They built a stationary miniature model of the FCHV where the tests for the EMS are carried out. Based on literature review, there has been no work, to my knowledge, on such a design of an intelligent EMS which helps the driver optimize fuel usages and better utilize the vehicle.

1.3 Organization of the Dissertation

An overview of the dissertation outline is shown in Fig. 1.1.

1.4 Abbreviations

The list of abbreviations used in this dissertation is presented in Appendix A.

Chapter 2

Modeling the FCHV PowerTrain

The construction of the FCHV subsystem models in graphical simulation environment software is widely exploited in literature. It is essential for the models to emulate the real dynamics of the vehicle in-order to have efficient simulation results [17] [16] [15] [71]. Figure 2.1, reveals the topology of the system under discussion. In this dissertation, the FCHV is composed of at least seven different subsystems as indicated in table 2.1. The sources in the subsystem are a primary one-way energy source unit and a secondary bi-directional storage component. The former source is a PEM fuel cell system and the latter is a Li-ion battery.

The vehicle considered in this paper is a light duty sprinter. It has two energy sources which are the FC and the battery in a parallel configuration. The drive train is of the series type with a 70 kW induction electric motor. The battery system has a nominal energy of 1.9 kWh. The 70kW FC System is based on hydrogen fuel with an operating voltage range between 250 and 430V. Therefore, the battery system can assist with power during fast dynamics to prolong the life cycle of the FC and to reduce fuel consumption.

In figure 2.1 the solid black arrows indicate the flow of energy between the subsystems. The dashed blue arrows are for sensing information and the dark blue arrows represent the controller's actions. The black dashed arrows represent the flow of data.

The FC is connected to the DC bus via a DC/DC converter that serves to stabilize the voltage at the bus. The fuel cell is supplied by a hydrogen tank. The level of hydrogen in the tank ($M_{O_{H_2}}$) is monitored by the efficient energy management system.

The battery system is joined to the DC bus in parallel using a bi-directional DC/DC converter. This enables the battery to discharge current into the system to serve the load, and charge current during regenerative braking. The converter is controlled by the system controller. The state of charge of the battery is sensed by the efficient energy management system.

The electric motor is connected to the DC bus via a DC/AC inverter. It is serially coupled to the transmission system and wheels. The information of the inverter and electric motor is sensed by the controller system.

The DC bus supplies the vehicle auxiliaries with DC power which will be

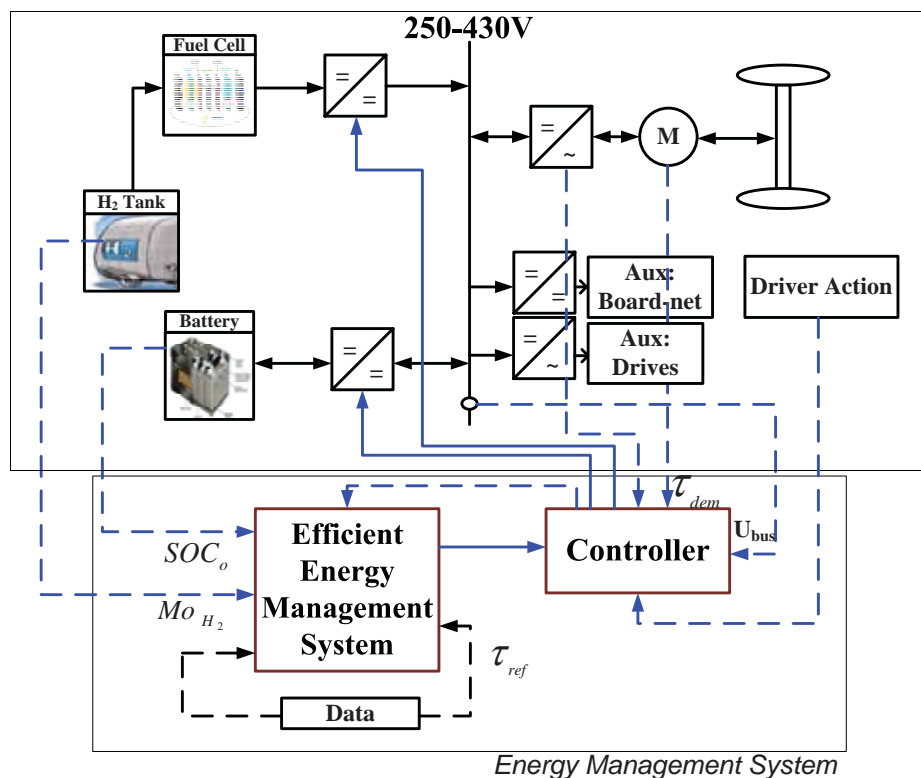


Figure 2.1: FCHV Topological Model.

Table 2.1: FCHV Subsystems.

Subsystem	Description
FC System	PEM FC with a rated power of 70 kW
Battery System	Lithium ion battery with a capacity of 6.5 Ah
DC/DC Two Way Converter	For the battery discharging and charging currents with a high voltage of 250-400V
Electric Motor	An induction AC motor along with its inverter rated at 180 Nm, 70 kW
Vehicle Dynamics	Dynamic models of all the forces acting on the vehicle
Drivers Model	Calculates the torque demand from the speed profile of the driving cycle
EMS	Optimal power allocation of the demand

transformed to AC by inverters. The auxiliary path is split in two branches. The first branch connects the 24V DC board to the bus using a DC/DC converter. The other branch embeds a DC/AC inverter to join the DC bus to the electric drives of the subcomponents such as the air conditioning, servo brakes and water pumps. This is a fuel cell dominant model similar to Daimler A, B class vehicles.

The energy management system block consists of two components, the efficient energy management system (EEMS) and the controller. The data block sends system costs and characteristics to the EEMS. Moreover, it sends the estimated torque demand (τ_{ref}) based on the selected driving cycle. The EEMS block senses the initial state of charge of the battery and the initial level of hydrogen in the tank. It feeds the power split between the fuel cell and battery to the controller. The controller feeds back the actual vehicle information to the EEMS.

The controller receives the control actions from the EEMS and sends it to the battery's bi-directional converter and the converter of the fuel cell. It senses information from the driver action, electric motor, inverter and DC bus voltage.

The mathematical models that govern these subsystems encompass high levels of computational complexity. For this reason, simple dynamic equations as well as test-benched experimental results indexed as lookup tables are used to model the subsystems in Simulink. The model of the subsystems is based on a distributed control system with a CAN bus communication method. The CAN network is designed to regulate the performance of the FCHV. An energy management system strategy based on optimization algorithms is formulated to coordinate the power split between the sources. The model is built at the University of Applied Sciences in Esslingen with the help of several engineering students from the mechanical and electrical field disciplines. It is comprehended and tuned to fit the runs needed to complete the dissertation objectives.

In this chapter, the subsystems of the FCHV are modeled based on mathematical models of the FCHV dynamics. Then based on approximations of the models and experimental data, a model of the subsystems is built using Simulink. This model emulates the real time behavior of the vehicle. The chapter has the following structure. The fuel cell model is detailed in 2.1 and the battery model is presented in 2.2. The vehicle model is presented in Section 2.3. The model for the electric motor and transmission subsystems is shown in Section 2.4 and 2.5. The power conditioning subsystem is explained in section 2.7. Finally, the energy management system is modeled and executed in section 2.8. ¹.

This chapter has several contributions and relevance to the whole dissertation and these are summarized in the bullets below:

1. Fully understand the modeling phenomenon of the FCHV especially with

¹This chapter is done in collaboration with Mr. Ying Huang at the University of Applied Sciences where he developed the Simulink Model of the FCHV during his master thesis

the lack of documentation for the existing Simulink model.

2. Simplifying and implementing the models in MatLab/Simulink in-order to perform testing of the different algorithms that will be discussed in the subsequent sections.
3. Formulating the dynamic equations and gathering the test-benched experimental data of the different components of the FCHV powertrain.
4. Editing the Simulink model in order to install the energy management system that is formulated in this chapter of the dissertation in attempt to launch system testing and perform diagnostic analysis of the results.

2.1 Fuel Cell System Modeling

Fuel cell systems are composed of cells that convert the chemical energy present in hydrogen fuel into electrical energy by oxidation-reduction reaction. They produce a continuous amount of electricity as long as they are provided with fuel and oxygen to maintain the reaction process. Figure 2.2, shows the cathode at the positive side, the anode on the negative side and the electrolyte that facilitates the path of electrons to complete the circuit. Electrons travel from the anode and into the cathode producing a DC current. At the anode, hydrogen oxidizes into protons and electrons. The protons travel through the electrolyte while the electrons are forced to move through the external circuit because the electrolyte acts as an insulator. The charges reunite at the cathode and react with oxygen to produce water.

There are different types of FC depending on the type of membrane used as an electrolyte. These can be polymer exchange, phosphoric acid, solid oxide, molten carbonate or other type of fuel cells. The difference is in start-up time, power density and operating temperature. For example, PEM FC has a starting time of one second while solid oxide fuel cells need at least ten minutes to start up. Fuel cells are manufactured as small cell units each having an open circuit voltage of around 0.7 V. They are stacked in series to reach the required voltage level. This voltage is affected by activation losses, ohmic losses or mass transport losses.

Proton exchange membrane fuel cells are usually embedded in vehicular applications due to their fast start-up time, high power density and low operating temperature [15]. Their transient performance when responding to load demand is limited due to the chemical reactions that occur in the FC. Sometimes, it takes 1 to 2 seconds for the FC to respond to the load demand [57]. High dynamic operations may cause significant negative impacts to the overall lifetime of the cells. Moreover, during high or fast power demand there is a high voltage drop in the FC. This means that more oxygen supply is needed from the compressor

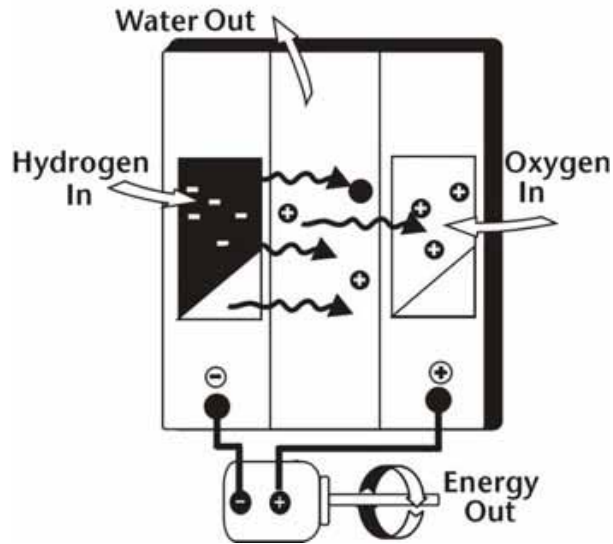


Figure 2.2: Fuel Cell System.

which is usually powered by the FC. The latter case might give rise to the concept of oxygen starvation which draws high currents from the FC. Oxygen starvation causes drainage of the FC and might severely damage the membranes [15]. The other challenge facing PEM FC is in controlling the water and air supply. This means that the membrane needs to remain hydrated at the same rate of water evaporation. For this reason, a constant ratio between oxygen and reactants should be maintained in order for the FC to continue its efficient operation. Otherwise, the membrane will either dry out or be flooded with water if evaporation in the membrane is too fast or too slow respectively. On the other hand, the reaction that produces water is exothermic which leads to additional thermal energy accumulations in the FC. This needs a temperature control mechanism to keep the cell from thermal loading. FC auxiliary components, such as the compressor, need additional power supply which can be approximated to 4kW. This is around 95% of power demanded by FC auxiliaries [15]. The service life of PEM FC for automotive applications is 5000 hours under normal conditions. The efficiencies of the FC ranges between 25 to 60% and they require more maintenance than batteries or super capacitors [57]. However in the transportation sector, the efficiency of PEM FC is around 60% [72].

FCHV high cost can be cut via volume production of units for automotive applications. The department of energy approximated that with a volume production of 100,000 units per year the cost of PEM FC is 67 \$/kW. The cost can decrease to 55 \$/kW with a volume production of 500,000 units per year [73]. Improvements of FC system along with the supervisory control between the FC and its converters to control the flow of reactants as well as maintain the voltage

on the DC bus. The coordination between the compressor and the converter is needed [74]. The FC system depends on the FC current, the partial pressure of oxygen, hydrogen and the cathode, stack temperature and humidity.

2.1.1 Fuel Cell Dynamic Model

In this section, a static model of a PEM FC is selected consisting of 350 cells in series. To avoid complex chemical equations of the FC, the net power output of the fuel cell is shown in equation 2.1, where the power demanded by the compressor, the FC auxiliaries and system losses is deducted from the power supplied by the stack. The auxiliary components in the FC are the radiator fan, coolant pump and others. The auxiliary power is neglected because 95% of the power demanded by the auxiliaries is consumed by the compressor. To avoid non-linearity, the compressor power demand can be approximated to 1kW. The FC power losses are mainly the ohmic and activation losses.

The rate of consumption of hydrogen in the FC stack depends on the current of the stack according to equation 2.2. The rate of air flow into the cathode is formulated in equation 2.3. The minimum and maximum limits of the power from the FC are defined based on the efficiency maps of the FC system. While the dynamic response of the FC is limited between ramp-up and ramp-down rates.

$$P_{FC} = n_{st} V_{st} I_{st} - P_{comp} - P_{FC-aux} - P_{FC-losses} \quad (2.1)$$

$$\dot{m}_{H_2} = \frac{M_{H_2} n_{st} I_{st} \lambda_{H_2}}{nF} \quad (2.2)$$

$$\dot{m}_{air} = \frac{M_{O_2} n_{st} I_{st} \lambda_{O_2}}{4w_{O_2} F} \quad (2.3)$$

2.1.2 Fuel Cell Simulink Model

The aforementioned static model is used to derive the parametric values to construct the FC system. To build a fast and correct Simulink model of the FC, lookup tables are used to approximate the equations discussed in section 2.1.1. These tables were derived from experimental testing on an actual FC test-bench in the labs of the University of Applied Sciences of Esslingen Germany.

Figure 2.3, shows a schematic of FC system incorporated in the Simulink model. The current requested from the FC (I_{FC-req}) is limited to the maximum current (I_{FCmax}) that could be supplied by the FC according to the manufacturer's data sheet. Then the power required from the FC is calculated by multiplying the requested current with the corresponding voltage of the DC bus (V_{bus}). The FC power request (P_{FC-req}) is also limited between the maximum (P_{FCmax})

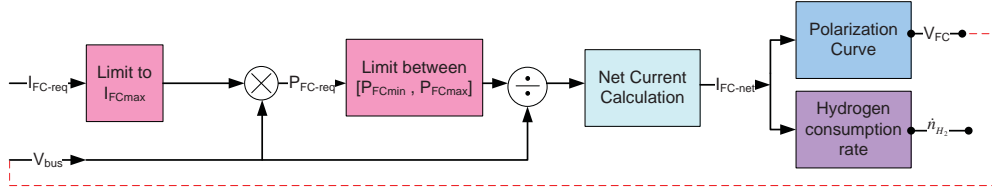


Figure 2.3: Fuel Cell Simulink Block Diagram.

Table 2.2: Fuel Cell Characteristics.

FC Current ramp up/down rates [A/s]	[290 , 290]
FC Power ramp up/down rates [kW/s]	[10 , -10]
FC max/min power [kW]	70/0
Resistance factor for series and parallel connection	40
FC stack number of cells	350
FC OCV [V]	345.8
FC minimum voltage [V]	250
FC maximum voltage [V]	430
Area for heat exchange on stack surface [m^2]	1.5

and minimum (P_{FCmin}) power of the FC that is provided in the data sheet. From the resulting FC current request, the net current request is computed using the net current curve in figure 2.4 which considers the fuel cell efficiency. Then, the net current is used to calculate the FC voltage using the polarization curve in figure 2.5. The latter takes into consideration the losses in the FC system such as activation and ohmic losses. The stack voltage is a function of the stack current and the cathode pressure. This voltage is the same voltage at the DC bus because the FC system is directly connected to the DC bus. Finally, using the net FC current request, the hydrogen consumption is approximated using the hydrogen consumption curve in figure 2.6. This curve is a function of the current requested from the FC.

In this dissertation, the characteristics of the chosen FC is shown in table 2.2. For a PEM fuel cell, the theoretical open circuit voltage is 1.23 V at 298 K, in practice it is around 1 V at open circuit. Under load conditions, the cell voltage is between 0.5 and 0.8 V. So taking the theoretical OCV as the maximum voltage, $1.23 \times 350 = 430V$; and a cell voltage of 0.714/cell (between 0.5V/cell and 0.8V/cell) is taken as the minimum voltage ($0.714 \times 350 = 250V$). For open circuit voltage, we just take the practical value of 0.988V/cell.

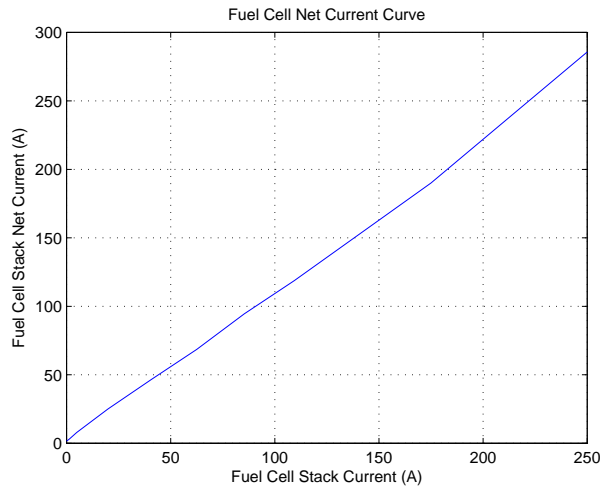


Figure 2.4: Fuel Cell Net Current Curve.

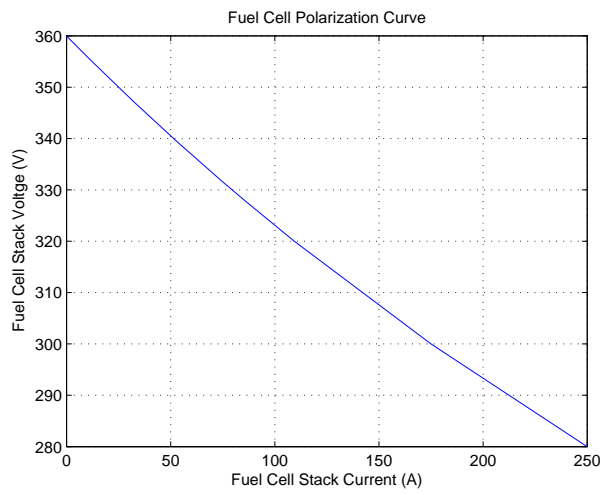


Figure 2.5: Fuel Cell Polarization Curve.

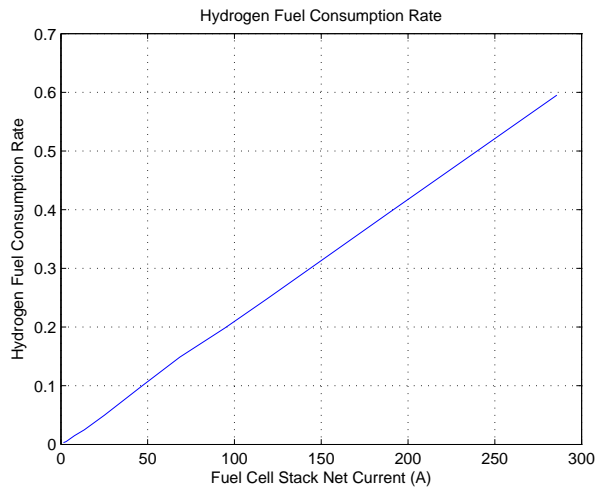


Figure 2.6: Hydrogen Fuel Consumption Rate.

2.2 Battery System

The next building block of the FCHV power-train is the energy storage component system. Energy storage components aid the FC to overcome transient response effects. They have faster dynamics and thus can quickly respond to power fluctuations. Normally, two devices are considered, super capacitors and batteries. Batteries have higher energy densities than super capacitors while exhibiting a lower power density. Batteries are mainly needed to capture the large amount of kinetic or potential energy that could be recovered by regenerative braking when reducing speed or running downhill. They can also power FC auxiliaries and provide additional power for accelerations. The types of batteries that are used in FCHV are lead acid, NiMh, or lithium ions. Improvements in battery systems in terms of performance as well as building high efficiency charging converters contribute to the growing interest in FCHV [48]. Variation in SOC of the battery affects the voltage, for instance a drop in SOC causes a decrease in the voltage. These variations affect the life of the BT and sometimes it can be deeply drained. The SOC of the battery system in automotive applications is limited between 20 to 80%.

The battery that is adopted for this work is a Li-ion because it is more attractive to the automotive applications. This is due to the fact that it has higher efficiency and better energy density when compared to lead-acid or NiMh/NiCad batteries [58] [75], as well as a minimum charge loss when it is not working. The charge and discharge efficiency is usually high ranging from 80 to 90% depending on the application [76]. The selection of the sizes is based on the Mercedes-Benz Sprinter used for the EU project HySYS (FP6) [77]. However, a 70kW FC is

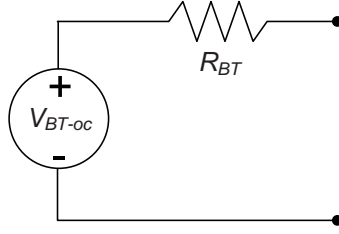


Figure 2.7: Battery Equivalent Circuit Model.

used for research instead of the 80kW FC used in the EU project.

The lithium ion battery stack is modeled as a simple resistive model [78] shown in figure 2.7. The output battery current depends on the open circuit voltage as well as the battery internal resistance and output power as shown in equation 2.4. The internal resistance of the battery is a function of the SOC (charging or discharging) and on the battery temperature. When the battery temperature increase, a factor is multiplied by the battery internal resistance to show its effects. The SOC of the battery is calculated in equation 2.5 according to the charging or discharging current. Li-batteries have the lowest discharge rate of 1.5-2 % per month [79] as compared to NiMh with 30% discharge rate. This can be approximated to a discharge rate of 80μ per second.

To derive the optimum range of the battery SOC, a test benched process is held at the UAS labs in Germany. After several tests, it is noticed that the favorable SOC range is between 0.55 and 0.65 as shown in figure 2.8. However, if the requirement is to drain the battery through the cycle and then charged again at night, then 20% is the lowest limits and lower hydrogen consumption is achieved.

The model used for the battery is the internal resistance model where the open circuit voltage and the internal resistance are functions of the SOC. The mathematical relation governing this dependency is shown in equation 2.4 and equation 2.5.

$$I_{BT} = \frac{V_{BT-oc} - (\sqrt{V_{BT-oc}^2 - 4R_{BT}P_{BT}})}{2R_{BT}} \quad (2.4)$$

$$SOC(t_k) = SOC(0) - \frac{1}{C_{BT}} \int_{t_0}^{t_k} I_{BT} dt \quad (2.5)$$

2.2.1 Battery Control System

In Simulink, the battery controller is used to monitor and calculate the maximum charging and discharging currents that are permissible. The battery control system calculates the maximum charge and discharge limits of the battery system

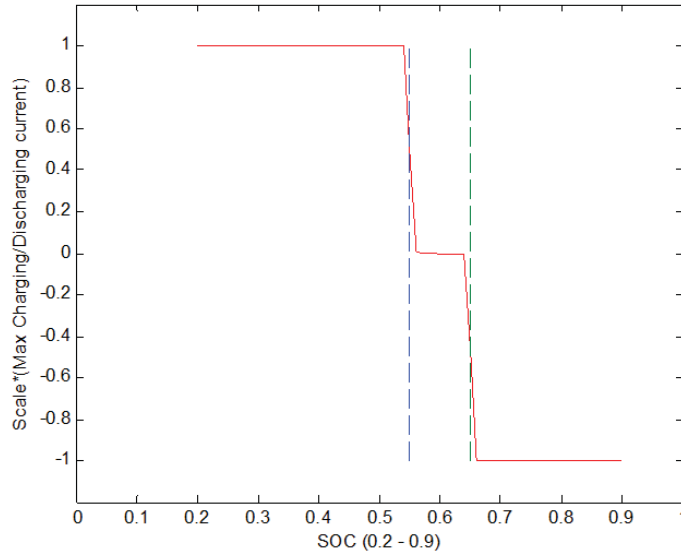


Figure 2.8: Battery SOC Range.

depending on the SOC level, open circuit voltage (V_{BT-oc}), internal resistance (R_{BT}) and temperature (T_{BT}). The maximum permissible positively charging current is shown in equation 2.6 and the maximum allowable negatively discharging current is shown in equation 2.7.

$$I_{BT-ch-max} = \begin{cases} \frac{V_{BT-max} - V_{BT-oc}}{R_{BT}} & SOC < SOC_{max} \\ 0 & SOC \geq SOC_{max} \end{cases} \quad (2.6)$$

$$I_{BT-disch-max} = \begin{cases} \frac{V_{BT-min} - V_{BT-oc}}{R_{BT}} & SOC > SOC_{min} \\ 0 & SOC \leq SOC_{min} \end{cases} \quad (2.7)$$

2.2.2 Battery Simulink Model

The Simulink model for the battery is shown in figure 2.9. It receives the battery current request and accordingly computes the battery voltage depending on the SOC, internal resistance and temperature. It is composed of four different blocks that are interconnected. These blocks are the SOC generator block, the open circuit voltage generator block, the battery resistance generator block and the thermodynamics block.

In the SOC generation block, the SOC is updated from the current value inputted to the block as shown in equation 2.5.

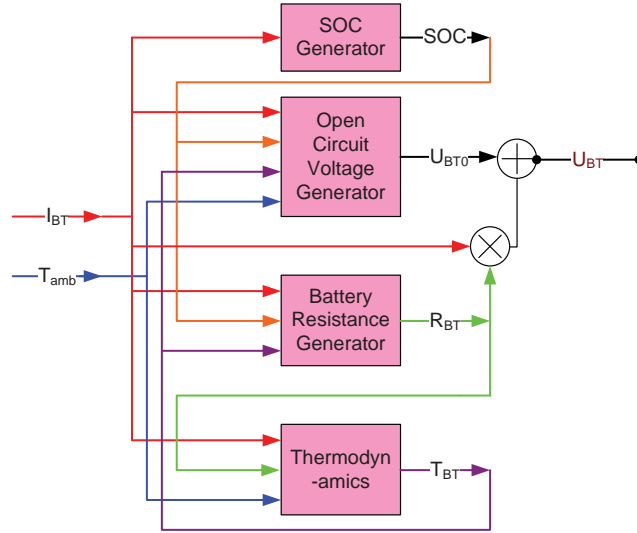


Figure 2.9: Battery Simulink Model.

The open circuit voltage generation block adds the effects of SOC and temperature on the battery open circuit voltage according to equation 2.8. The open circuit voltage depends on the current SOC level so V_{BT-oc0} is estimated according to figure 2.10. Then the battery voltage can be derived accordingly depending on the ambient temperature and the actual battery temperature. Note that at the beginning of the simulation the battery temperature is equal to the ambient temperature.

The battery internal resistance R_{BT} for a certain level of SOC and for a specific battery temperature is calculated using the method in equation 2.10. Figures 2.11 and 2.12 indicate the resistive factor added to the battery during charging and discharging processes depending on the SOC level as shown also in equation 2.9. Similarly, figure 2.13 shows the relation between resistance and battery temperature as shown also in equation 2.9. Therefore, after interpolating the factors α_{R-SOC} and α_{R-T} using figures 2.11, 2.12 and 2.13 respectively, the battery internal resistance can be computed using equation 2.10.

To calculate the temperature changes in the battery in degrees Celsius, a simple equation is adopted based on the thermodynamic system inside the battery. It is the continuous integration of three factors as shown in equation 2.11. The first factor is the heat loss by the current; while the second is the entropy generator which multiplies the battery current and the number of cells and temperature in kelvin by an entropy of cell reaction factor. Finally, the third factor is the difference between the ambient and battery temperature multiplied by the battery thermal resistance which depends on the power in each cell with respect to the area.

Finally, the output voltage of the battery system is calculated using

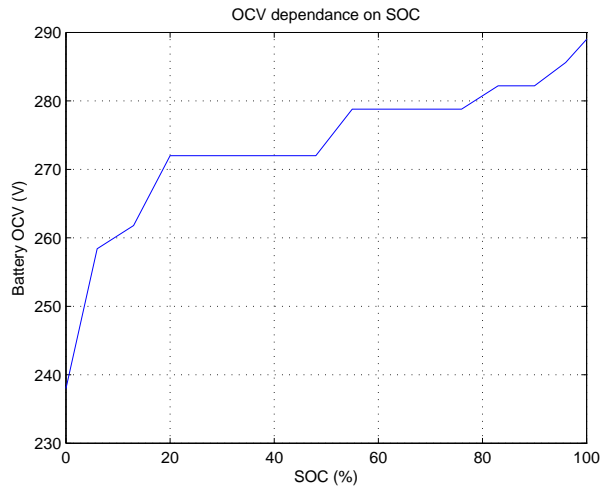


Figure 2.10: Battery OCV-SOC Dependency.

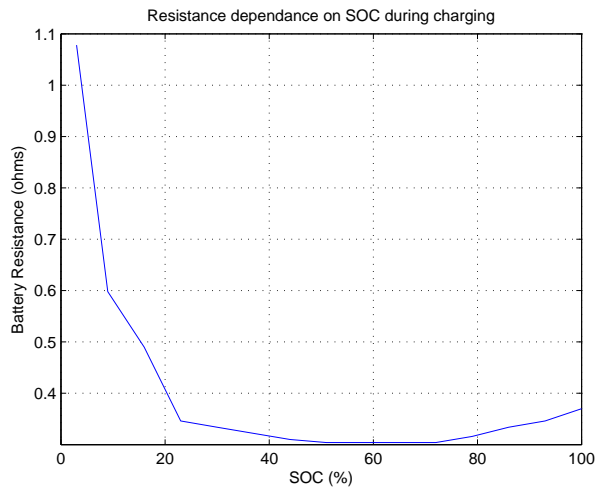


Figure 2.11: Battery Resistance-SOC Dependency during Charging.

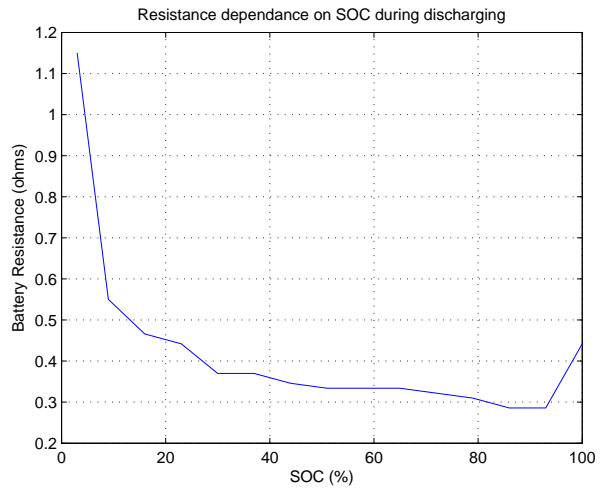


Figure 2.12: Battery Resistance-SOC Dependency during Discharging.

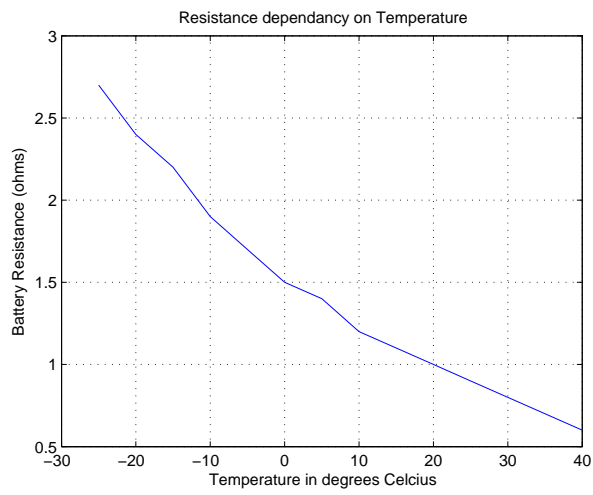


Figure 2.13: Battery Resistance dependency on Temperature.

Table 2.3: Battery Characteristics.

Number of cells in series	80
Number of cells in parallel	1
Type	Li-ion
Resistance factor for series and parallel connection	40
Nominal cell capacity [Ah]	6.5
Nominal capacity of battery [Ah]	6.5
Minimum/Maximum cell voltage [V]	2 / 4.1
Minimum/Maximum BT voltage [V]	160 / 328
Nominal cell voltage [V]	3.6
Nominal battery voltage [V]	288
Temperature coeff. for OCV [V/K]	-0.00013
U damping factor	0.005
Resistance of one cell interconnector[Ohm]	0.00025
Resistance of all cell interconnectors[Ohm]	0.01
SOC at simulation start	0.8
Initial battery temperature [C]	20
battery ambient temperature [C]	20
Battery voltage at start of simulation [V]	280.75
Battery resistance at start of simulation [ohms]	0.3186
Max. Charge/Disch. I [A] at 25C, 60% SOC	155 / -360
Max. Charge/Disch. P [kW] at 25C, 60 % SOC	50.8 / -57.5
Entropy of cell reaction [J/(As K)]	-0.00013
Module surface [m^2]	0.048
Module volume [m^3]	0.000554
Battery Surface Estimation [m^2]	0.64
Battery Volume Estimation [m^3 S]	0.012
Battery [W/Km2]	50
Module heat capacity of battery [J/K*module]	1214
Battery heat capacity of battery [J/K]	48560
Maximal battery temperature [C]	50
Module Weight (kg)	1.02
Power Density (W/kg)	137.6471
kW/kg module power density	4.2313
kg Total weight	15.7122
SOC Limits	20 / 90

equation 2.12. The battery model that is adopted for this dissertation has certain characteristic factors shown in table 2.3.

$$V_{\text{BT-oc}} = \beta_{\text{BT}} V_{\text{BT-oc0}} + (\alpha_{\text{OCV}}(T_{\text{BT}} - T_{\text{amb}}))(n_{\text{BT}}) \quad (2.8)$$

$$\alpha_{\text{R-SOC}} = f(\text{SOC}) \quad \alpha_{\text{R-T}} = f(T_{\text{BT}}) \quad (2.9)$$

$$R_{\text{BT}} = \alpha_{\text{R-SOC}} \alpha_{\text{R-T}} \quad (2.10)$$

$$T_{\text{BT}} = \int \frac{1}{H_{\text{BT}}} [(I_{\text{BT}}^2 R_{\text{BT}}) + [n_{\text{BT}} I_{\text{BT}} \delta_{\text{siBT}} (T_{\text{BT}} + 273)] + 32(T_{\text{amb}} - T_{\text{BT}})] \quad (2.11)$$

$$V_{\text{BT}} = V_{\text{BT-oc}} + R_{\text{BT}} I_{\text{BT}} \quad (2.12)$$

2.2.3 Drivers Model Subsystems

The driving cycle is usually indexed by a velocity profile. The user can choose between the common known cycles such as FTP-75, FUDS, Highway, JAP-1015, NEDC or can generate a user defined cycle. The driver's model subsystem is responsible to send control signals to the energy management system. These signals represent the magnitude of the accelerating and braking torques. The derivation of these signals is based on the reference speed set by the user and the actual vehicle speed measured at the level of the wheels. In order to minimize the speed difference between the referenced value and the measured value, a proportional integral derivative controller (PID) is adopted. This type of controllers is widely used in the control systems in-order to minimize the error between the measured and the desired process value.

The PID controller as shown in figure 2.14 consists of three parallel blocks: Proportional, Integral and Derivative. The proportional part reduces almost the overall error while the integral part drives the system to a smaller error. Finally, the derivative part minimizes the overshoot and reduces settling time for the overall system. Equation 2.13 calculates the torque demand. This torque is limited to the maximum torque of the vehicle electric motor which is 230Nm in this case. The error $e(t)$ is the difference between the measured speed and the reference speed. Table 2.4, indicates the values of the parameters of the PID controller. These values resulted from multiple testing and tuning of the controller to fit the Simulink model.

$$\tau_{\text{req}}(t) = K_p e(t) + K_i \int e(t) dt + K_d \frac{d(e(t))}{dt} \quad (2.13)$$

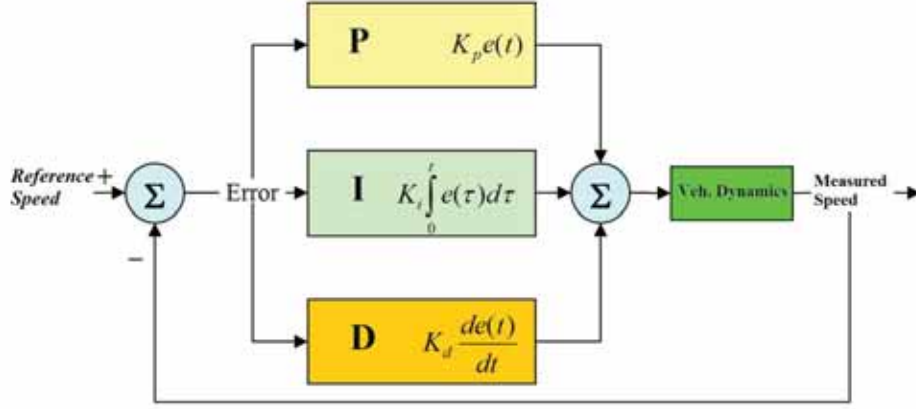


Figure 2.14: PID Controller.

Table 2.4: Drivers Model Characteristics.

Controller proportional factor K_p	130
Controller integral factor K_i	2
Controller derivate factor K_d	1
Avoid integrator overflow factor a_w	0.05

2.3 Vehicle Dynamics Subsystem

In this research, the forward model for vehicle dynamics is adopted. The vehicle block calculates the actual vehicle speed and acceleration as shown in equation 2.14. The speed is a function of the traction, resistive and braking forces acting on the vehicle. The block includes four different sub-modules which are: the driving resistance, traction concept, traction limit and moment of inertia. The model is based on the balance of forces acting in the longitudinal direction.

The actual road height and ambient air pressure are computed using equation 2.15 and equation 2.16.

$$v_a = R_w + \int \frac{(F_{\text{trac}} - F_{\text{res}} - F_{\text{brake}})R_w}{\theta_t} dt \quad (2.14)$$

$$H_a = H_{\text{in}} + \int v_a \sin(\alpha_s) dt \quad (2.15)$$

$$P_a = P_{\text{in}} + e^{\frac{-gM(H_a - H_{\text{in}})}{R_{\text{air}}T_{\text{amb}}}} \quad (2.16)$$

The total moment of inertia θ_t is the sum of the moments of inertia of the wheels and motor, along with the mass of the vehicle as shown in equation 2.17.

Table 2.5: Vehicle Model Characteristics.

Total mass m (kg)	3500
Frontal area A_f (m^2)	3.48
Drag coefficient C_d	0.44
Traction Coefficient μ_r	0.9
Air density ρ_{air} (kg/m^3)	
Tyre radius R_w (m)	0.314
Wheels moment of inertia θ_w (kgm^2)	3.2
Maximum braking force f_{br-max} (m/s^2)	0.8
Center of gravity Cog (m)	0.314
Wheel base w_b (m)	2.778
Front wheel distance to center of gravity Cog_f (m)	1.22
Rear wheel distance to center of gravity Cog_r (m)	1.558
Axle load distribution μ_{al}	0.5

$$\theta_t = m_v R_w^2 + \theta_w + \theta_m \quad (2.17)$$

2.3.1 Vehicle-Driving Resistance

This block calculates the resistive forces acting on the wheels for a specified velocity. These forces are the rolling resistance force in equation 2.18, the air drag force in equation 2.19, the gravitational force in equation 2.20 and the swirl resistance force F_{Swirl} which is due to wheel environmental effects. The latter is dependent on the vehicle velocity and is implemented with a lookup table indexed by the vehicle speed. The graphical curve of the relation is sketched in figure 2.15. Finally, the driving resistance force is computed from the sum of the aforementioned forces as shown in equation 2.21.

$$F_r = m_v g \cos(\alpha_s) f_{rol} \quad (2.18)$$

$$F_w = \frac{1}{2} C_D A_f \rho_{air} v_a^2 \quad (2.19)$$

$$F_g = m_v g \sin(\alpha_s) \quad (2.20)$$

$$F_{res} = F_r + F_w + F_g + F_{Swirl} \quad (2.21)$$



Figure 2.15: Wheel Swirl Resistance.

2.3.2 Vehicle-Braking Force

The braking force is deduced from the braking torque demand on the rear and the front brakes as shown in equation 2.22.

$$F_{\text{brake}} = \frac{\tau_{\text{br}} + \tau_{\text{bf}}}{R_w} \quad (2.22)$$

2.3.3 Vehicle-Traction Force

Finally, the traction concept of the vehicle which could be front drive, rear drive or four wheel drive is specified by the user. For this dissertation, the rear wheel torque is the only one considered and it is equal to the output torque of the transmission system.

The actual torque acting on the rear wheels which is the vertical force at the rear wheels is derived in equation 2.23.

$$F_{\text{trac}} = \min \left\{ \begin{array}{l} \frac{T_{\text{traction}}}{R_w} \\ \mu_r m_{\text{CoG}} \left[\frac{l_R}{l} g - \frac{h_{\text{CoG}}}{l} a_v \right] \end{array} \right. \quad (2.23)$$

2.4 Electric Motor

In FCHV, there is one propulsion driving source which is the electric motor. Its size is determined at the early stage of power train design to satisfy the peak power requirements [21]. Many kinds of electric motors for FCHV are studied in reference [80]. However, these models have a high degree of complexity especially

Table 2.6: Motor System Characteristics.

Continuous Power (kW)	70
Peak Power (kW)	90
Continuous Torque (Nm)	180
Peak Torque (Nm)	230
Max Speed (rad/s)	1248.8
Motor mass (kg)	50
Cp (J/kg K)	1500
Surface Area (m ²)	0.5
Heat transfer coeff. (W/m ² K)	10
Motor Inertia (kgm ²)	0.1098

if one tried to incorporate them into a bigger model. Failure to provide a fast response time can crash the whole model. For this reason, in FCHV control applications, the electric motor is modeled as a static entity with certain power losses [81]. The power losses and efficiency maps are usually referred to by look-up tables.

The electric motor Simulink block translates the power demanded from the sources to torque and speed to drive the wheels as shown in equation 2.24. Table 2.6, indicates the motor characteristics. The losses in the motor and inverter are handled using 2-D lookup table based on the rotor speed and output torque. This relation is based on the motors efficiency map shown in figure 2.16. The dynamics of the electric motor are ignored because the period of the power train of the FCHV is much larger than the period of the motor dynamics. This is why it is redundant to go into the motor dynamics. Therefore, the motor is modeled with its efficiency maps and equation 2.24.

$$P_{\text{motor}} = f(\tau_{\text{req}}, \omega_{\text{m}}) = \tau_{\text{req}}\omega_{\text{m}} + P_{\text{loss}} \quad (2.24)$$

2.5 The Transmission System Unit

The transmission system translates the torque from the motor system into gear ratio, torque and speed values to the wheels. The gear box is based on the motor speed and thus alters the gearshift lever consequently. After the gear command is generated, it is translated to a gear ratio. In the FCHV the gear is assumed to be always at one and so the gear ratio is 13.

The transmitted torque is subjected to several factors, such as losses due to acceleration of rotational inertia and friction of gear rotation. Moreover, the

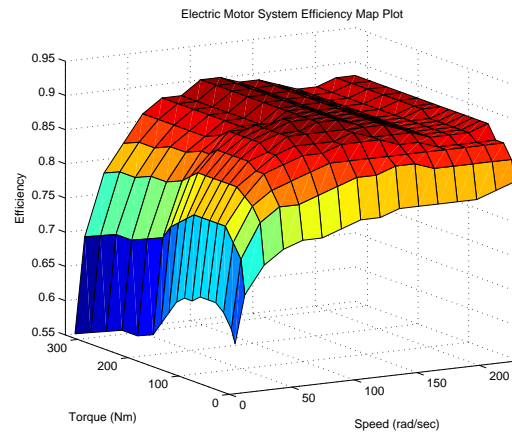


Figure 2.16: Electric Motor System Efficiency Map.

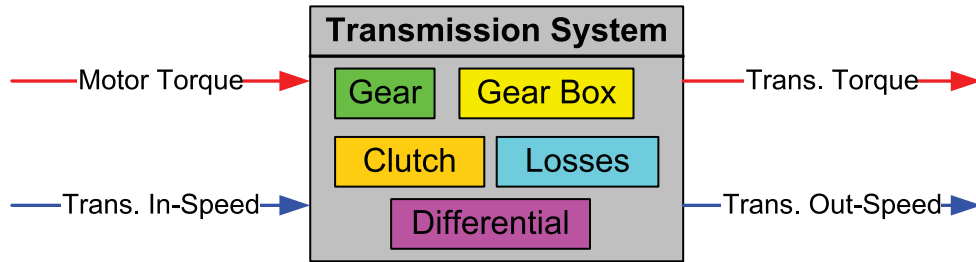


Figure 2.17: Transmission System Model.

gear ratio causes torque multiplication and speed reduction. Figure 2.17 shows a sketch of the Simulink topology of the transmission system. The calculation of the transmission torque and speed is indicated in equation 2.25 and 2.26 respectively. The losses in the transmission system are derived from the efficiency map samples of the gearbox which is approximated at 95 percent.

1. The gear output is 1.
2. The gear ratio is 13
3. Differential efficiency and ratio is 1
4. The position of the clutch is the same because the gear number is constant

$$\tau_T = g_r \tau_M - \frac{P_{T\text{loss}}}{\omega_T} \quad (2.25)$$

$$\omega_M = g_r \omega_T \quad (2.26)$$

Table 2.7: Auxiliaries Power.

Air Conditioning Power	600W
Power Steering	120W
Power Braking	20W
FC Auxiliaries	1000W

2.6 Auxiliaries

The Simulink model considers the auxiliary power that is required from the FCHV components. These include the power required from the cooling system, power braking, power steering, air-conditioning and fuel-cell system auxiliaries as shown in table 2.7. The fuel cell auxiliary current demand is calculated in figure 2.4 in section 2.1.2.

2.7 The Power Conditioning System Block

The power conditioning of the FCHV is composed of two components. The first is a bi-directional DC/DC converter connected between the battery and the DC bus. The second is the three phase inverter which transforms the DC power from the bus into AC current to be fed to the electric motor. The latter is modeled as power losses along with the electric motor losses. It is shown in figure 2.16.

The DC/DC converter allows the passage of the current from the DC bus to the battery system and vice versa depending on the voltage level on both sides. The current at the input of the converter i_{dc-in} is related to the current at the output i_{dc-out} of the converter according to equation 2.27. These equations are then subjected to the minimum and maximum power limits of the converter. Table 2.8 indicates the characteristic data of the DC/DC converter adopted for this dissertation.

$$\left\{ \begin{array}{l} \text{Battery Charging} \\ \text{Battery Discharging} \end{array} \right. \quad i_{dc-in} = \begin{array}{l} \frac{i_{dc-out} V_{bus} \eta_{buck}}{V_{BT}} \\ \frac{i_{dc-out} V_{bus}}{\eta_{boost} V_{BT}} \end{array} \quad (2.27)$$

2.8 The Energy Management System Block

The main subsystem in the FCHV is the energy management system (EMS) block. The EMS block in figure 2.18, is the main drive of the FCHV since it organizes the power allocation between the FC system and the battery system. The

Table 2.8: Power Conditioning Characteristic Data.

Current Limit in buck mode during battery charging (A)	40
Current Limit in boost mode during battery discharging (A)	-40
Buck converter efficiency	0.96
Boost converter efficiency	0.96
Converter specific weight (kW/kg)	2

algorithms that are dealt with in this dissertation exhibit a slow response time especially when compared to the response time of the FCHV. For this reason, the EMS is tweaked for it to be adaptable to all algorithmic scenarios. This is accomplished by using lookup tables linked directly to the output of the algorithmic blocks in the matlab files environment.

The FC status block pinpoints the conditions in which the FC is turned on or off S_{FC} . The algorithm used is shown in table 2.1. There are four lookup tables embedded in the EMS block. These lookup tables are derived beforehand from the algorithmic techniques discussed in the forthcoming chapters. All tables are horizontally indexed by the cycle time of the FCHV. Vertically, they are indexed by the FC power requirements, battery power requirements, motor torque request and braking torque request respectively. Figure 2.19, reveals a topologically view of the above mentioned design. The FCHV model is based on current calculations and not power computations. For this reason the FC and battery power requests are translated into current request by dividing those requests with the voltage at the DC bus.

Algorithm 2.1 EMS FC Status Algorithm

```

1: {Battery SOC}
2: if  $SOC(k) \geq 100\%$  then
3:    $S_{FC} \leftarrow 0$ 
4: end if
5: {Motoring or Idling Mode}
6: if  $v_m(k) \leq 0$  or  $\tau_{req}(k) \geq 0$  then
7:    $S_{FC} \leftarrow 0$ 
8: end if
9: {Generating Mode}
10: if  $\tau_{req}(k) < 0$  then
11:    $S_{FC} \leftarrow 0$ 
12: end if

```

Energy Management System

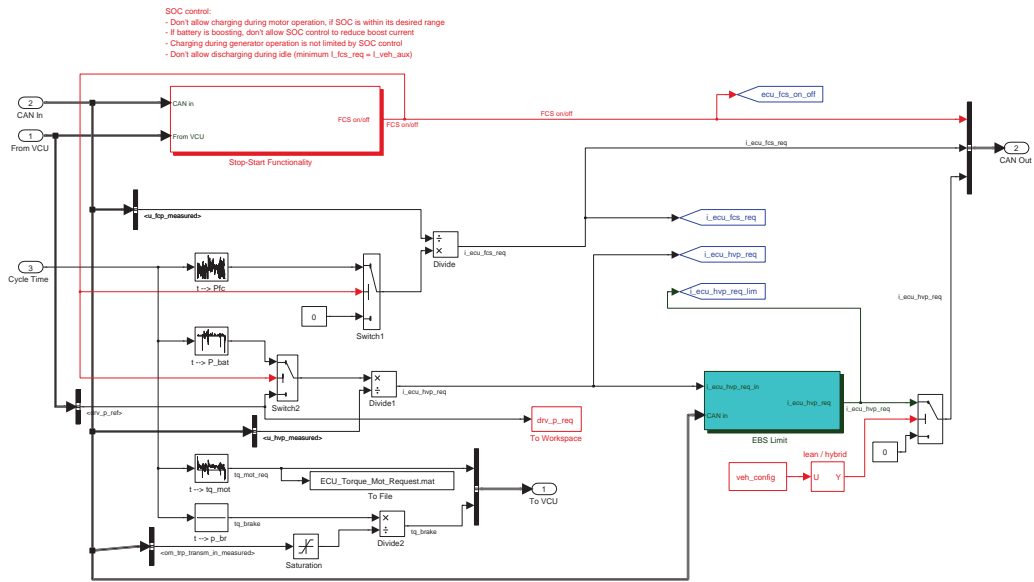


Figure 2.18: EMS Simulink.

2.9 Summary

The problem of studying an existing Simulink model of a FCHV and editing the EMS system was investigated. Starting from formulating the dynamic equations of the power train subsystems, an analytical simplification of the equations based on experimental results was derived. The EMS of the FCHV was modeled and explained and made adaptable to the different algorithmic settings that will be discussed in the next chapters.

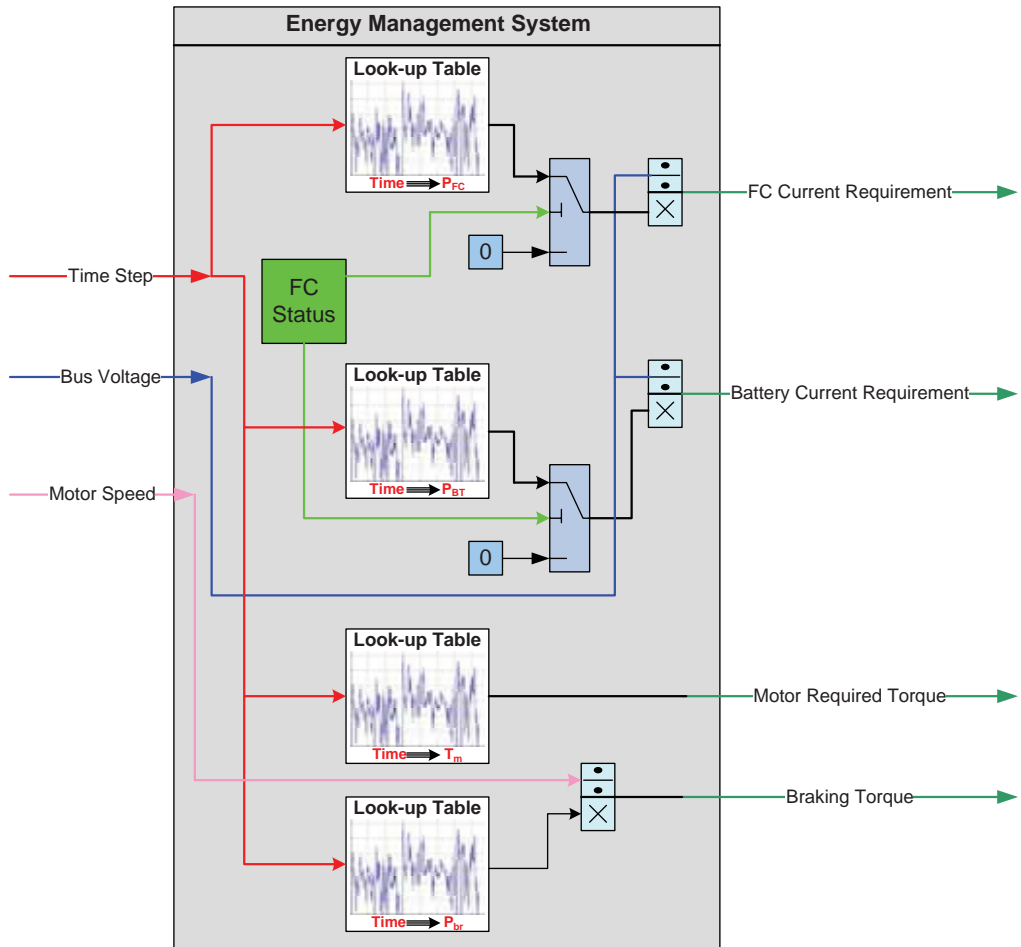


Figure 2.19: EMS Topological Model.

Chapter 3

Efficient Energy Management System

Mathematical optimization is a technique utilized to achieve the best possible outcome for a certain problem. It can take different forms depending on the type of the objective function. The numerical formulation of the FCHV power train discussed in chapter 2 exhibits nonlinear equations. Therefore, it is crucial to select an optimization technique that will closely model the drive train of the FCHV in-order to lead optimum results. The goal is to optimize the power allocation between the FCHV sources which are the FC system and the battery system.

Optimization algorithms when embedded into the vehicle have a slower response time than the vehicle dynamics. For this reason, the optimization phase is calculated beforehand. This means that the optimization of the EMS is done off-line using optimization algorithms. Then during on-line simulation, the pre-registered references are embedded in the Simulink model as lookup tables indexed by the sources power values. The embedded PID controller furthers improve the optimization procedure. The selection criteria of the style of optimization method used depends on the degree of knowledge of the driving cycle and the trip characteristics.

Total knowledge of the driving cycle occurs when the same route is repeatedly driven and a velocity log is recorded. This is the case with city buses for instance where they propel through the same route every day. However, even with total knowledge of the driving cycle, sometimes unpredictable events might occur like rain, collisions or technical problems. This optimization is performed off-line using Matlab software. After the sub-optimal power allocation matrix is obtained, it is injected into the EMS of the Simulink model that is explained in the previous chapter. In the efficient energy management system proposed for the FCHV in this dissertation, three different algorithmic techniques are adopted and tweaked to fit the model and consider different degrees of knowledge of the driving cycle as well as unpredictable events. These are presented in the items

below:

- **Known driving cycle:** If the driving cycle is known beforehand then an improved dynamic programming technique.
- **Mean knowledge of the driving cycle:** If the driving cycle can be approximated by weighted stochastic functions then the improved dynamic programming technique is instigated.
- **Minimal knowledge of the driving cycle:** If the driving cycle is not comprehended, then it is fairly approximated in small steps and a looped improved dynamic programming technique is tested during on-line operation, to tweak deviations from pre-set cycles by updating the algorithm along the trip. This technique is also used to amend the unpredictable events striking known cycles.

The performance criteria for the different adopted techniques are the total operational cost and hydrogen consumption of the FC system. The performance of the FC system is tested using a metric based on the efficiency maps of the FC system. Moreover, to measure the stress factor on the system components, the standard deviation of haar wavelet decomposition of the power supply profile for the sources is considered. The standard deviation value is the measuring parameter to indicate which source has been exploited more than the other [20].

The mathematical optimization is formulated off-line for a pre-defined or approximated driving cycle. Section 3.1 defines an approximation of power demand using a simple power train model based on subsystem losses.

To verify that the results of the weighted improved dynamic programming are close to the global optimal results, a linear approximation of the system sources is derived and applied to a linear program formulation.

3.1 Approximation of the Off-line Power Demand

In a supervisory control problem like the one tackled in this dissertation, it is sufficient to study an abstracted scheme of the system. The power demand at the DC bus is computed by taking the power train losses from the wheels until the input of the electric motor as shown in figure 3.1. The driving cycle is usually a matrix indexed by time and speed. The first step is to calculate the total forces acting on the wheel during each time step and then derive the power demand at the levels of the wheel. The total sum of forces F_T acting on the wheels are the aerodynamic force F_w , the force of rolling resistance or friction losses F_r , the force due to inclination or load slope F_i and the acceleration force F_a . These forces are described in equation 3.1. The power demanded P_w by the vehicle as a function

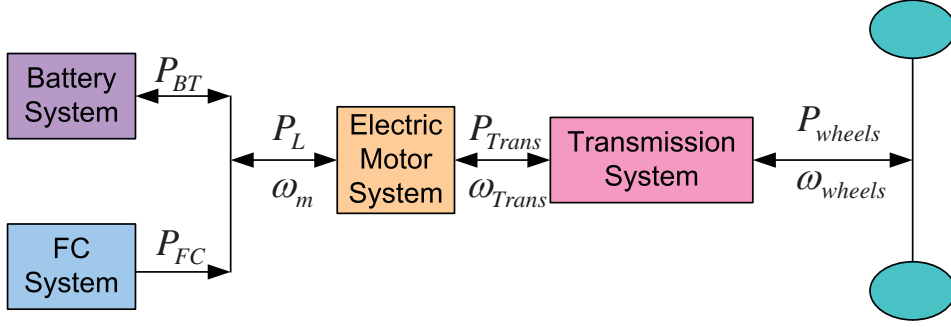


Figure 3.1: Power Train Losses.

of speed at the level of the wheels is given in equation 3.1. For simplicity, the road is considered to be flat and therefore the road inclination is zero.

$$\left\{ \begin{array}{l}
 \text{Aerodynamic Force: } F_w = \frac{1}{2}\rho A_f C_w v^2 \\
 \text{Rolling resistance/ Friction losses: } F_r = mg C_r \cos(\theta) \\
 \text{Inclination/ load slope Force: } F_i = mg \sin(\theta) \\
 \text{Acceleration Force: } F_a = ma \\
 \text{Total Sum of Forces: } F_T = F_w + F_r + F_i + F_a \\
 \text{Power Demand at the Wheels: } P_w = v F_T
 \end{array} \right. \quad (3.1)$$

The power train is composed of the transmission system and electric motor/inverter system as well as the two energy sources. Losses of the power train are modeled using experimental results derived at UAS test-benches. Therefore, the power required by the electric motor P_L is the sum of the power required at the wheels P_w , the transmission system losses P_{TL} and the electric motor losses P_{ML} as shown in equation 3.2.

$$P_L = P_w + P_{TL} + P_{ML} \quad (3.2)$$

The losses in the transmission system are derived from experimental results. Then a 3-D matrix is generated indexed by the transmission system torque and transmission system speed. The third dimension would be the transmission system losses. This is translated in our model using a lookup table where the inputs are the speed and torque of the transmission system and the result is the power loss coefficient. Linear interpolation applies if an input is not indexed and so a linear interpolant is plotted between the adjacent coordinates of the unknown point. Similarly, the power losses of the electric motor and inverter system are derived from a 3D matrix indexed by the electric motor speed, torque and power losses as shown in figure 2.16. Now, after computing the power demanded at

the DC bus, it is time to try to model the sources with their losses to optimally allocate this demanded power.

3.1.1 FC System Characteristics

Life cycle analysis of the FC system is considered in this paper. The current service life of FC that is embedded in automotive systems is 5,000 hours under cycling conditions, which is equivalent to 242,000 km [82]. The current cost of the system is \$50/kW [82]. However, it is still double the cost of ICE. Therefore, a cost measure for the service life $\gamma_{\text{SL-FC}}$ of a FC is indicated in equation 3.3.

$$\gamma_{\text{SL-FC}} = 0.01 \text{ \$/kWh} \quad (3.3)$$

There are three important parameters that need to be approximated. These are: the rate of consumption of hydrogen molecules per kW in g/kWh, the cost of energy from hydrogen consumption in \$/kWh, and the initial mass of hydrogen molecules available in the tank in grams.

The Rate of Consumption of Hydrogen Molecules per KW

The consumption rate of hydrogen molecules per kW depends on the type of fuel cell used and on the manufacturer's datasheet. Table 3.1 shows the experimental data recorded from running a FC under certain conditions. Our goal is to find a constant relation between the hydrogen fuel consumption rate and the power capacity of the fuel cell. The derivation is shown in equation 3.4 and equation 3.5.

$$P_{\text{FC}} = I_{\text{FC-req}} V_{\text{FC}} \quad (3.4)$$

$$\dot{m}_{\text{H}_2} = M_{\text{H}_2} \dot{n}_{\text{H}_2} \quad (3.5)$$

Figure 3.2 shows the plot of \dot{m}_{H_2} versus P_{FC} . The rate of consumption of hydrogen molecules per kW, λ , is the slope of the graph which is 0.015 g/kWs. It is obtained by using a basic linear curve fit of the available data. Therefore, $\lambda=54$ g/kWh.

The nonlinear relation between the power provided by the FC and the respective hydrogen consumed is modeled. The data is used in the Simulink model and derived from experimental testing on the FC system. Equation 3.6 provides the curve fitting model.

$$\dot{m}_{\text{H}_2}(P_{\text{FC}}) = 3.9 \times 10^{-5} P_{\text{FC}}^2 + 0.012 P_{\text{FC}} - 0.0031 \quad (3.6)$$

Table 3.1: FC Experimental Data.

$I_{\text{FC-req}}(A)$	$\dot{n}(/sec)$	$V_{\text{FC}}(V)$
1.49	0.003	360
3.06	0.005	359
7.82	0.015	358
13.48	0.025	356
25	0.05	352
46.51	0.1	344
68.45	0.15	336
94.51	0.2	328
118.75	0.258	320
190	0.4	300
285.71	0.5952	280

The Cost of Energy from Hydrogen Consumption

Hydrogen is produced using electrolysis of water or from steam reformation of natural gas. At a cost of energy of 8 cents/kWh, the price of hydrogen production ranges from 14 to 16 \$/kg [83]. The higher price is for hydrogen production via electrolysis of water. An average cost for hydrogen of 15 \$/kg is used. The value for the cost of energy from hydrogen consumption can be approximated from the consumption of hydrogen molecules per kWh. It is shown in equation 3.7.

$$\gamma_{\text{FC}} = \lambda \times 0.015 = 0.81 \quad \$/\text{kWh} \quad (3.7)$$

The Initial Mass of Hydrogen Molecules Available in the Tank

The initial mass of hydrogen molecules available in the tank is calculated by using the ideal gas equation in equation 3.8. The tank has a volume (V) of 0.08 cubic meters and is maintained at a pressure (P_a) of 300 atm and temperature (T_{amb}) of 20 degrees celcius. Therefore, after calculating the number of moles (n) in equation 3.8, the initial molar mass of hydrogen in the tank is estimated in equation 3.9.

$$P_a V = nRT_{\text{amb}} \quad (3.8)$$

$$M_{\text{O}_{\text{H}_2}} = nM_{\text{H}_2} \approx 1970g \quad (3.9)$$

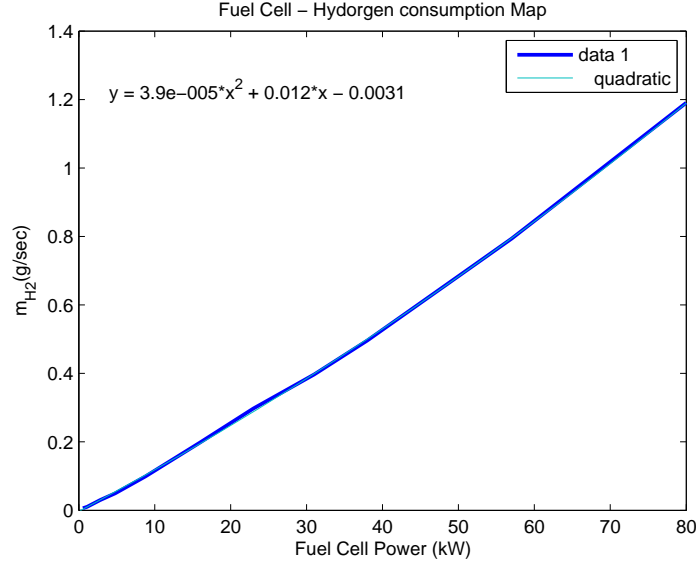


Figure 3.2: Fuel Cell - Hydrogen consumption Map.

3.1.2 Battery Storage System Characteristics

The selected battery is a lithium-ion cell battery [84] suitable for vehicular applications. The test-bench based datasheet shown in table 3.2 indicate the relation between the DOD and the cycles that the battery can withstand till the end of its life.

It can be fairly assumed that the amount of energy that is delivered by the battery system during its lifetime is constant depending on the DOD. From Table 3.2, at a discharge efficiency of 80%, the average energy delivered by the battery system over its life is 7863 kWh. The current cost of the battery is 500 \$/kWh [85] [86]. Therefore, the cost of the battery for its service life is shown in equation 3.10.

$$\gamma_{BT} = \frac{500 \times 1.9}{7863} = 0.12\$/kWh \quad (3.10)$$

The losses of energy sources are also taken into consideration. Q maps are used to model the losses in the battery, which include the power value of the battery while considering internal resistance losses, charge losses and other battery losses. These Q-maps are derived from test-benches where actual battery values are measured [87]. Figure 3.3, shows a Q-map for a battery derived in [87]. To approximate the losses, the basic fitting equation given in equation 3.11 is used.

$$Q_{BT}(P_{BT}) = -0.0076P_{BT}^2 - 1.1P_{BT} + 0.4 \quad (3.11)$$

Table 3.2: Battery LifeCycle Estimation.

DOD (%)	Number of Cycles	Energy Delivered during Battery Life (kWh)
100	1000	1520
90	1000	1368
80	2000	2432
70	3000	3192
60	4000	3648
50	5000	3800
40	6000	3648
30	10000	4560
20	30000	9120
10	100000	15200
5	500000	38000

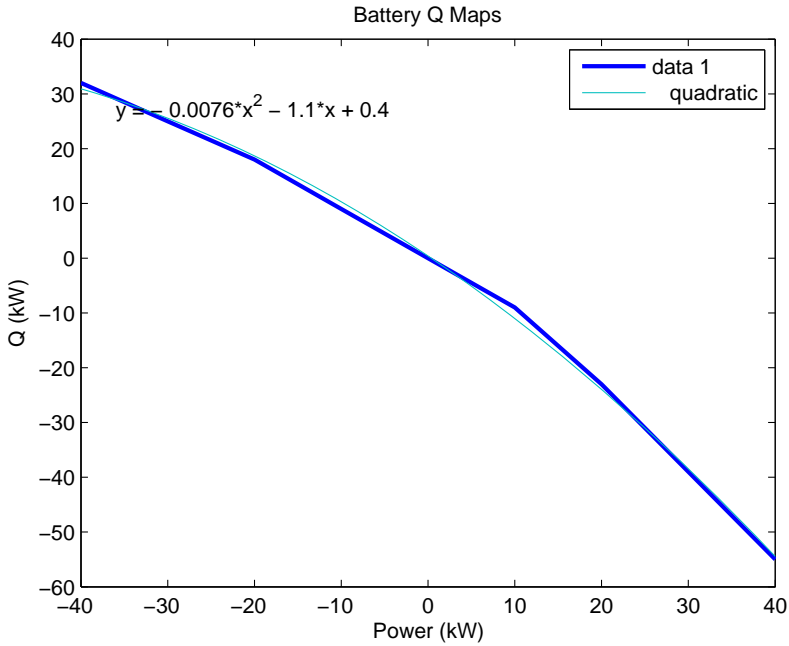


Figure 3.3: Battery Q Maps.

3.2 Linear Programming

Linear programming is a set of optimization techniques that is characterized by linearity in the objective function and constraints. The feasible region addressed by the constraints is a convex polyhedron. The program chooses the global optimum point that minimizes the objective function. The canonical form expressing LP is shown in equation 3.12.

$$\begin{aligned}
 & \text{maximize} && \mathbf{c}^T \mathbf{x} \\
 & \text{subject to} && \mathbf{Ax} \leq \mathbf{b} \\
 & \text{and} && \mathbf{x} \geq \mathbf{0}
 \end{aligned} \tag{3.12}$$

The objective function and constraints of the FCHV power allocation problem is formulated using only linear equations. Afterwards, the optimization problem is solved using linear programming algorithm. Linear programming provides the feasible optimal solution of the linear model of the FCHV power allocation problem which can be used to compare the efficiency of the other proposed methods when linearized.

The EMS for FCHV problem can be expressed with linear objective function and linear constraints. For this reason, LP is adopted to test the effect of simple optimization techniques on the controller of the FCHV. The linear program takes the initial SOC of the battery as well as the initial hydrogen availability in the tank. The system costs and characteristic block in figure 2.1, which is also an input to the linear program block represents the vector of fixed input values which are the cost of H_2 consumption γ_{FC} in \$/kWh, the initial cost of FC system γ_{SL-FC} in \$/kWh, the cost of battery γ_{BT} in \$/kWh, battery energy capacity E_{BT} , the minimum power provided by the FC system P_{FCmin} , the maximum power provided by the FC system P_{FCmax} , the minimum power provided by the battery system P_{BTmin} , the maximum power provided by the battery system P_{BTmax} , the minimum battery state of charge SOC_{min} , the maximum state of charge of the battery SOC_{max} , FC ramp down and up rates ($R_{down-fc}$, R_{up-fc}), the battery ramp down and up rates ($R_{down-bt}$, R_{up-bt}), the consumption rate of H_2 molecules per kW (λ), and the initial mass of hydrogen in the tank in grams MH_o . The linear program yields the optimal split of power between the FC and the battery for a specific driving cycle. The program feeds the results to the Simulink model to yield optimal power flow management.

The problem is formulated as a constrained optimization problem with linear constraints. The main aim is to find the optimal split of power between the components of the FCHV, thus to find the power required from the FC (P_{FC}) and the power required from the battery (P_{FC}). The cost function is depicted in equation 3.13.

$$J = \min \left[\sum_{k=1}^N [(\gamma_{\text{FC}} + \gamma_{\text{SL-FC}}) P_{\text{FC}}(k) + \gamma_{\text{BT}} P_{\text{BT}}(k)] \Delta t \right] \quad (3.13)$$

The cost minimization function calculates the cost of energy from the FC. The cost of the FC includes the hydrogen consumption cost as well as a penalty factor. The latter is a fraction of the life of the fuel cell. In this manner, the cost function will consider the life cycle of the FC. The cost of the battery is considered during charging and discharging phases. This cost comprises the depletion of the battery towards its end life.

3.2.1 System Constraints

The system constraints are described in equations 3.14 till 3.21 respectively.

SOC Period Coupling Constraint:

$$SOC(t) = SOC(t-1) - \frac{P_{\text{BT}}(t)\Delta t}{\eta_{\text{BT}}C_{\text{BT}}} \quad (3.14)$$

Power Balance Constraint:

$$P_{\text{FC}}(t) + P_{\text{BT}}(t) - P_{\text{br}}(t) = P_{\text{L}}(t) \quad (3.15)$$

Fuel Cell Power Limits:

$$P_{\text{FCmin}}(t) \leq P_{\text{FC}}(t) \leq P_{\text{FCmax}}(t) \quad (3.16)$$

Battery Power Limits:

$$P_{\text{BTmin}}(t) \leq P_{\text{BT}}(t) \leq P_{\text{BTmax}}(t) \quad (3.17)$$

Battery State of Charge Limits:

$$SOC_{\text{min}}(t) \leq SOC(t) \leq SOC_{\text{max}}(t) \quad (3.18)$$

FC Ramp Rate Constraint:

$$R_{\text{down-FC}}\Delta t \leq P_{\text{FC}}(t) - P_{\text{FC}}(t-1) \leq R_{\text{up-FC}}\Delta t \quad (3.19)$$

Battery Ramp Rate Constraint:

$$R_{\text{down-BT}}\Delta t \leq P_{\text{BT}}(t) - P_{\text{BT}}(t-1) \leq R_{\text{up-BT}}\Delta t \quad (3.20)$$

Hydrogen Tank Capacity Constraint:

$$\sum_{k=1}^N \lambda P_{\text{FC}}(t) \Delta t \leq MH_o \quad (3.21)$$

The SOC period coupling constraint calculates the available state of charge of the battery after each discharge in a given time step Δt . The subtracted value represents the fraction of energy from the total energy available in the battery spent at time (t). The power balance constraint ensures that the load is served at each step (t). The system dumps any available extra power via P_{br} , which is usually the case when the battery is fully charged and the load demand is generative. A convention adopted for this dissertation states that a positive battery power flows implies that the battery is discharging its current into the FCHV system. Constraints shown in equation 3.16, equation 3.17 and equation 3.18 are limitation constraints for the power that can be provided by the FCHV components. The ramp rate constraints limit the ramp rate of both the FC and the battery. This is very important to prevent a phenomenon known as oxygen starvation of the FC system. The latter occurs when a high instantaneous power is required from the FC. Due to the stoichiometry of the chemicals present, the FC does not respond fast to the requirement yielding oxygen starvation causing FC degradation. Similarly the battery needs a certain amount of time to be able to deliver the required power. The storage capacity constraint ensures that the hydrogen tank is able to cover the entire desired trip [29]. The calculation of the initial available hydrogen consumption is done using the ideal gas equation.

3.3 Dynamic Programming

The FCHV energy management system formulation is not easy to solve using optimal control theory due to its non-linearity. The feasibility region is wide and to satisfy all the constraints many Lagrange multipliers are required and karush-kuhn-Tucker conditions need to be satisfied.

Dynamic programming is an algorithmic optimization tool based on Bellmans principle of optimality for solving recursive problems. The algorithm is easy to implement but suffers from the dimensionality drawback. The problem size grows exponentially with the number of time steps [60]. It is one of the techniques used to optimize the power split between the different energy resources in FCHV [62]. It is implemented by many researchers and applied to different types of hybrid vehicles. In [62], the vehicle power sources are the internal combustion engine (ICE) and battery system. DP is used to test the effect of battery weight and storage capacity on the operational cost. The analysis leads to the selection

of the most feasible battery capacity to lower system costs. Dokuyucu et al. [65], formulated a controller based on dynamic programming to find the torque split between the internal combustion engine and the electric motor. The control signal considered is the battery SOC which is bounded between 0.4 and 0.7. Results show that during low torque demands, the vehicle operates in motor mode and charging is favored. While during high torque demands, both the battery and the ICE assist in feeding the load. Vinot et al. [63], use DP to find the optimal split between the internal combustion engine and battery to study two different series parallel architectures for the hybrid electric vehicle. They used an electric variable transmission concept which leads to slightly higher fuel consumption range, but it can be tweaked by using a gear between the engine and motor. In [64], DP has successfully found the optimal split between the power sources for HEV consisting of fuel cell and battery.

Improved dynamic program is used so as to overcome the problem of dimensionality. IDP takes into consideration the non-linearity of system sources. This novel method considers a tunnel of fixed states rather than an exponential increase in the number of states. In [66], power levels of fuel cell are considered in the state vector while in [67] the authors take SOC levels as state vectors. Both latter papers consider the improved DP and the results are not far from using the regular DP.

In this dissertation, the finite horizon optimization problem is formulated as a constrained structure and the improved DP (IDP) is adopted. The formulation presented in [66] to optimally manage the energy flow between the fuel cell and the battery storage for FCHV is enhanced and applied. The IDP is used to overcome the problem of dimensionality normally faced in dynamic programming algorithms. Power levels of fuel cell are considered in the state vector and SOC levels are control vectors. The paper deals with the power allocation of the fuel cell and battery to minimize the cost function in equation 23. For this reason, the power of the fuel cell or the power of the battery can be considered as the state vector. By fixing one, the other can be derived from the power balance equation in 25, hence this power fixing method lends itself for an easier solution of the problem and is natural to program. In this case, the supervisory control of the vehicle is exerted by the fuel cell, and then the battery satisfies the remaining power demand within the SOC constraints. The optimal path is located by minimizing the cost through a weighted fitness function, which corresponds to the optimal policy [68]

3.3.1 IDP General Formulation

Improved dynamic programming is an upgraded version of DP through which the number of states at each level does not change with time. It bypasses the problem of dimensionality suffered using dynamic programming. In such a supervisory control model, an objective function along with the constraints is defined.

The independent variables are defined through a set of actions and the dependent variables are defined in number states.

The time horizon is sampled into T discrete stages that are equally spaced along the length of the driving cycle. The vertical axis is quantized into S different states. The state vector u is composed of fuel cell power levels that range from 0 to P_{FCmax} in equal steps. Figure 3.4, reveals a model of the network along with all interconnected nodes. The total number of nodes is $S \times T$ which depends on the number of selected states and time samples. Each of these nodes (N) is indexed according to the its current stage location and corresponding state. For example node N_{iu_j} corresponds to the node at stage i and state u_j . At the first stage each node is characterized by a cost function C_{iu_j} symbolized as nodal cost. This is a discrete closed form function that defines a certain objective. The nodal cost represents the cost of being in the associated state. Starting the second stage until $t = T$, each node has two associated costs which are the nodal cost and the transition cost. The transition cost R_{u_k,iu_j} is the cost of moving from the previous states u_k at $i - 1$ to the current state u_j at i . The total cost F_{iu_j} associated with each node at a certain stage is the sum of its nodal cost and the minimum value of all transition costs to the node from previous stage as shown in equation 3.22. If a transition to a node or a certain state of the current node violates any of the constraints, then the node is infeasible and could not be considered on the optimum path. For this reason and to remove it from the optimal path, a very high cost is associated with the transitional cost. The idea behind correlating a high cost rather than removing the transition node from the path is just for the idea of having a faster algorithmic convergence in Matlab without adding extra functionalities. It is assumed that there is at least one possible transition g_{u_k,iu_j} that is feasible so removing a link from the path is meaningless. Finally, at stage T , the minimum cost F_{Tu_j} is selected and traced back to the first stage following the minimum cost path. The algorithm is depicted in steps in 3.1. All index correlations are summarized in equation 3.23.

$$F_{iu_j} = C_{iu_j} + \min_k [R_{u_k,iu_j}] \quad \text{where } i = 1 : T \quad j, k = 1 : S \quad (3.22)$$

$$\left\{ \begin{array}{l} \text{State Vector: } u = [u_1 \quad u_2 \dots u_j \dots u_S] \quad \text{where } j = 1 : S \\ \text{Stage Vector: } Stage = [1 \quad 2 \dots i \dots T] \quad \text{where } i = 1 : T \\ \text{Node Representation: } N_{iu_j} \\ \text{Node Cost: } C_{iu_j} \\ \text{Transition Cost: } R_{u_k,iu_j} \quad \text{where } k = 1 : S \end{array} \right. \quad (3.23)$$

To further explain the methodology behind IDP, we consider a finite time horizon of 3 discrete time steps and a problem with 2 state levels. Figure 3.5

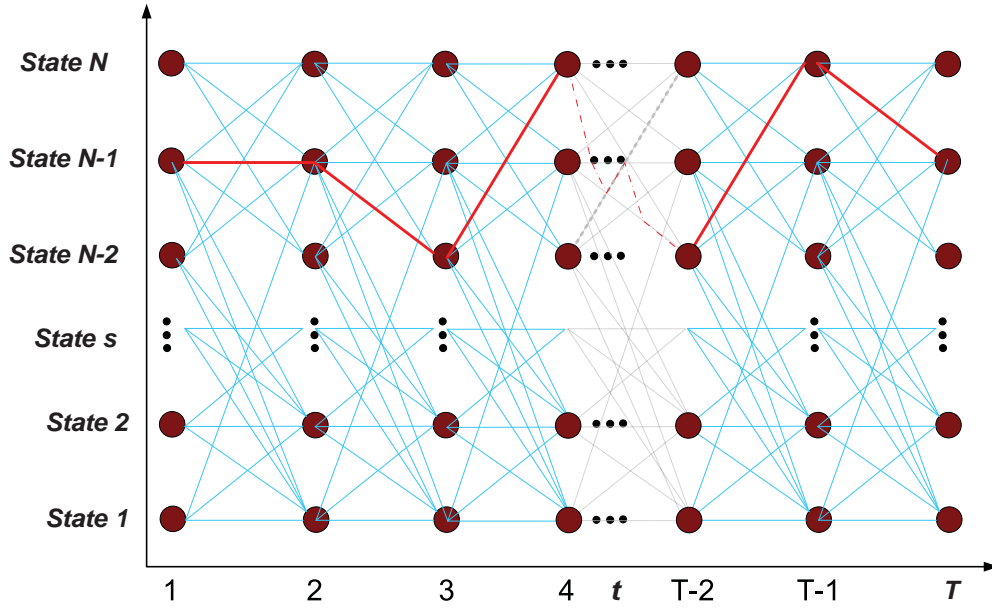


Figure 3.4: Improved Dynamic Programming Sketch.

Algorithm 3.1 Improved DP Algorithm

- 1: **{Forward Path Generation}**
 - 2: **for** i such that $i = 1 : T$ **do**
 - 3: **for** j such that $j = 1 : S$ **do**
 - 4: **for** k such that $k = 1 : S$ **do**
 - 5: Compute C_{iu_j}
 - 6: Compute $R_{u_k, iu_j} \forall k$
 - 7: Locate minimum of R_{u_k, iu_j}
 - 8: Save index of min $Min = [i, k_{min}]$ for min of R_{u_k, iu_j}
 - 9: Compute $F_{iu_j} = C_{iu_j} + R_{u_k, iu_j} + C_{(i-1)u_k}$
 - 10: **end for**
 - 11: **end for**
 - 12: **end for**
 - 13: **{Backward Path Trace}**
 - 14: **for** m such that $m = 1 : T$ **do**
 - 15: Locate $N^*(T) = \min(F_{Tu_j}) \forall j$
 - 16: Locate *all* $N^* = Min(:, 2)$
 - 17: **end for**
-

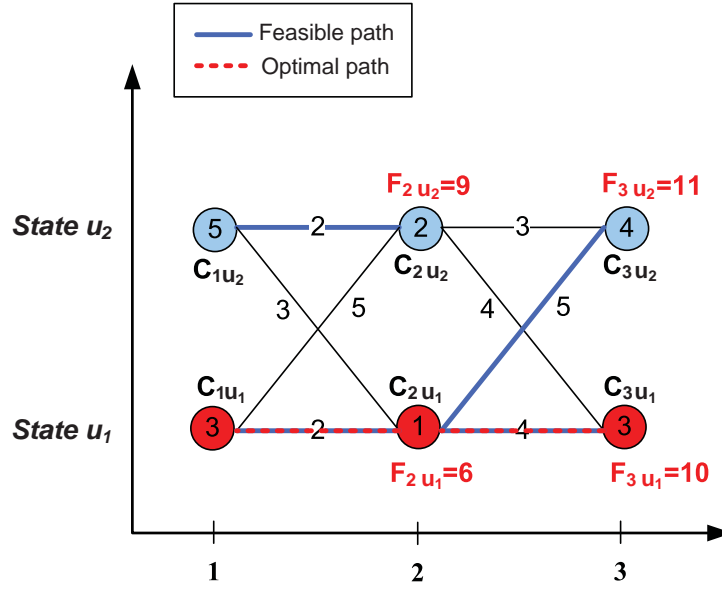


Figure 3.5: Improved Dynamic Programming Sketch.

depicts this model. It starts at $t=1$ where different states u_1 and u_2 are initialized and the corresponding costs C_{1u_1} and C_{1u_2} are calculated. In stage two, two nodes are considered N_{2u_1} and N_{2u_2} . The cost of node N_{2u_1} is its own cost added to the minimum sum of the transitional cost and the nodal cost from the transition node in the previous state. Node N_{2u_1} can be reached from node N_{1u_1} or node N_{1u_2} . The minimum cost to reach node N_{2u_1} is 7 from node N_{1u_1} as indicated by the blue line in figure 3.5. Similarly, the minimum cost to reach node N_{2u_2} is from node N_{1u_1} . Next, the total cost of the nodes at stage 2 is updated such that $F_{2u_1} = 9$ and $F_{2u_2} = 6$. Similarly, at stage 3 the minimum cost to reach nodes N_{3u_1} and N_{3u_2} , is from node N_{2u_2} . The total nodal cost at stage three is updated again and $F_{3u_1} = 15$ and $F_{3u_2} = 13$. Finally, the minimum cost at stage three is selected and traced back to stage one following minimum cost node procedure. This is shown in the dashed red line in figure 3.5. This is a simple problem, if it was tackled using normal DP then the total number of states will be fourteen rather than 6. Therefore, the main benefit behind using IDP over DP is to solve the problem of dimensionality without brutally affecting the optimal path.

3.4 IDP Formulation for FCHV EMS

The improved dynamic programming is formulated for the FCHV EMS. In this context, the nodal cost and the transitional costs are defined. Two approaches are considered, a linearized IDP approach and a non-linear IDP approach. The linearized IDP approach considers linear functions similar to those used in the LP

formulation. It is used for comparison against the LP approach. This assessment is important to verify that the IDP converges to a sub-global optimum point, and provides results similar to the LP algorithm. The non-linear IDP better models the dynamics of the vehicle.

3.4.1 Linearized IDP Formulation for FCHV EMS

In the linearized IDP formulation, the nodal cost represents the cost of energy for being in the current state. It is the cost of consumption of hydrogen fuel as well as the life cost of the battery and FC.

$$C_{iu_j} = \left[(\gamma_{FC} + \gamma_{SL-FC})P_{FC,iu_j} + \frac{1}{2}\gamma_{BT}P_{BT,iu_j} \right] \Delta t \quad (3.24)$$

At each time step, the battery SOC needs to be updated according to 3.25. It is important to note that when the battery power is positive, the battery is considered to be discharging power and thus feeding the load. During this period the power supplied to the load by the battery is lower than the actual energy produced by the battery due to losses. This is accounted for in equation 3.25 by splitting the operation of the battery into charging and discharging modes. When the power supplied by the battery is negative, the battery is considered to be charging and thus the load is generative. However, during this period the actual energy delivered to the battery is lower than that generated from the wheel's kinetic energy and so the efficiency is multiplied by the battery energy.

$$SOC_{iu_j} = \begin{cases} SOC_{(i-1)u_j} - \frac{P_{BT,iu_j} \Delta t}{\eta_{BT} C_{BT}} & \text{if } P_{BT,iu_j} \geq 0 \\ SOC_{(i-1)u_j} - \frac{\eta_{BT} P_{BT,iu_j} \Delta t}{C_{BT}} & \text{if } P_{BT,iu_j} < 0 \end{cases} \quad (3.25)$$

In each state at a certain discrete time, it is important to adhere to the power equation represented in equation 3.26:

$$P_{FC,iu_j} + P_{BT,iu_j} - P_{br,iu_j} = P_{L,i} \quad (3.26)$$

Transitional costs are linked to the feasibility of a step from a node to the other. If the jump from a node to the next is infeasible then a very high cost is associated with the transitional cost. On the contrary, if a link is feasible between the nodes then a zero cost defines the transitional cost. This feasibility of a move is verified through the fact that the power source variables adhere to their limits as defined by equations 3.16 to 3.20. If a step violates the above limits then it will be an infeasible state.

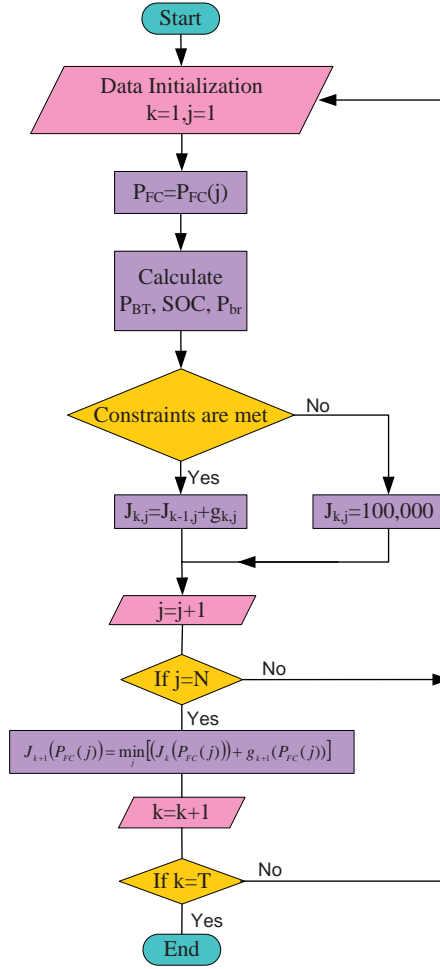


Figure 3.6: Improved Dynamic Programming Forward Algorithm.

The forward algorithm behind the improved dynamic programming adopted for FCHV is summarized in figure 3.6. Note that after the forward algorithm terminates, then the node at $t=T$ that corresponds to the minimum cost among the set of nodes at the final stage is chosen. Afterwards a backward algorithm traces the optimum nodes corresponding to that node all the way towards the beginning. This backward traced path represents the optimal path.

3.4.2 Weighted IDP Formulation for FCHV EMS

In the IDP objective function, the coefficients of the power demand of the fuel cell and the battery are in the order of micro units. They are calculated in sections 1.1.1 and 1.1.2. The fuel cell has two coefficients associated with it as shown in equation 3.3 and equation 3.6. The first equation corresponds to the fuel cell

service life. The second equation, when multiplied by the hydrogen cost, results in the cost of hydrogen consumption for a given fuel cell power level. The battery cost coefficient is shown in equation 3.10 and corresponds to its service life.

The relative cost of the fuel cell with respect to that of the battery in the cost objective function is very high. The cost coefficient of the fuel cell can range from 25 to almost 200 times more than that of the battery depending on the power supplied by each. For this reason, the IDP treats the battery in a charge depleting mode since the objective is to minimize the cost function. This section introduces a different view of the cost objective function by treating the battery cost as a control parameter. This permits changing the relative value of cost of the fuel cell with respect to the battery.

There are some real life examples where the trip conditions force the power circumstances of the cycle. For example, if the trip is long and there are no fuel stations available on the road, therefore, it is better for the battery to work in charge depleting mode and save hydrogen fuel consumption until reaching a fuel station. Another case arises when there is plenty of fuel supply on the road so the battery can work in charge sustaining mode while considering minimization of the hydrogen fuel. In certain cities the municipality might force vehicles to utilize the battery more than the fuel cell to save hydrogen fuel. In this case, the battery needs to be in charge depletion mode.

Therefore, it is essential to study the IDP while having more or less emphasis on the battery. This is achieved by adding a certain weighting factor to the battery cost in the objective function. The weighting factor (w_{BT}) introduces a mechanism of controlling the mode of operation of the battery. It changes the relative cost of the battery with respect to the fuel cell in the cost objective function. It enables the battery to change between charge depleting and charge sustaining modes. The cost calculation at the end of the cycle is performed based on the IDP cost objective function and not the weighted one.

The objective function of the weighted improved dynamic program (WIDP) is now denoted by (V). It includes a weight added to the battery cost coefficient in an attempt to achieve another desired response of the system. The function with the battery weight added is shown in equation 3.27. It is used to calculate the nodal cost of the states in a similar manner to the IDP calculations of the nodal costs using equation 3.24. The transitional and total costs are calculated in the same way as that for the IDP. Moreover, the same backward path tracing method is used in the WIDP.

$$V_{iuj} = \left([(\gamma_{FC} + \gamma_{SL-FC})P_{FC,iuj}] + \frac{1}{2}w_{BT} [\gamma_{BT}P_{BT,iuj}] \right) \Delta t \quad (3.27)$$

This new method is formulated and tested based on the system requirement and trip conditions. In the next chapter, the search technique using brute force search method for weight selection is presented. Comparative simulation

runs on the two major driving cycles is presented. These include the analysis of the outputs of the IDP and weighted IDP methods comparing the hydrogen consumption levels, the energy provided by the fuel cell and battery SOC profiles of both methods.

3.5 Looped Dynamic Programming Algorithm

Standard driving cycles are created by engineers to assess the vehicle performance. The daily driving conditions faced by drivers are different from the standard cycles. On the other hand, even the driving habits that are unique for each driver affect the driving cycle. The IDP algorithm presented in the previous sections can be applied only for known driving cycles. It is one of the powerful optimization algorithms, however it needs apriori knowledge of the driving cycle.

This section introduces a novel method to find the sub-optimal power split matrix between the sources of unknown cycles. The technique caters for totally unknown driving cycles and special event occurrences using a looped dynamic programming algorithm. Unknown driving cycles that do not mimic any of the commonly known cycles can be forecasted using traffic information signals. The derivation of such a forecast is beyond the scope of this work; however it is assumed that a certain demand is forecasted for a period of time between 0 and T. The forecast is approximated in small time limited windows.

This means that for a certain cycle, there is a fair prediction of the driving conditions before the cycle occurs. The window size for prediction is determined before the vehicle starts the trip. Therefore, the unknown driving cycle is forecasted in steps determined by the window size and prior to the occurrence of the cycle in the corresponding window. This implies that the driving speed profile is now identified and the IDP can be applied to the window. The problem with the window size is the possibility of converging into less efficient solutions. If the whole cycle is known, then IDP can locate the sub-optimal power allocation of the sources in-order to lower the hydrogen fuel consumption levels. In looping methodology, the window size is much smaller than the duration of the total driving cycle because of the lack of efficient equipment and technology that could forecast the whole cycle in one shot. For this reason, there is a huge risk that the IDP converges into a solution which is far from the sub-optimal solution pursued.

When the unknown cycle finishes and the speed profile is gathered, IDP can be performed on the whole cycle. It would be best if the profiles of the power sources in all windows gathered together is close to the profile of the sources when the IDP is applied to the whole cycle. For this reason, other data constraints need to be considered for the optimization to be comparable. This is mainly the amount of battery discharge during each window.

The size of the prediction window affects the speed of the IDP, the smaller the size, the faster is the rate of convergence of the IDP algorithm. This rate is

an essential factor for the EMS when it is applied in real time situations. On the other hand, the window size reflects the accuracy of the forecast. A smaller window implies that the forecast is more efficient and closer to reality.

The objective behind this section is to develop a novel method to update the sub-optimal power allocation matrix of the vehicle sources in unknown driving cycles. The cycle speed is assumed to be forecasted in a certain window size prior to vehicle operation in this window. These values are used by the IDP to find the optimal power allocation matrix that minimizes the hydrogen fuel consumption for the corresponding window while limiting the battery SOC in that window.

Figure 3.7 depicts the methodology followed to implement the looping technique. There are two initialized time frames, the off-line activity and the on-line activity. Both activities extend from 0 to T seconds where T symbolizes the length of the unknown cycle which is also unidentified.

The initialization block on the top left corner, is performed before the vehicle starts the trip. The driver sets the road path from point A to point B. The road data is not known so the speed profile for the path can not be calculated. For this reason, the path from A to B is assumed to take T seconds to be completed. Then, the time frame of T seconds is split into k windows of size N. Each current window is symbolized by k varying from $1 \rightarrow N$. The next window is symbolized by $k : N + 1 \rightarrow 2N$.

The vehicle acquires the initial road conditions from the data management center and it forecasts the speed profile ($\hat{v}_{1:1 \rightarrow N}$) for the first window of the cycle. The speed forecasts for the whole cycle are calculated per window based on the traffic information and the measured vehicle speed for the current window. The latter is computed in the vehicle drive block during the on-line simulations. Therefore, the forecast block acquires the measured vehicle speed during the current window ($\hat{v}_{m,k:1 \rightarrow N}$) and forecasts the speed for the next window ($\hat{v}_{k:N+1 \rightarrow 2N}$).

The switch shown in the figure is a signal routing switch. It passes the first input if the condition of the second input is satisfied. Therefore, the initial forecasted vehicle speed profile for the first window of size N ($\hat{v}_{1:1 \rightarrow N}$) passes through the switch since the time (t) is not greater than zero. When the vehicle starts accelerating during the first window, the time (t) is greater than or equal to zero. The third input of the switch passes through because the second input is not satisfied. Therefore, initially ($\hat{v}_{1:1 \rightarrow N}$) and during the next phases ($\hat{v}_{k:N+1 \rightarrow 2N}$) passes.

The speed signal enters the vehicle dynamics block which calculates the load power profile based on the speed profile as explained in the first section of this chapter. The efficiencies of the power train are calculated in the drive system block. They are added to the corresponding demand before entering the improved dynamic programming block. Therefore, the output of the vehicle model block is the forecasted power demand of the current window ($\hat{P}_{L,k:1 \rightarrow N}$).

At this stage, the input power demand to the IDP block is the demand

at the DC bus which connects the fuel cell and battery systems to the power train of the vehicle. The other input of the IDP block is the final state of charge for each corresponding window. This value is required in-order to achieve better results from the IDP algorithm in-terms of total minimization of the hydrogen consumption for the whole cycle. The IDP algorithm tends to use the battery more in each window so as not to consume more hydrogen thus causing the battery to be depleted in the first window which hinders its advantageous use in the other windows. For this reason, by limiting the amount of battery discharge per window, it is guaranteed that the cycle can make use of the battery during most of the other windows.

The IDP block calculates the sub-optimal power allocation matrix which is composed of the split of power between the fuel cell and the battery during the corresponding window. Thus, the matrix holds the power split between the fuel cell and the battery at each second of the N sized window. The calculation of the power split matrix is performed during the off-line activity. The IDP block also considers the final state of charge of the battery (SOC_f) per window. This specification leads to better utilization of the battery during all the windows of the cycle. If this is not specified, then the IDP program will tend to discharge the battery during the initial windows and thus hinder its usage in the other windows.

This power split matrix is fed to the power split matrix block (PSM). The latter gathers the data of all the matrices of each corresponding window collected during the whole cycle. The PSM block sends the estimates of the fuel cell power ($\hat{P}_{FC,k:1 \rightarrow N}$) and battery power ($\hat{P}_{BT,k:1 \rightarrow N}$) to the vehicle energy management system operating through the on-line activity.

During the on-line operation, the vehicle drives block measures the vehicle speed ($v_{m,k:1 \rightarrow N}$) and sends it to the forecast block. The forecast block uses the measured speed along with some traffic information in-order to estimate the vehicle speed for the next window. The vehicle drives block also calculates the load demand ($P_{L,k:1 \rightarrow N}$) and sends it to the PID controller.

The PID controller compares the actual calculated demand with the forecasted one derived during the off-line operation. The PID controller tries to minimize the difference between the measured and forecasted demands using proportional, integration and derivation values of the error signal. The output of the PID controller is a power measure (ΔP) symbolizing the added power request for minimizing the error between the measured and the forecasted vehicle power demand.

The power requested from the fuel cell system ($\hat{P}_{FC-req,k:1 \rightarrow N}$) during the on-line operation is the sum of two signals. The first is the estimated value of the power split for the fuel cell ($\hat{P}_{FC,k:1 \rightarrow N}$) which is calculated in the IDP off-line block. The second signal is the error in power measure (δP) which is computed by the PID controller. The addition of these two signals provides the total power request required from the fuel cell system ($\hat{P}_{FC-req,k:1 \rightarrow N}$). The output of the

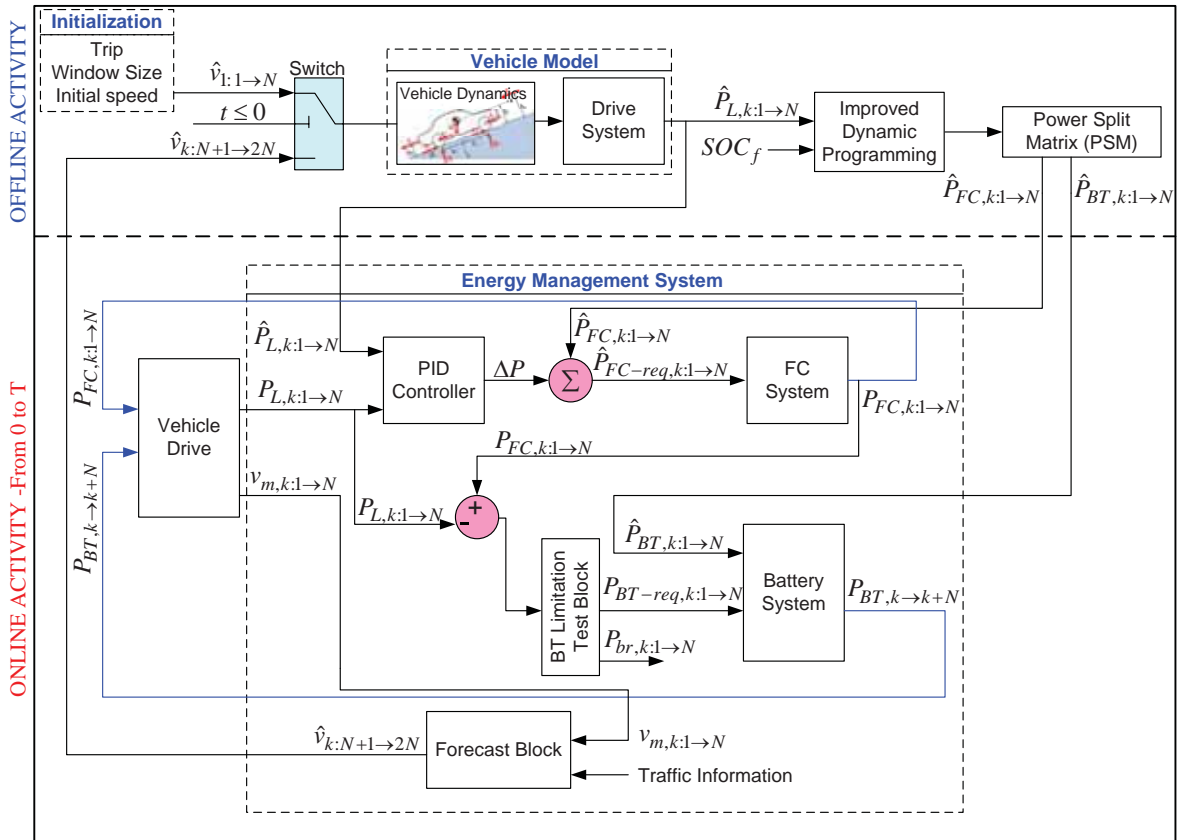


Figure 3.7: Looped Dynamic Programming Sketch.

fuel cell system is the actual fuel cell power used ($P_{FC,k:1 \rightarrow N}$). This value is fed back to the vehicle drives block in-order to calculate the vehicle speed and power demand.

The battery system block calculates the actual battery power demand ($P_{BT,k:1 \rightarrow N}$) and feeds it back to the vehicle drives block. It takes two inputs. The first input is the estimated value of the power split for the battery ($\hat{P}_{BT,k:1 \rightarrow N}$) which is calculated in the IDP off-line block. The second input is the battery request ($P_{BT-req,k:1 \rightarrow N}$) calculated by the power balance constraint. The power balance constraint computes the difference between the actual power demand ($P_{L,k:1 \rightarrow N}$) and the fuel cell power ($P_{FC,k:1 \rightarrow N}$). The difference is fed to a battery limitation test block. The latter block tests the need for power brake. This case occurs during two scenarios. First, when the load is generative and the battery is full. The second scenario is when the load is generative but greater than the maximum battery charging power. If one of the two scenarios is satisfied then the power brake ($P_{br,k:1 \rightarrow N}$) is a non-zero value. The driver hits the brake and automatically the controller specifies whether it needs to activate the frictional braking system or the regenerative braking system.

This methodology is applied and tested for known driving cycles in chapter 5.6. Two scenarios are presented. First, the cycle is assumed to be unknown and thus it is split into a number of windows and the looped IDP is performed on each window as explained previously. The vehicle speed of the next window is assumed to be forecasted and the sub-optimal power allocation matrix is calculated. The second scenario is to consider the whole driving cycle. This means that the IDP algorithm is applied to the whole cycle. The two scenarios are compared in terms of fuel cell power profiles and battery SOC. This comparison verifies the efficiency that the windows of the looped IDP would be fairly comparable profiles to the global optimum of the cycle.

The novel EMS presented also considers special event occurrences on the road. These occurrences might happen during the trip. They represent accidents, sudden road traffic or unexpected effects of weather conditions. These events alter the driving cycle. The operating vehicle usually decelerates and sometimes stops before reaching the point where the event happened. The vehicle can really benefit from this deceleration by using the recuperation of energy to charge the battery. However, it can only benefit if the event occurred some time (t) before the vehicle reaches the point of the event. The traffic control signal updates the vehicle controller about the occurrences of the event. The speed profile of the trip can be speculated. The IDP algorithm performs additional runs to cater for the special event. When the vehicle reaches the special event, it would have been updated with the new sub-optimal power allocation matrix. These events are to be known at time (t) and before the vehicle reaches the event location, so the looped IDP algorithm can update the power split signals in-order to minimize the total cost.

This method is applied in chapter 5.4 where an event at time (t) occurs, a certain time before the vehicle reaches the location. The vehicle off-line speed profile is updated to cater for a deceleration before the event and a stop near the event and then an acceleration phase. This off-line speed profile is fed into the vehicle dynamics block and motor system to approximate the power demand at the DC bus. The latter power demand is fed to the off-line IDP block which calculates the sub-optimal power allocation matrix of the sources. This matrix is fed back to the on-line operation of the vehicle before it reaches the event. In this way, the vehicle deceleration before reaching the location of the event helps to save more hydrogen fuel by utilizing the recuperation energy to charge the battery.

3.6 State Machine Control Algorithm for Comparison Methodology

The proposed methodology of efficient energy management system using IDP is compared against a state machine control algorithm. The latter is proposed and tested by Panik [88]. Different states are formulated depending on the demanded power and the battery SOC. The different states are defined in the items below:

- **State 1: Motoring** $P_L > 0, v_L > 0, P_L \geq P_{FC-\min}$: If the demanded load is positive and greater than the minimum power that can be supplied by the FC, then the FC system is turned on and limited to the minimum power values. The battery system supplies the difference between the required load and minimum power value of the FC.
- **State 2: Motoring** $P_L > 0, v_L > 0, P_{FC-\min} < P_L < P_{FC-\max}$: If the demanded load is positive and ranges between the minimum and maximum power that can be supplied by the FC, then the FC system is turned on and limited to the demanded power values while preserving the ramp rate constraint. The battery system supplies the difference between the required load and supplied power value of the FC.
- **State 3: Motoring** $P_L > 0, v_L > 0, P_L \geq P_{FC-\max}$: If the demanded load is positive and is greater than the maximum power that can be supplied by the FC, then the FC system is turned on and limited to its maximum power value while preserving the ramp rate constraint. The battery system supplies the difference between the required load and supplied power value of the FC.
- **State 4: Generating** $P_L < 0, v_L > 0, P_L \geq P_{m-\min}$: If the demanded load is generative and is greater than the minimum power that can be endured

by the motor, then the FC system is turned on and limited to its minimum power values. The battery system supplies the difference between the required load and supplied power value of the FC.

- **State 5: Generating** $P_L < 0, v_L > 0, P_L < P_{m-\min}$: If the demanded load is generative and is less than the minimum power that can be endured by the motor, then the FC system is turned on and limited to its minimum power values. The battery system supplies the difference between the minimum motor power and the supplied power value of the FC.
- **State 6: Idling** $P_L = 0, v_L = 0, P_L < P_{FC-\min}$: If the demanded load is in idle mode and is less than the minimum power that can be supplied by the FC system, then the FC system is turned on and limited to its minimum power values. The battery system supplies the difference between the auxiliary power demand and the supplied power value of the FC.
- **State 7: Idling** $P_L = 0, v_L = 0, P_L \geq P_{FC-\min}$: If the demanded load is in idle mode and is greater than the minimum power that can be supplied by the FC system, then the FC system is turned on and limited to its minimum power value while preserving the ramp rate constraint. The battery system supplies the difference between the auxiliary power demand and the supplied power value of the FC.

3.7 Stress Analysis using Haar Wavelet

The haar wavelet transform of a certain function x with n inputs x_n is y_n . Equation 3.28, shows the relation between the input and output of the transformation. The haar transform matrix is derived from the 2x2 haar matrix, shown in equation 3.29, which is associated with the wavelet. This discrete wavelet transform converts any sequence of even length into a two component vector. Depending on the length of the sequence, the elements can be transformed as building blocks of the 2x2 haar wavelet. The general form of the 2Nx2N haar matrix is shown in equation 3.30. The second component of the matrix is the identity matrix with a diagonal value of 1. The product symbolized in the equation is the Kronecker product [89] [90].

$$y_n = H_n x_n \quad (3.28)$$

$$H_2 = \begin{bmatrix} 1 & 1 \\ 1 & -1 \end{bmatrix} \quad (3.29)$$

$$H_{2N} = \begin{bmatrix} H_N \otimes [1, 1] \\ I_N \otimes [1, -1] \end{bmatrix} \quad (3.30)$$

Haar wavelet transform is the simplest transform that can divide a signal into its low and high frequency components. It exhibits advantageous results with signals incorporating sudden transitions. Motapon et al. [20], discovered that it can be used for stress analysis of the FCHV sources. In their analysis, they compared the performance of five different energy management system strategies. They used the haar wavelet analysis to associate the stresses on the sources for the different strategies. They discovered that the classic PI control based EMS exerts the highest stress on the fuel cell while the frequency decoupling and fuzzy logic based EMS exerts the lowest stress on the fuel cell. The latter EMS algorithm exerts the highest stress on the battery system. In this thesis, the stresses on the fuel cell and the battery will be compared for the proposed EMS algorithms based on the same haar wavelet decomposition method.

The technique they used is based on decomposing the power supplied by the FC and the battery for a given load using Haar wavelet transform. The decomposition results in a low and a high frequency component of the signal. It is noticed that the high frequency component has a zero mean and so the standard deviation is used as a measure to indicate the stress component on the source.

In the analysis of the stresses on the FCHV sources, the Matlab function 'dwt' from the wavelet toolbox is used. The 'dwt' function decomposes any signal into its low and high frequency components using a low pass and a high-pass filter respectively. It computes the two coefficients of the wavelet by convolving the input signal with a low pass filter and a high pass the filter. The standard deviation of the high pass filter is used as a measure of the stresses exerted on the FCHV components.

Chapter 4

Improved Dynamic Programming Algorithm for Known Driving Cycles

The improved dynamic programming algorithm discussed in the previous section is applied, tested and analyzed for known driving cycles. A multiple of simulated comparative experiments demonstrates the efficiency, significance and applicability of the algorithmic strategy. The IDP algorithm for electric vehicles is verified by linearizing its objective function and constraints and then comparing it against a linear programming algorithm. It is tested for a small test cycle and then for known driving cycles such as highway and FUDS driving cycles. Sensitivity analysis is applied to highlight the effects of the variables.

The outcome of the algorithm which is obtained from off-line simulation, is the sub-optimal power split between the FC and the battery. This is injected in the vehicle Simulink model which incorporates also a PID controller for on-line testing. The behavior of the system resources and electric motor is analyzed and the hydrogen consumption is compared against the state machine controlled algorithm discussed in the previous section.

MatLab is the simulation environment that beds the adopted IDP algorithm. The performance of the system in terms of runtime is derived on an intel core i7-3610QM CPU at 2.30GHz. Using the conventional DP, during a certain stage three loops will be initialized, the time, state variable and control variables [81]. IDP limit the number of states and the exponential growth in states which makes it easier to mask one of the loops.

4.1 Algorithm Validation

The IDP algorithm is validated by comparing it against a linear programming algorithm. The IDP method proposed converges into a sub-optimal solution for

Table 4.1: Comparative Results for LP and LIDP.

	Highway		FUDS	
	LP	LIDP	LP	LIDP
The Cost of Operation (\$)	2.767	2.804	1.29	1.31
Electric Energy Supplied by FC (kWh)	3.897	3.898	1.785	1.786
Electric Energy Supplied by BT (kWh)	0.63	0.67	1.28	1.31
Total amount of H2 fuel consumption(g)	178.7	180.7	76.94	77.51

obtaining the power split between the fuel cell and the battery.

The IDP has limited number of states so it does not consider the outcomes from all of the combinations. To verify that the achieved results are acceptable within a certain tolerance, the equations of the IDP technique are linearized (LIDP). Then, it is compared against the optimal results obtained from the linear programming technique.

The LP method converges into a global optimal solution for the power allocation problem. It would be the best technique of choice for the problem, however it does not accept non-linear equations which model the FCHV. For this reason, LP is used to test the efficacy of the sub-optimal solution acquired from a linearized IDP technique. The objective function and constraints of both methods are similarly defined.

Table 4.1 shows the comparative measures of the highway and FUDS cycles trips when using LP and LIDP. For the highway cycle, the hydrogen consumption using the linearized IDP method is 1 percent more than the LP method. The energy supplied by the fuel cell is 3.898 and 3.897 kWh based on the LIDP and LP technique respectively. This is less than 1% difference.

Similar analysis is carried out for the FUDS driving cycle. The hydrogen consumption difference is less than 1% in favor of the LP method. Moreover, the fuel cell and battery utilization in terms of energy supplied throughout the cycle is very close in both method. The fuel cell supplied energy in kWh is 1.786 and 1.785 for the LIDP and LP method respectively. Similarity, the battery overall kWh during the cycle is 1.31 and 1.28 for the LIDP and LP methods respectively. This means that the split of energy between both methods is very similar and with little discrepancy. For this reason, it is safe to conclude that the LIDP method converges to an acceptable sub-optimal solution very close to the optimal solution achieved by the LP.

4.2 Sample Driving Cycle

The efficacy of the IDP algorithm is then verified with respect to a small test cycle shown in figure 4.1a. Table 4.2 indicates the base case data chosen for analysis.

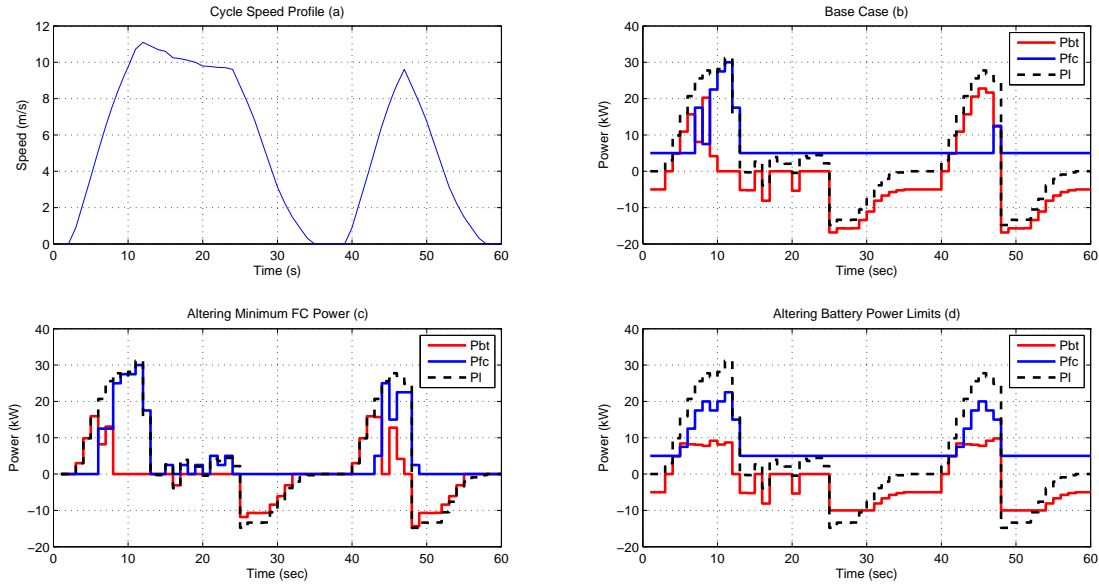


Figure 4.1: Sample Driving Cycle.

Figure 4.1b, shows the power distribution using IDP. During the first three seconds, the vehicle is in its idle state with a zero demand, the FC is set to its minimum power which is 5kW and so its energy is used to charge the battery. The FC and the battery start supplying the load between 5 and 12 seconds. Then the fuel cell goes back to its minimum power supply until second 48. Between 25 and 47 seconds when the load is mostly generative, the battery is charging. However, it is using power not just from regenerative braking but also from the minimum set power of the FC. The battery considers the efficiency of regenerative braking. This depends on the efficiency of the transmission system, motor/inverter system and battery. The efficiencies are speculated as discussed in chapter 2. Although the battery is charged and can supply the load between 40 and 48 seconds, the sudden drop in load at around 49 seconds, forces the FC to supply the load in its ramp rate steps so as not to violate the ramp rate constraint of the battery.

Figure 4.1c, shows the result when the FC minimum power is lowered to zero. In this case, the fuel cell is supplying the load aided by the battery. Between 40 and 50 seconds, the program didn't drain the battery to respect its ramp rate constraint especially with the sudden drop in power at second 49. The minimum permissible level of the fuel cell power is set by its manufacturer. This test is performed to validate that the program respects the limits when they are altered.

The savings in hydrogen consumption in the second case is almost 33% with respect to the base case. This goes back to changing the minimum permis-

Table 4.2: Vehicle Parameters.

Variable	Value
P_{FC-max} (kW)	70
P_{FC-min} (kW)	5
P_{BT-max} (kW)	40
P_{BT-min} (kW)	-40
SOC_{max}	0.9
SOC_{min}	0.79
SOC_0	0.8

sible fuel cell level from 5 to 0 kW. The stresses on the fuel cell are measured in both cases following the haar wavelet transform method explained in chapter 3. The second case exerts more pressure on the fuel cell with respect to the base case. In the base case the fuel cell is maintained at a minimum power of 5kW so the shifts in power from minimum to a certain supply is not that much. The frequency of high transitions in the second case is more noticeable due to the lower minimum permissible fuel cell power level.

The effect of limiting the battery power between [-10,10]kW is shown in figure 4.1d. The FC plays a more important role in-order to supply the demand. This is due to the fact that the battery could not supply the load due to its upper limits constraint. As well as the regenerative power used to charge the battery is shaved due to the battery lower limit constraint.

4.3 Optimum Power Allocation using IDP

After analyzing the small test cycle, the normal driving cycles are set. It is time to monitor and analyze the behavior of the light duty sprinter using IDP for different driving cycles. The analysis includes the activities of the FC and battery operations during the vehicle acceleration and deceleration modes. Moreover, comparison against the state machine control method discussed in the previous section is investigated.

The IDP algorithm is launched in off-line mode for the corresponding driving cycle using MatLab program. The split of power between the FC and battery is derived from the algorithm. This split is fed to energy management system block in the Simulink model that simulates the selected vehicle in on-line mode.

The outcomes from each cycle are analyzed. The curves resulting from the on-line Simulink model of the vehicle are compared against the curves resulting from the off-line IDP algorithm. The chain of analysis is shown in figure 4.2.

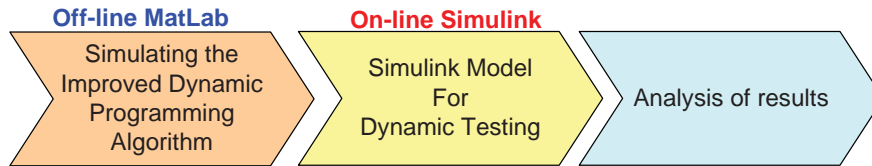


Figure 4.2: Chain of analysis.

4.3.1 Highway Driving Cycle

The power profile of the highway driving cycle is shown in figure 4.3. The upper curve indicates the speed profile over the 766 seconds period. The lower curve shows the calculated demand at the level of the wheels (P_{wheels}) and the electric motor (P_m) as per the equations derived in chapter 3.

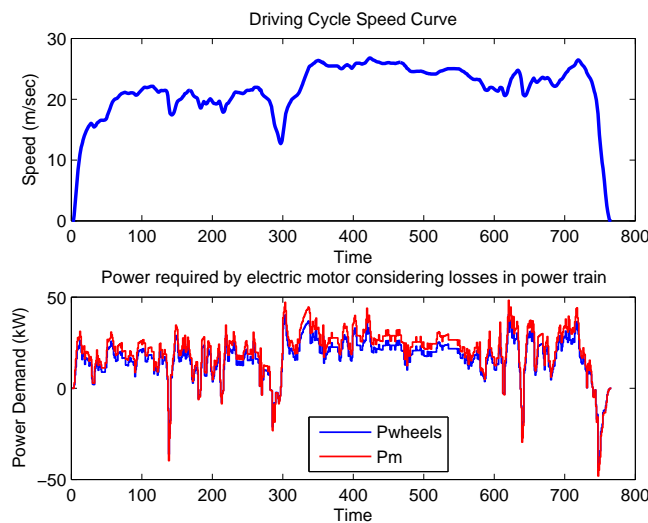


Figure 4.3: Highway Power Profile.

The off-line power split between the fuel cell and the battery is obtained by running the IDP MatLab program. Then the power split is fed to the Simulink model which mimics the electric vehicle dynamics. Figure 4.4a shows the behavior of the fuel cell and battery during on-line and off-line operations.

Figure 4.4a indicates the role of the PID controller in matching the reference speed (V_{req}) to the measured speed (V_{act}). The two speed profiles are almost identical. However, at some instances, specifically at 150 and 300 seconds there is a mismatch in the system occurring due to the errors in the PID controller. This occurs because the PID controller is trying to minimize the errors between the provided vehicle speed and the measured one.

The power allocation profile of the light duty sprinter operating on a highway driving cycle is shown in figure 4.4b. At the beginning of the cycle, the battery enters a charge depleting mode to save some of the hydrogen fuel

especially at start-ups. Then at around 100 seconds, the FC starts supplying the load. The FC continues to supply the load almost throughout the cycle. This coincides with the fact that the sprinter has a small battery and a large FC which makes the later the main energy source in the system. To relieve the stresses on the FC, the battery tends to aid the FC in supplying the load at several instances of time. These figures resulted after the simulation of the optimal power allocation matrix in Simulink environment.

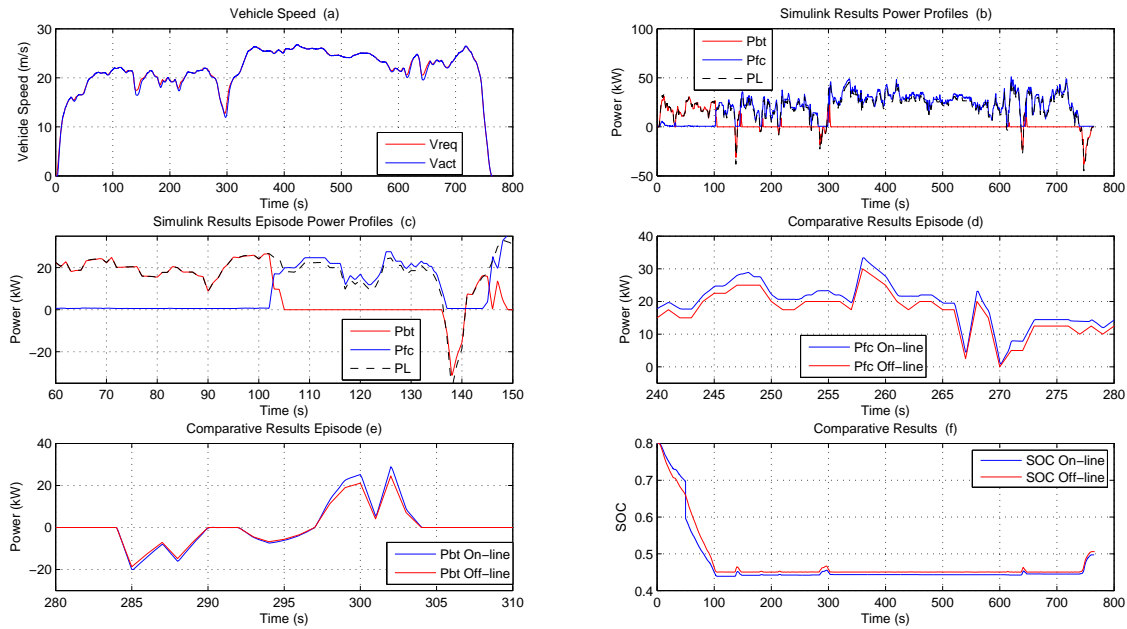


Figure 4.4: Highway Cycle using IDP.

To further analyze the results a zoom into the power allocation profile shows different episodes. In figure 4.4c, the simulation shown is between 60 and 150 seconds. It is noticed that the FC power is higher than the load, to cater for the power needed for FC compressor and auxiliaries. When the load is generative, the battery charges power through regenerative braking. This power is less than the power provided by the load, to account for the losses in the power train. It is noticed around 141 seconds, the load shifts from generative into motoring. The battery plays the important role of aiding the FC in supplying the load in order to respect the fuel cell ramp rate constraint. When the load was generative the fuel cell was not supplying any power.

Figure 4.4d, shows an episode of the fuel cell power profiles. The blue curve in the figure is obtained during the on-line simulation of the cycle in the Simulink environment. The red curve is obtained from the IDP off-line runs in Matlab to obtain the sub-optimal power split between the sources. There is an

approximate match between the on-line and off-line results in terms of FC power of the simulation. The on-line power curve is shifted up by almost 2kW.

Figure 4.4e, shows an episode of the battery power profiles during the off-line and on-line operations. It is noticed that the profiles are almost the same. Some mismatches occur due to the difference in modeling the battery during the on-line and the off-line operations. At around 300 seconds the battery requested more power during the on-line operation as compared to the off-line one. In this sense, the battery is catering for the mismatched in the PID controller by adding the powers of the error to its load.

Figure 4.4f shows the SOC profiles of the cycle during the on-line and the off-line operations. The software is trying to keep the SOC within the favorable limits and thus SOC is not dropping below 45%. The figure shows the approximate match between the battery SOC during on-line and off-line optimization.

Table 4.3, shows an analysis of the results including costs and hydrogen consumption levels. The cost of operation as calculated by equation 3.24, is \$2.8. This includes the battery and fuel cell service life costs as well as the hydrogen consumption cost for the highway trip. The total amount of hydrogen spent during the trip is 182 grams. The highway cycle is 16.45 km long, therefore the amount of hydrogen fuel spent per km of the trip is 11 grams.

During on-line operation, the total amount of hydrogen consumed is 185 grams which is close to the off-line one. The on-line operation showed that it mismatched the off-line one in terms of fuel cell power by a maximum of 3kW. This explains the higher amount of hydrogen consumed during the on-line operation.

The electric energy supplied by the battery and fuel cell throughout the trip are 0.6 and 3.9 respectively. This coincides with the power plots that the fuel cell is the main source of energy in the trip and the battery aids it whenever it is necessary.

The stresses on the system components are derived based on the haar wavelet transform explained in chapter 3. They are higher for the FC than the battery. The latter means that the sudden changes in power levels of the system sources are more on the FC side and thus the FC is exploited more. This is normal for highway cycles because the fast dynamics don't provide a room for battery to charge and discharge frequently. Such sudden changes add stresses to the components. For instance if the FC is supplying 5kW now, it is better to maintain this supply rather than shifting between 5 and 0 kWS or 5 and 20 kW.

Finally, the off-line program took 8 seconds to converge into the sub-optimal solution. This is fairly fast for a controller finding a sub-optimal solution in dynamic programming.

Table 4.3: Highway Driving Cycle Results.

Variable	IDP
The Cost of Operation (\$)	2.8
Electric energy supplied by the FC (kWh)	3.9
Electric energy supplied by the BT (kWh)	0.6
Total amount of H2 fuel consumption(g)	181.6
Fuel Cell Stress Factor	17.3
Battery Stress Factor	11.4
Off-line Runtime (seconds)	8

4.3.2 FUDS Cycle

The speed profile of the FUDS driving cycle is shown in figure 4.5a. The cycle is characterized by low speeds and fast dynamics especially because the cycle shifts between accelerating, decelerating and idling states. This induces negative and positive fluctuations in the power profile.

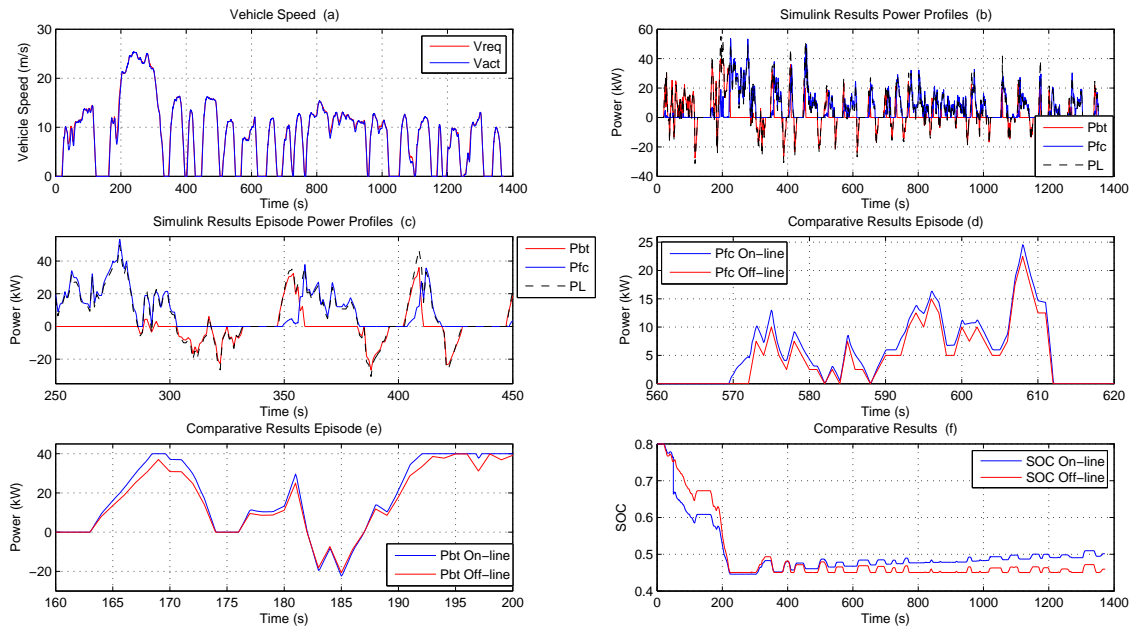


Figure 4.5: FUDS Cycle using IDP.

The power allocation profile of the light duty sprinter operating on the FUDS driving cycle is optimized using the off-line IDP method. Then the off-line matrix is embedded into the FCHV Simulink model for on-line testing. Fig-

ure 4.5b shows the power profile behavior of the sources against the load demand. Since the system has a small battery and a larger FC capacity, the FC supplies the demanded load almost throughout the cycle. Due to the fact that urban cycles are rich with generative loads based on the frequent idling mode, the battery is being charged often. The charging efficiency is added to account for the power train losses.

In figure 4.5c, an episode of the simulation profile is shown between 250 and 450 seconds. The battery is charging every time the load is generative. It is aiding the fuel cell in supplying the load so as to lower the hydrogen consumption especially when high loads are encountered such as around 350 and 410 seconds. The battery plays a more active role in this cycle as compared to highway cycle due to its frequent charging. The battery discharging efficiency is also considered.

Figure 4.5d, shows an episode of the fuel cell power profiles. The blue curve in the figure is obtained during the on-line simulation of the cycle in the Simulink environment. The red curve is obtained from the IDP off-line runs in Matlab to obtain the sub-optimal power split between the sources. There is an approximate match between the on-line and off-line results in terms of FC power of the simulation. The on-line power curve is shifted up by almost 2kW.

Figure 4.5e, shows an episode of the battery power profiles during the off-line and on-line operations. The profile are almost the same. Some mismatches occur due to the difference in modeling the battery during the on-line and the off-line operations.

Figure 4.5f, shows the SOC profiles of the cycle. These curves show a comparative SOC profiles between the off-line IDP optimal power allocation matrix and the Simulink calculated matrix. The latter is traced in the blue curve while the former is shown in the red curve in the corresponding figure. The battery SOC is kept within the favorable limits. The match between the SOC during off-line and on-line simulation is very close. This is common SOC profile for urban cycles because the battery tends to charge and discharge frequently due to the cycle dynamics.

Table 4.4, shows an analysis of the results including costs and hydrogen consumption levels. The cost of operation as calculated based on equation 3.24, is \$1.4. This includes the battery and fuel cell service life costs as well as the hydrogen consumption cost for the highway trip. The total amount of hydrogen spent during the trip is 84 grams. During on-line operation, the total amount of hydrogen consumed is 89 grams which is close to the off-line one. The on-line operation showed that it mismatched the off-line one in terms of fuel cell power by a maximum of 3kW. This explains the higher amount of hydrogen consumed during the on-line operation.

The electric energy supplied by the battery and fuel cell throughout the trip are 1.1 and 1.9 respectively. This coincides with the power plots that the fuel cell is the main source of energy in the trip and the battery aids it whenever it is necessary. However, since the battery is charging frequently during the cycle,

Table 4.4: FUDS Driving Cycle Results.

Variable	IDP
The Cost of Operation (\$)	1.39
Electric energy supplied by the FC (kWh)	1.935
Electric energy supplied by the BT (kWh)	1.097
Total amount of H2 fuel consumption(g)	84.39
Fuel Cell Stress Factor	11.3
Battery Stress Factor	12.2
Off-line Runtime (seconds)	13

it is supplying more power to the vehicle. This explains the higher energy share of the battery as compared to the highway cycle.

The stresses on the system components based on the haar wavelet transform are comparable between the fuel cell and battery. Both of these resources are utilized in the FUDS cycle which explains the haar results. This indicates that in fast dynamics driving cycles comparable stresses occur on the fuel cell and battery. It is justified by the frequent idle state visited during urban cycles which increases regenerative braking via kinetic energy recuperation which drains the fuel cell and battery.

Finally, the off-line program took 13 seconds to converge into the sub-optimal solution. It is a bit slower than the highway cycle. This is because the time sample in the highway cycle is 766 seconds and that for the FUDS cycle is 1373 seconds.

4.4 Weighted Improved Dynamic Programming

In this section, different values of the battery weight of the WIDP objective function are set and analyzed for the highway and FUDS driving cycles using a brute force search technique. These values are responsible to change the mode of operation of the battery between charge depletion and charge sustaining modes. The main trade-off through the weight setting is between the total cost and the desirable SOC profile during the trip. The more the battery is set to work in charge sustaining mode, the higher is the cost of operation and hydrogen consumption levels.

4.4.1 Battery Weight Analysis

The battery enters a charge sustaining mode when its cost coefficient in the objective function becomes higher than that of the fuel cell. The fuel cell cost

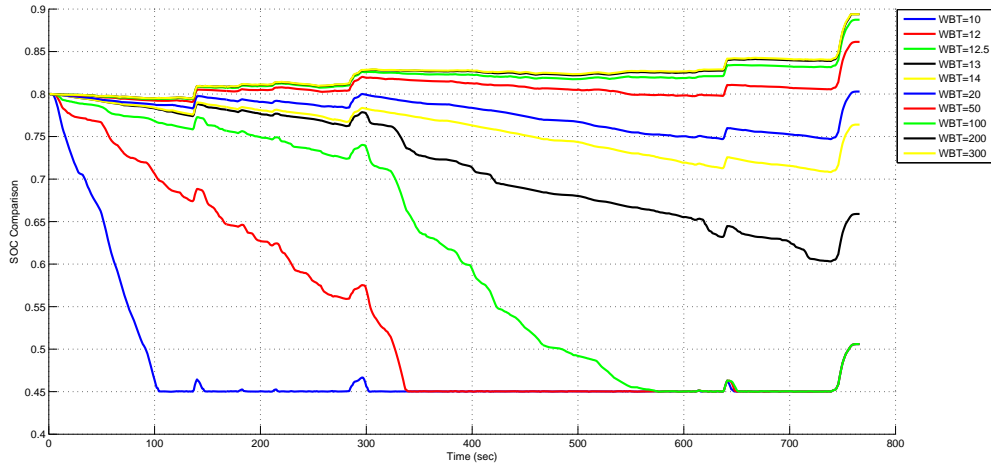


Figure 4.6: Highway Cycle - SOC Profiles for Weighted Battery Cost.

coefficients calculated in sections 1.1.1 and 1.1.2 in equation 3.3 and equation 3.6, are higher than that of the battery coefficient shown in equation 3.10. The relative cost of the fuel cell with respect to that of the battery in the cost objective function is very high. The cost coefficient of the fuel cell can range from 25 to almost 200 times more than that of the battery depending on the power supplied by each.

The battery weights are selected using a brute force method in an attempt to find different SOC profiles. Figure 4.6, shows the different SOC profiles for the highway driving cycle based on different values for battery weight in the objective function shown in equation 3.27. By setting the weight at a value of ten or below, the battery is working in a pure charge depleting mode. This is shown in the leftmost blue curve in the figure. This means that the battery cost coefficient is still very low in comparison to that of the fuel cell.

Below a weight value of 50, the battery still acts in a charge depleting mode but with different behavioral profile. At a weight setting of 12 and 12.5, the battery takes a longer time to be depleted to the minimum SOC level set by the user. At a weight level of 13, the relative cost of the battery with respect to that of the fuel cell started to increase. This kept the battery in a charge depletion mode but sustained the minimum SOC at almost 0.6. At a weight level of 14 and 20, the SOC is sustained at 0.7 and 0.75 respectively. At weight levels of 50 and above, the relative cost of the battery is higher in comparison to the fuel cell. Therefore, the battery is purely in charge sustaining modes and it is charging throughout the cycle.

Figure 4.7, shows the behavior of the battery in terms of SOC profile for different weight settings under the FUDS driving cycle. Due to the nature of the

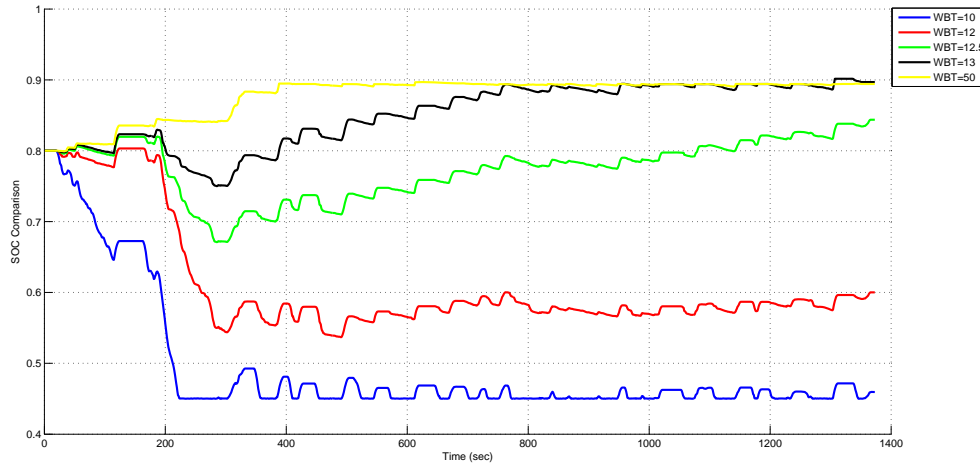


Figure 4.7: FUDS Cycle - SOC Profiles for Weighted Battery Cost.

cycle, the battery is more utilized in such a cycle which is rich in regenerative braking cycles. However, when the relative cost of the battery with respect to the fuel cell increase, then the WIDP tends to decrease the battery usage and thus goes into a charge sustaining mode. The first leftmost curve in the figure corresponding to a weight settings of 10 makes use of the battery in a charge depletion mode. The battery is being discharged to its minimum SOC level during the FUDS cycle.

At a battery weight level of 12, the battery is still in charge depletion mode but the charge is sustained at a lower SOC level of 0.6 and not 0.45 as set by program. At around 12.5, the battery entered a small charge depletion mode at the beginning of the cycle and then after 300 seconds, it started the charging mode. From a weight level of 13 onwards, the battery barely discharges into the cycle. At a weight level of 50, the battery is in pure charge sustaining mode. The battery charges from the fuel cell until it reaches its maximum permissible charging level which is 0.9 in this case.

4.4.2 Comparative Modes

Three weights for the battery in the cost objective function are tested for the highway and FUDS driving cycles. These weights define a mode of operation for the battery. The first is charge depletion mode (CDM) with a battery weight for the highway and FUDS cycles of 10. The second is the charge sustaining mode (CSM) with a battery weight for the highway and FUDS cycles of 30 and 12.5 respectively. Finally, the third mode is the charging mode (CM) with a battery weight for the highway and FUDS cycles of 100 and 50 respectively.

Table 4.5: WIDP Results.

	CDM	CSM	CM
<i>Highway Driving Cycle</i>			
The Cost of Operation (\$)	2.8	3.1	3.2
Electric Energy Supplied by FC (kWh)	3.9	4.4	4.5
Electric Energy Supplied by BT (kWh)	0.6	0.2	0.1
Total amount of H2 fuel consumption(g)	181.6	204.6	208.4
Fuel Cell Stress Factor	17.3	14.3	14.0
Battery Stress Factor	11.4	5.4	5.3
Off-line Runtime (seconds)	8	8	8
<i>FUDS Driving Cycle</i>			
The Cost of Operation (\$)	1.39	1.75	1.9
Electric Energy Supplied by FC (kWh)	1.935	2.519	2.7
Electric Energy Supplied by BT (kWh)	1.097	0.6	0.5
Total amount of H2 fuel consumption(g)	84.39	110.2	116
Fuel Cell Stress Factor	11.3	10.71	10.5
Battery Stress Factor	12.2	8.07	7.5
Off-line Runtime (seconds)	13	13	13

Table 4.5 shows the numerical results during CDM, CSM and CM modes for the highway and FUDS cycle. The cost of operation and hydrogen consumption levels for both cycles for CM is higher than CSM. The numerical outcome of the CSM are higher than CDM.

During CDM, the battery is supplying the load as much as possible. For this reason, the electric energy supplied by the battery is the highest during CDM when compared to CSM and CM for both cycles. The opposite case occurs for the fuel cell since it has to cover the load if the battery is not. CDM has the lowest fuel cell energy supply in both cycles. This directly implies that the CDM has the lowest cost and hydrogen consumption levels.

The runtime for both cycles during the three battery modes of operation is the same. For the highway cycle, the IDP program takes 8 seconds to converge. It takes 13 seconds for the IDP to converge for the FUDS cycle.

For both cycles, the stresses on the sources are related to the changes in supply. CDM has the highest battery supply, therefore it has the highest battery stresses. CM has the highest fuel cell supply, however since the switching to high frequency is minimal then lower stresses on the fuel cell are noted.

4.5 IDP and RB Comparative Analysis

Comparative analysis is needed to verify the methodologies presented. It is based on tabular and graphical comparative analysis of the methods output parameters such as the hydrogen consumption levels, stress levels and power/SOC profiles. Comparison between the IDP and the RB method shows the superiority of the former method in lowering hydrogen consumption levels. The latter comparative argument is not novel and is expected. It is now well known that rules versus optimization of the commutation level change drastically the cost. However, the message is to highlight the savings achieved as well as the methodologies to utilize the IDP technique for on-line testing.

The comparative analysis is launched for the two major driving cycles discussed in the previous section. These are the highway and the FUDS driving cycles. The two cycles have different dynamics which present different analysis for the validation of the methodologies. The comparative analysis is displayed in tabular and graphical forms. The latter visualize of the trajectories of the two profiles under study are virtually identical and measures the discrepancy between them.

The RB method that is used is based on the model discussed in the paper with citation number [88] and presented in chapter 3.6. This model is not an optimized version of a rule based model. It was implemented and tested on an actual sprinter in Germany. The goal was to implement the IDP strategy on the same vehicle. However, the sprinter was no longer available and so the IDP is only tested on a real-time stationary system which is explained in chapter 6. Although the rules are not optimized, they are used in the effort that in future the sprinter will be available and IDP testing can be carried on it. Therefore, the comparison of the IDP and RB methodologies is carried out based on the Simulink model of the vehicle. The vehicle is set for the runs of both methodologies and the battery and fuel cell performance is compared in these runs for the highway and FUDS driving cycles.

Table 4.6 shows the outcomes of the IDP and RB methods for the highway and FUDS driving cycles. The IDP ensures a better hydrogen fuel economy than the RB in both cycles. Concerning costs and hydrogen consumption levels, it is noticed that those are the highest using the RB method. The latter does not foresee the demand power profile and thus performs a per step optimization which blinds it from locating the sub-optimal allocation range.

The savings in cost and hydrogen consumption levels for the highway cycle when IDP is used as compared to RB are around 0.4% and 0.06% respectively. The savings are higher for the FUDS cycle because the IDP tends to utilize the battery more frequently by charging and discharging it. The savings in hydrogen consumption using the FUDS driving cycle is approximated at 0.3% in favor of the IDP method. The savings in cost are 0.7% in favor of the IDP method. FUDS cycle is rich with regenerative braking energy which makes the

Table 4.6: IDP/RB Comparative Results.

	IDP	RB
<i>Highway Driving Cycle</i>		
The Cost of Operation (\$)	2.80	2.81
Electric Energy Supplied by FC (kWh)	3.9	3.91
Electric Energy Supplied by BT (kWh)	0.6	0.5
Total amount of H2 fuel consumption(g)	181.6	181.7
Fuel Cell Stress Factor	17.3	17.6
Battery Stress Factor	11.4	11.6
Off-line Runtime (seconds)	8	2
<i>FUDS Driving Cycle</i>		
The Cost of Operation (\$)	1.39	1.4
Electric Energy Supplied by FC (kWh)	1.935	1.936
Electric Energy Supplied by BT (kWh)	1.097	0.92
Total amount of H2 fuel consumption(g)	84.39	84.62
Fuel Cell Stress Factor	11.3	11.5
Battery Stress Factor	12.2	12.4
Off-line Runtime (seconds)	13	2

IDP optimally use the battery so as to save hydrogen consumption.

In the highway and FUDS cycles, it is noticed that the convergence speed of the RB method outweighs that of the IDP. This convergence speed is the time it takes Matlab to perform the off-line runs and thus calculate the power allocation matrix that is fed to the Simulink model. This time is of value because it is the time the driver needs to spend in his vehicle waiting for the sub-optimal power allocation to be calculated and delivered to the vehicle controller before he/she can start the trip. As commonly known that each power allocation algorithm has a certain superiority over the other. While the IDP one ensures lower hydrogen consumption rates, the RB method guarantees faster convergence speed. Therefore, the answer for the question of which is better remains in the kind of application. If the whole cycle is known, then the driver would need a few more seconds to optimize the power allocation matrix and thus find the sub-optimal solution. The driver can do that before starting the trip. The few extra seconds needed to wait are worth the savings in the hydrogen fuel. If the cycle is not known and looped dynamic programming is used then for sure IDP is superior over RB. The windows in the looping IDP are small and therefore the convergence rate of the IDP is much faster and comparable to the convergence rate of the RB. Consequently, lower hydrogen fuel consumption levels are highlighted in the IDP.

Another parameters worth mentioning are the stresses that are added

on the sources using the IDP and RB methods. The stresses on the battery and fuel cell are approximated based on the haar wavelet transform. For the highway cycle, the RB method tends to relax the battery thus using it at the beginning of the cycle in a charge depleting mode. The fuel cell supplies most of the load all the time. So the frequency of shifting power supply in the fuel cell is higher using the RB method. For the FUDS cycle, the fuel cell has higher stresses using the RB method because the algorithm does not make use of the battery intelligently so it tends to switch the fuel cell between high and low frequency ranges. The RB cycle adds 2% more stresses on the FC and battery in the highway and FUDS cycles as compared to the IDP method.

For the highway and FUDS cycles, the electric energy supplied by the fuel cell is higher using RB method than using IDP method. During the highway cycle the FC is supplying 3.9 kWh using the IDP method and 3.91 kWh using the RB method. This is approximately a 0.3% difference in favor to the IDP method. On the other hand, the IDP method utilized the battery more than the RB method. During the highway cycle, the battery supplied 0.6 kWh of energy using the IDP method and 0.5 kWh of energy using the RB method. During the FUDS cycle, the battery supplied 1.097 kWh of energy using the IDP method and 0.92 kWh of energy using the RB method. The IDP method tends to utilize the battery more than the RB method in an attempt to lower down the hydrogen fuel consumption.

Figure 4.8a,b shows the behavior of the power supplied by the fuel cell and battery using the IDP and RB methods tested on the highway driving cycle. In figure 4.8a, the battery profile based on the IDP and RB methods is traced in the blue and red curves respectively. The battery is discharged a bit more using the IDP method during the window ranging from 610 till 650 seconds. This result is expected based on the numerical outcomes that show higher energy supply of the battery using the IDP method.

In figure 4.8b, the blue curve shows the fuel cell power profile based on the IDP method, while the red curve shows the fuel cell power profile based on the RB algorithm. The profiles almost match one another, however it is noticed that the IDP method tends to use the fuel cell at lower power levels. This is evident also in the numerical results where the energy supplied by the fuel cell using the IDP method is lower than that of the RB method.

Similar plots for power source curves based on IDP and RB method are superimposed for the FUDS cycle. Figure 4.8c shows the battery profiles for the IDP and RB strategies in blue and red curves respectively based on the FUDS cycle. Figure 4.8d shows the behavior of fuel cell power levels in the blue and red curves corresponding to the IDP and RB strategies respectively.

The profiles are similar in analysis to the highway ones. The battery is used slightly more in the IDP method in an attempt to lower hydrogen consumption level. This is shown in figure 4.8c. The fuel cell is used more using the RB method as shown in figure 4.8d.

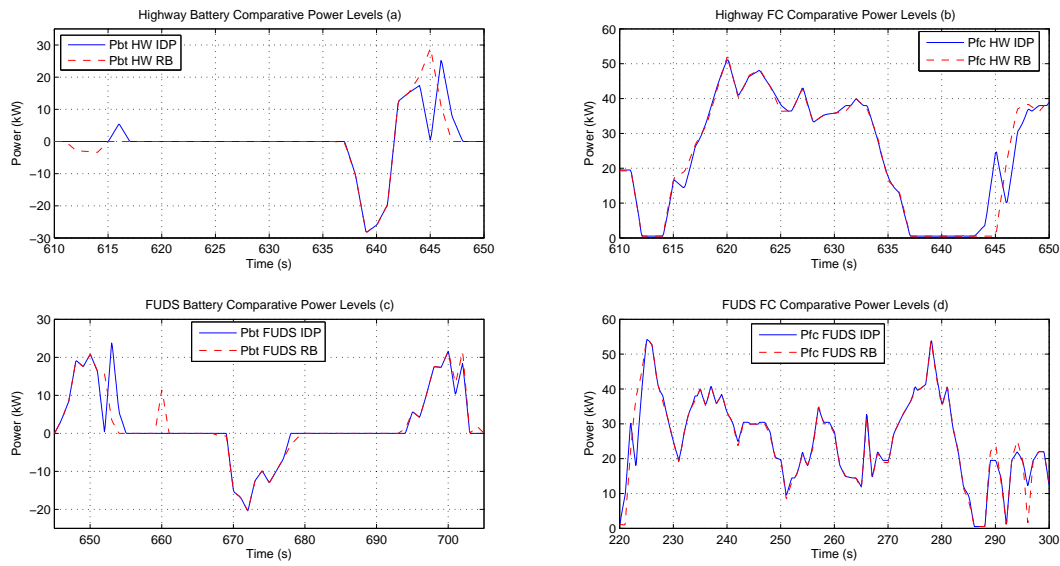


Figure 4.8: IDP RB Comparative Results.

This conforms with the nature of the RB solution which tends to have a local control on the cycle. Unlike the IDP method which employ the apriori knowledge of the cycle to set the power allocation between sources so as to reach a sub-optimal solution.

Chapter 5

Improved Dynamic Programming Algorithm for Analogous, Unknown and Special Event Driving Cycle

The objective behind this chapter is to formulate a methodology to approximate and tackle unknown driving cycles. Three different problems are considered. First, if the cycle is not known but can be compared to existing driving cycles. Second, the methodology to handle special events occurring on the road for certain trips. Finally, using a novel looping methodology where a cycle fore-cast is executed. The improved dynamic programming algorithm is applied to analogous, unknown and special events driving cycles that are approximated.

5.1 Analogous Driving Cycles

Analogous driving cycles represent a sequence of speeds that are similar to the known driving cycles. They are approximated based on the person's technical expertise of the road trip. In this section, two roads in Beirut, Lebanon are adopted and the speed is approximated according to the technique that will be shortly explained. Then a power profile is generated and the optimal power allocation matrix is derived.

The novel technique approximates an analogous cycle based on the transition probability matrix. Analogous cycles refer to cycles that have similar characteristics to the highway and urban cycles. First, the transition probability matrix for the known driving cycles is derived. This square matrix is based on the speed profile. The entries in the matrix represent the one step transition probability that the vehicle is accelerating at a certain speed during time $(t+1)$ given that it was cruising at a certain speed at time (t) . Then, the pattern of

each known driving cycle is extracted in accordance to the transition probability matrix.

Each pattern is converted to a base unit in-order to be dependent on the characteristics of the analogous driving cycle. The latter is segmented into N divisions where each subdivision is associated with three values. These values are the speed limit, the probability factor relating it to the highway and urban cycles and the traffic coefficient. In other words, in-order to approximate the speed profile of the analogous cycle, the cycle is segmented. Each segment holds values that define its characteristics.

After the derivation of the speed profile, the IDP is simulated in-order to get the optimum power allocation for the analogous cycle trip. The latter is tested under the Simulink environment to calculate the required parameters and analyze the results.

5.1.1 Stochastic Approximation of a Driving Cycle

Stochastic approximation of a driving cycle is used to solve some of the issues of previous knowledge of the driving cycle [22]. The optimization is performed using a transition probability matrix for known power demands. It is characterized by a transitional probability matrix indexed by the current vehicle speed. This matrix maps the current values into the future required power value.

The transition probability matrix is derived by using standard driving cycles. These cycles range from highway, urban and European cycles. They carry the speed profile information for a certain period of time. The speed vectors are v_h , v_u , and v_e for the highway, urban and European driving cycles respectively. However, each has a different size. For this reason, nearest neighbor quantization algorithm is used to map the observed speed values of the driving cycle into the quantized values [69]. The transition probability (TranM) is then estimated by dividing the number of occurrences of a specific transition from a certain speed to another given the total number of speed incidents. The length of TranM depends on the chosen speed sample. For M speed samples, TranM will be an MxM transition matrix. Weights are assigned to the transition matrix probability function to emulate the respective driving cycle conditions as shown in equation 5.1.

$$V = [w_h v_h \quad w_u v_u \quad w_e v_e] \quad (5.1)$$

The weights are w_h , w_u , and w_e for the highway, urban and European driving cycles respectively. The weights symbolize the utilization of a cycle more than the other. For instance, if weights are added to the highway cycle, it implies that the current cycle is more similar to a highway one rather than an urban one.

The transition probability matrix is a right stochastic matrix and thus singular, since all the elements are non-negative and the sum of each row is one. Moreover, the state space of operation is finite in time. For this reason, a

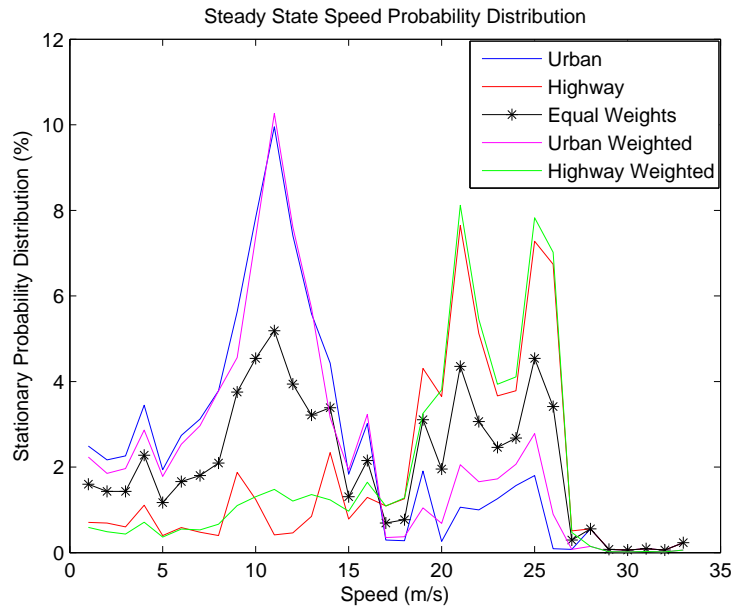


Figure 5.1: Steady State Speed Probability Distribution.

stationary markov chain distribution vector can be approximated for each desired set of weights. This vector is derived by using linear algebra to solve the set of linear equations defined by the TranM and a $1 \times M$ unity vector.

Figure 5.1, shows the vehicle speed versus the stationary probability distribution for five weighting scenarios. The considered scenarios are the urban cycle, the highway cycle, a weighted urban cycle, a weighted highway cycle and an equally weighted cycle. It is noticed that the equally weighted stationary distribution exhibits high and low speed values with relatively high probability distributions. For instance, local high probability peaks occur at 12, 22 and 26 m/sec. While the urban and weighted urban profiles have local high probability peaks only at 12 m/sec. Highway and weighted highway profiles exhibit 22 and 26 m/sec as their local high peaks. This difference provides a surf knowhow of the trend that the cycles follow. For instance, for urban cycles at least 50% of the cycle is spent within a low range of speed extending from 8 till 14 m/sec. While for highway cycles, more than 60% of the cycle takes place at a high speed limit between 18 and 26 m/sec. These bounds are now considered as reference points when deriving an analogous cycle speed profile. When the cycle is weighted then it will tend to spend more time in this speed range.

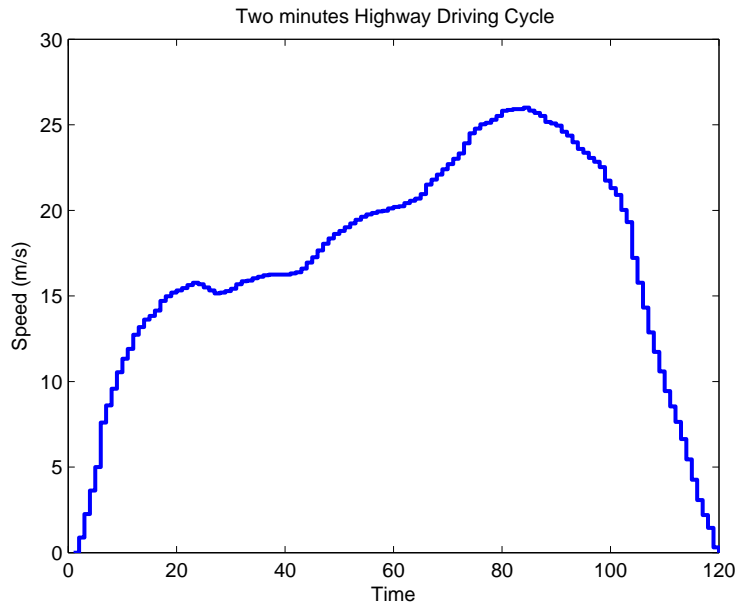


Figure 5.2: Two Minutes Highway Speed Profile.

5.2 Two-minutes Cycle derivation

Using the analysis from the stationary probability distribution, a two minutes range sub-driving cycle mimicking the highway and urban cycles is derived. The two new sub-cycles stay in the previously specified ranges for approximately 60 % of the cycle duration. Figure 5.2 and figure 5.3 show the speed and power profiles of the two minutes highway cycle. It is noticed that the cycle stays in the range of speed from 18 till 26 m/s for approximately 60% of the time. Similarly, figures 5.4 and 5.5 show the speed and power profiles for a two minutes urban cycle where the cycle stays for at least 60% of the time within a speed range of 8 till 14 m/s.

5.2.1 Analogous Cycle Derivation Procedure

To apply this method, a certain range of an unknown cycle is selected. This analogous driving cycle is segmented into N divisions with different or equal durations. Each segment is then divided into samples of two minutes each. Then, the speed profile of the sample is the result of a three component multiplication as shown in equation 5.2. The first component is the traffic coefficient (ρ_{Tr}) which depends on the time of the day. Urban cycles are characterized with congested roads so they exhibit low speeds and fast dynamics. However, each cycle should depend on the amount of traffic it faces. NEDC for example, derives the speed

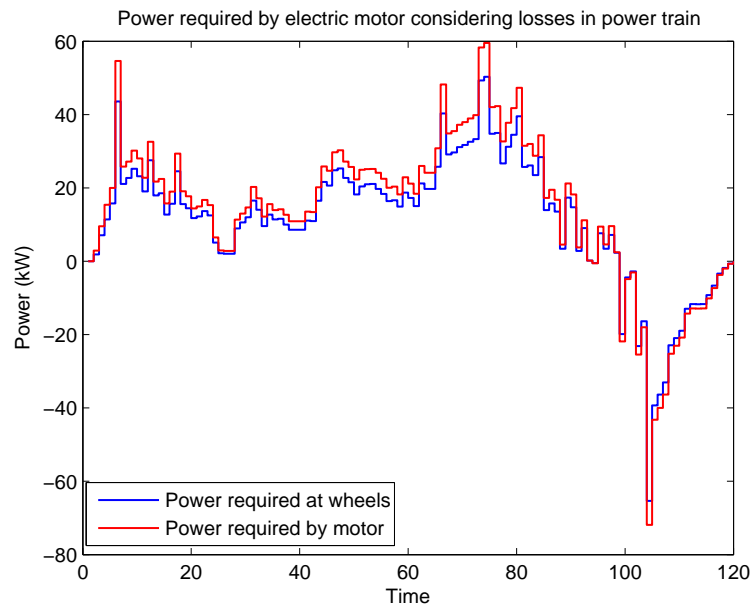


Figure 5.3: Two Minutes Highway Power Profile.

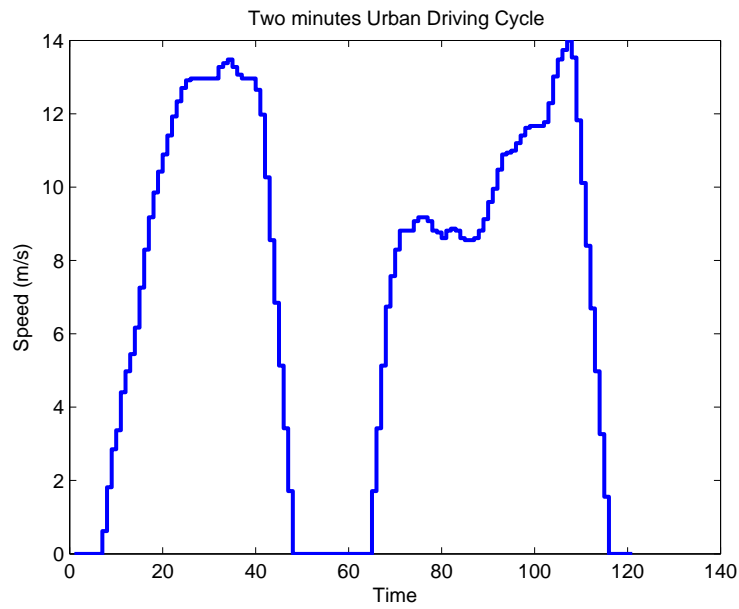


Figure 5.4: Two Minutes Urban Speed Profile.

profiles of the cycle based on the traffic congestion on the European roads. In Beirut, the traffic congestion depends on the time of the day. For instance, at

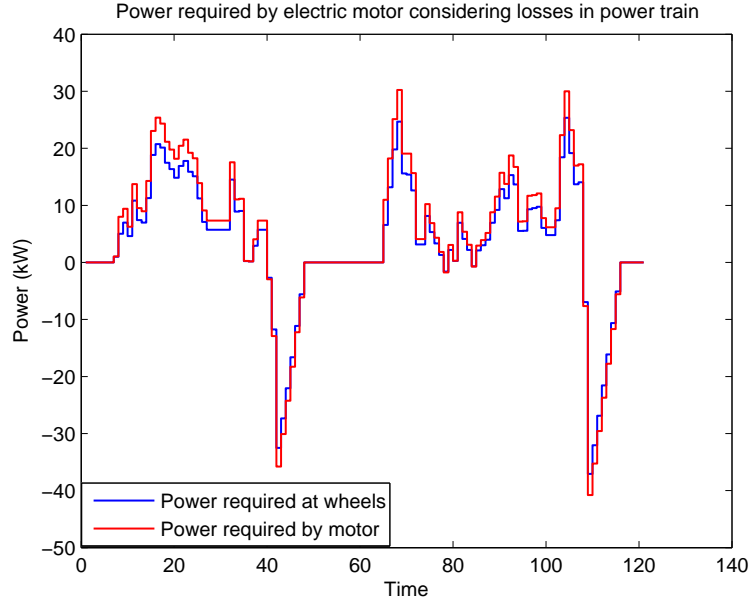


Figure 5.5: Two Minutes Urban Power Profile.

8:00 am the roads in Beirut are usually highly congested, however at night the congestion drops down. Therefore, a coefficient of congestion is added to the derivation of the speed profile. It is set as low, medium or high with coefficients set according to table 5.1. The second component is the speed limit (Sp_{lim}) that is usually set by the country's municipality corresponding to the road. Finally, the third component is the normalized speed of the two minute cycle. Thus, if the sample is evaluated as close to the highway cycle then the two-minutes highway cycle profile (v_{hs}) is normalized with respect to its maximum value (v_{hs-max}). Similarly, if it is close to the urban cycle then the speed profile (v_{us}) is divided by the maximum value (v_{us-max}).

$$\begin{cases} \text{Highway Analogy:} & V_{H-ana} = \rho_{Tr} Sp_{lim} \frac{v_{hs}}{v_{hs-max}} \\ \text{Urban Analogy:} & V_{U-ana} = \rho_{Tr} Sp_{lim} \frac{v_{us}}{v_{us-max}} \end{cases} \quad (5.2)$$

5.3 Analogous Cycle Derivation Example

In order to test the analogous cycle derivation, two roads are considered. All the roads are in Beirut Lebanon and the time of testing occurs at around 2:00 p.m. The road data and the segmentation characteristics are derived based on personal expertise and knowledge of the driven road. These roads are of different

Table 5.1: Traffic Coefficients.

Traffic Value	Highway Analogy	Urban Analogy
Low	1	1.5
Medium	0.8	1
High	0.5	0.8

Table 5.2: 5 Minutes Road Data Characteristics.

Segment	Analogy Cycle	ρ_{Tr}	Time (min)	$S_{p_{lim}}$ (km/hr)
1 till 2	Urban	high	1.5	60
2 till 3	Highway	low	0.25	60
3 till 4	Highway	low	0.5	60
4 till 5	Highway	low	0.5	60
5 till 6	Urban	high	1.5	60
6 till 7	Highway	low	0.5	60
7 till 8	Highway	low	0.25	60

time duration, five minute road data is shown in table 5.2 and figure 5.6 and the 19 minutes road data are shown in table 5.3 and figure 5.7.

5.3.1 Speed Curves and corresponding Load Profiles

The speed curves and corresponding torque characteristics of the 5 and 19 minutes cycles are shown in figures 5.10 and 5.13. For the five minutes cycle, the vehicle speed has a mismatch at around 170 seconds due to the sudden shift in its speed. This is due to the fact that the vehicle dynamics need time to adapt to such a

Table 5.3: 19 Minutes Road Data Characteristics.

Segment	Analogy Cycle	ρ_{Tr}	Time (min)	$S_{p_{lim}}$ (km/hr)
1 till 2	Urban	high	3	60
2 till 3	Urban	high	3	100
3 till 4	Highway	low	4	100
4 till 5	Highway	low	1.5	100
5 till 6	Highway	low	1.5	100
6 till 7	Highway	high	3	100
7 till 8	Urban	high	3	60

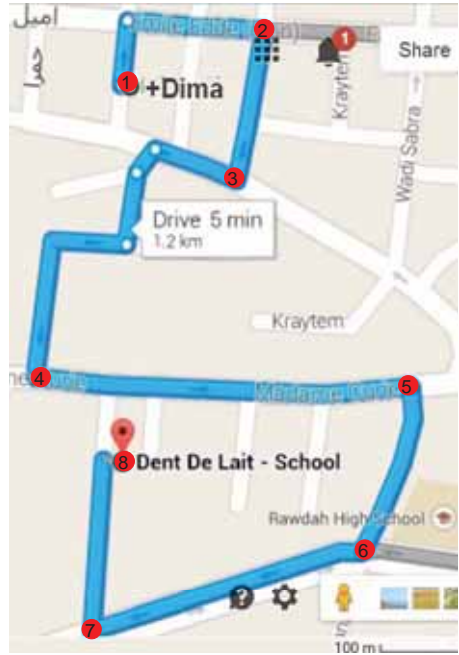


Figure 5.6: 5 Minutes Road Profile.

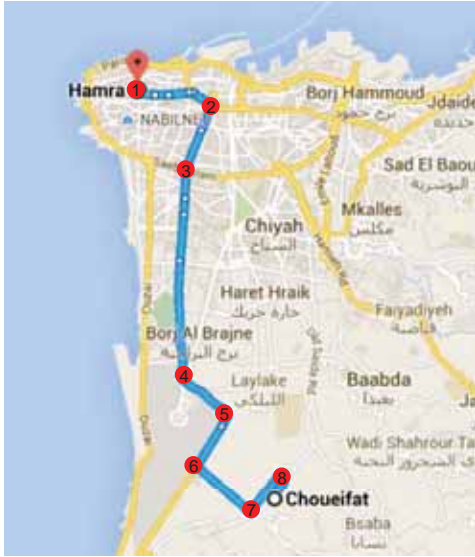


Figure 5.7: 19 Minutes Road Profile.

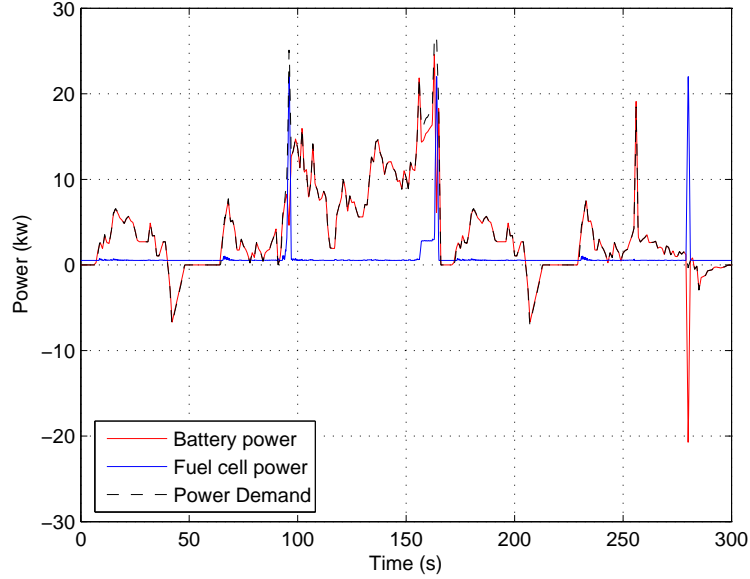


Figure 5.8: 5 Minutes Power Allocation Profile.

change. For the 19 min driving cycle, the speed curve was followed smoothly with no sudden shifts or controller's errors.

The power allocations for the two driving cycles using the IDP algorithm explained in chapter 3 are indicated in figures 5.8 and 5.11. It is noticed for the 5 min driving cycle that the battery is incorporated more since it is a small cycle and it can recuperate at around 40 and 270 seconds.

For the 19 min driving cycle, the battery plays a more important role due to its frequent charging. It is limited to -40kW as a lower limit. A zoomed in episode for the 19 minutes cycle is shown in figure 5.11. The battery aids the FC during the high power demands in-order to lower hydrogen consumption levels and relieve stresses on the FC.

The battery SOC comparison between on-line and off-line results for the driving cycles are shown in figures 5.9 and 5.12. For the five minute cycle the battery SOC is used till about 60%. While for the 19 minute cycle, it is drained till 40%.

5.4 Driving Cycles with Special events

Special and unpredictable events might occur during a driving cycle. These can range from a sudden vehicle accident to a police patrol halt signal. The improved dynamic programming algorithm caters for these special event by using an adaptive looping methodology. This methodology is based on a forecast that

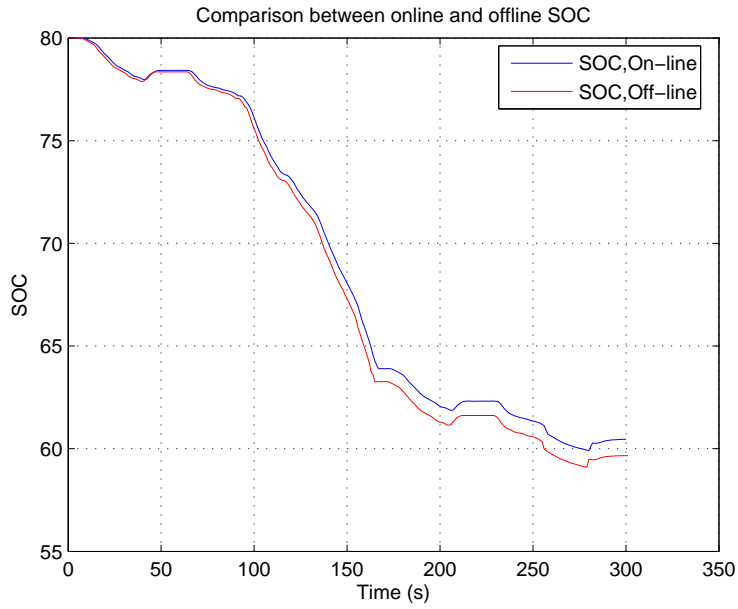


Figure 5.9: 5 Minutes SOC Profile.

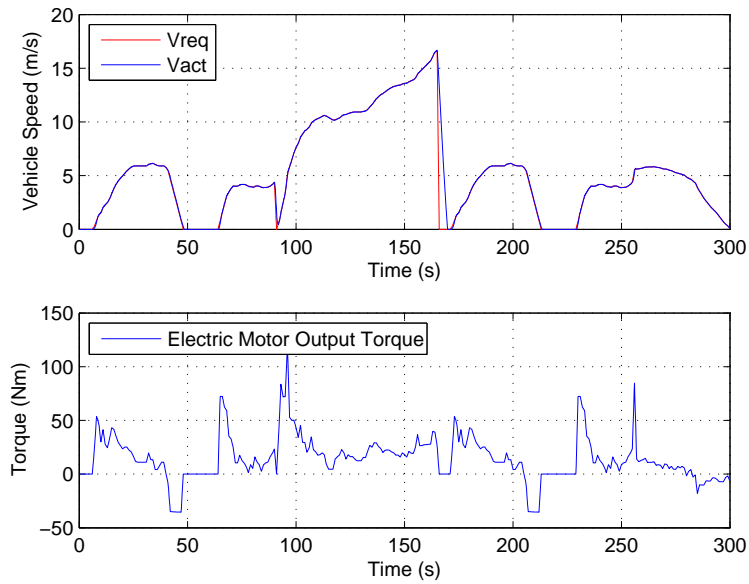


Figure 5.10: 5 Minutes Speed-Torque Profile.

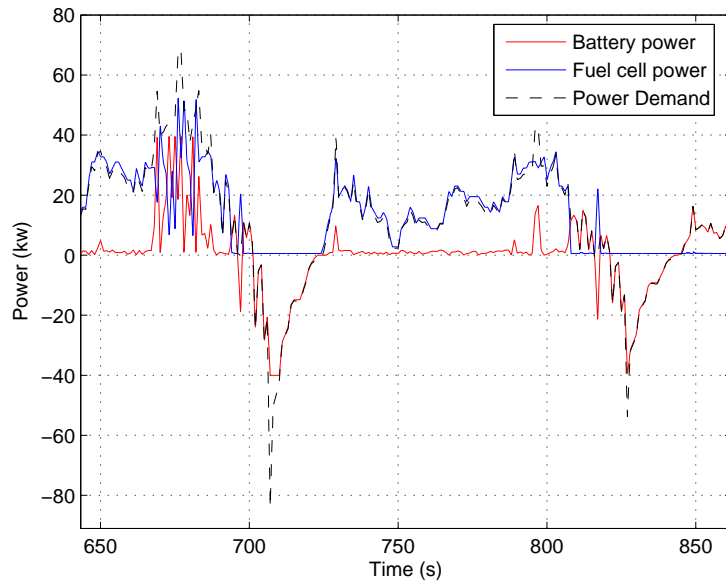


Figure 5.11: Episode - 19 Minutes Power Allocation Profile.

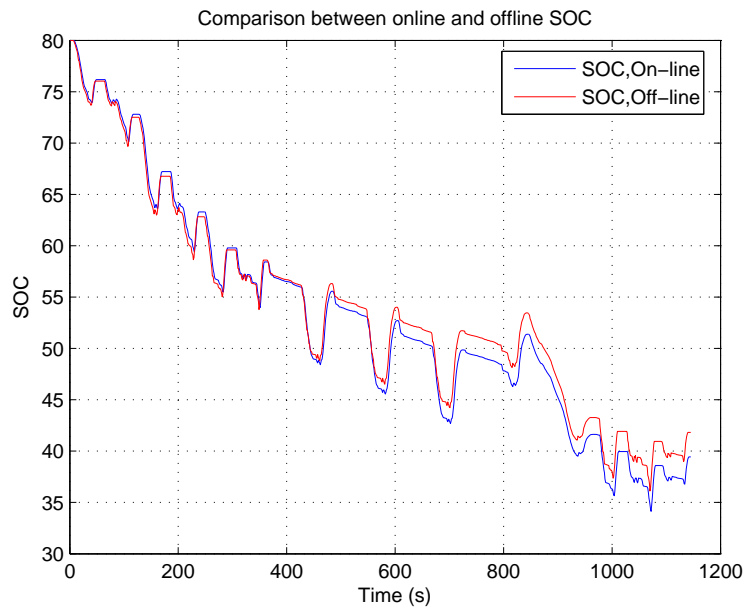


Figure 5.12: 19 Minutes SOC Profile.

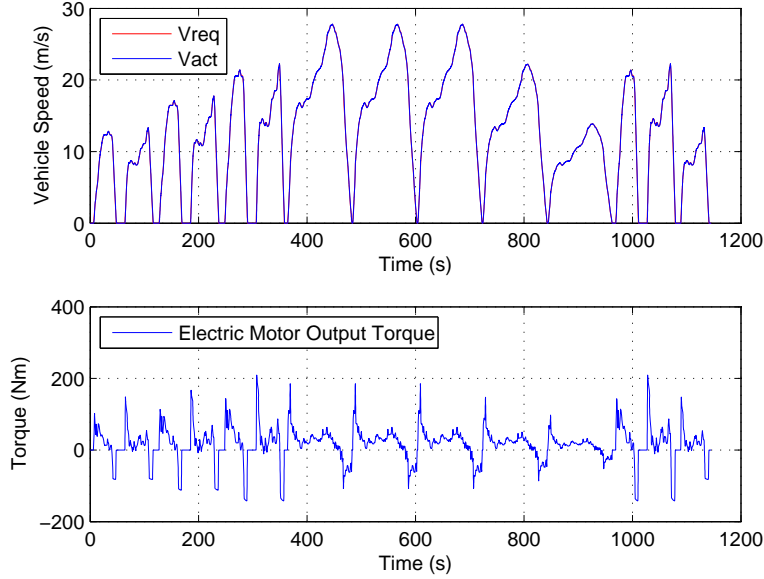


Figure 5.13: 19 Minutes Speed-Torque Profile.

is recognized at least a minute before the occurrence of the event. Then the speed profile is updated based on intuitive approximation. IDP algorithm is simulated to yield the updated power allocation values. Therefore, when the vehicle approaches the episode the system would have already updated its entries.

5.5 Special Events Formulation

During a highway driving cycle and at about 300 seconds after the beginning of the trip, the traffic control station signals a vehicle collision occurring when the vehicle reaches 500 seconds in time. For this reason, the vehicle needs to do a stop at around 500 seconds by gradually decreasing the speed until it reaches its idle state. Then accelerating again to finish the required distance. This deceleration results in regenerative braking energy which will charge the battery. The IDP algorithm uses this extra charge to lower the hydrogen consumption when the vehicle accelerates again. By not incorporating this looping methodology, the vehicle will not optimally benefit from this extra energy charging the battery. This is shown in figure 5.14 where the vehicle decreases its speed by about 500 seconds to reach a stop at around 550 seconds. It stays in idle mode for about 10 seconds and then accelerates back again and continues the path that occurred at the episode start time. This is the reason for the time shift of the two curves. The power allocation curve for the episode occurrence is shown in figure 5.15. The behavior of the battery SOC during the episode where the battery charges



Figure 5.14: Wheel Speed Before and After the Special Event.

Table 5.4: After 500 seconds Cost and Hydrogen Consumption Comparison.

State	Value
Cost without Episode Occurrence (\$)	1.45
Cost with Episode Occurrence (\$)	1.59
Hydrogen Consumption without Episode Occurrence (g)	68.9
Hydrogen Consumption with Episode Occurrence (g)	75.3

approximately to full charge due of the vehicle deceleration is shown in figure 5.15. The behavior of the power with and without the episode occurring is shown in figure 5.17. Figure 5.18, reveals the power levels during the episode where the battery charges the power and can discharge it at later stages. Table 5.4 illustrates the comparative results of cost and hydrogen consumption with and without the episode occurrence. The slight increase highlights the importance of knowing the episode occurrence beforehand.

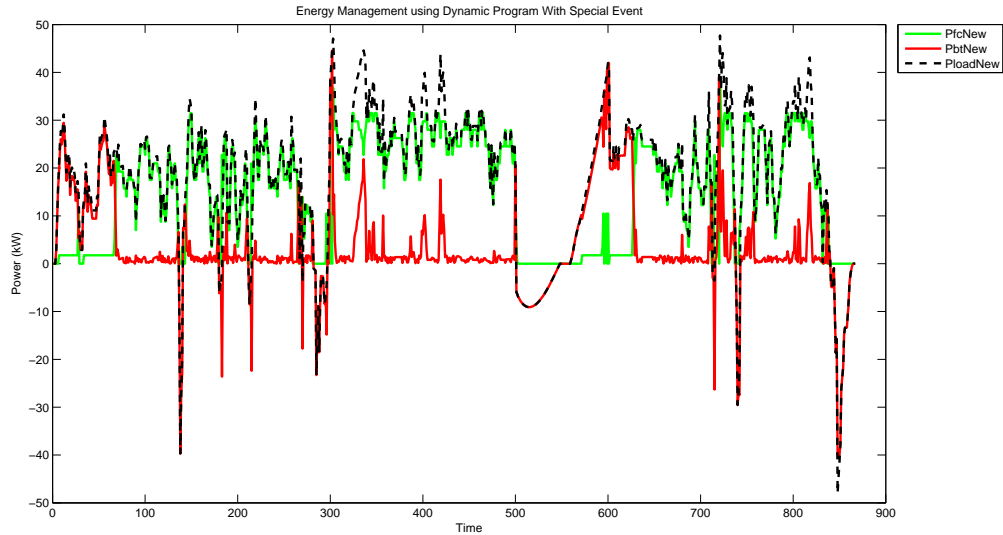


Figure 5.15: The optimal power allocation for the Episode Occurrence.

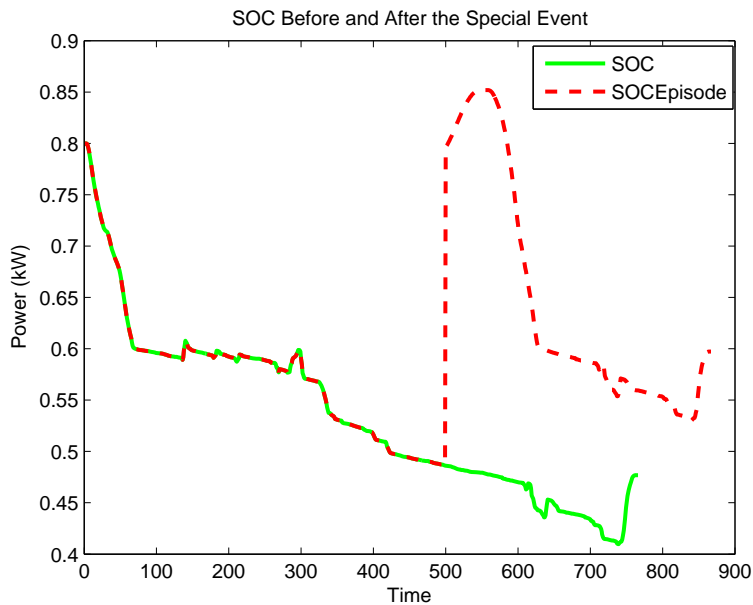


Figure 5.16: The Battery SOC for the Episode Occurrence.

5.6 Unknown Driving Cycles Looping Mechanism

The looping mechanism is a novel technique to provide the optimum power allocation between the vehicle sources while the vehicle accelerates. The driving cycle

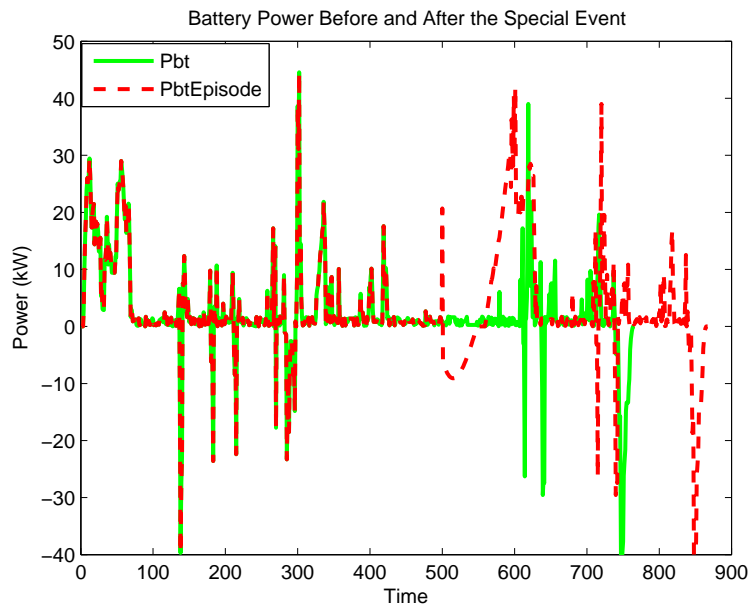


Figure 5.17: The Power Behavior with and without the Episode Occurrence.

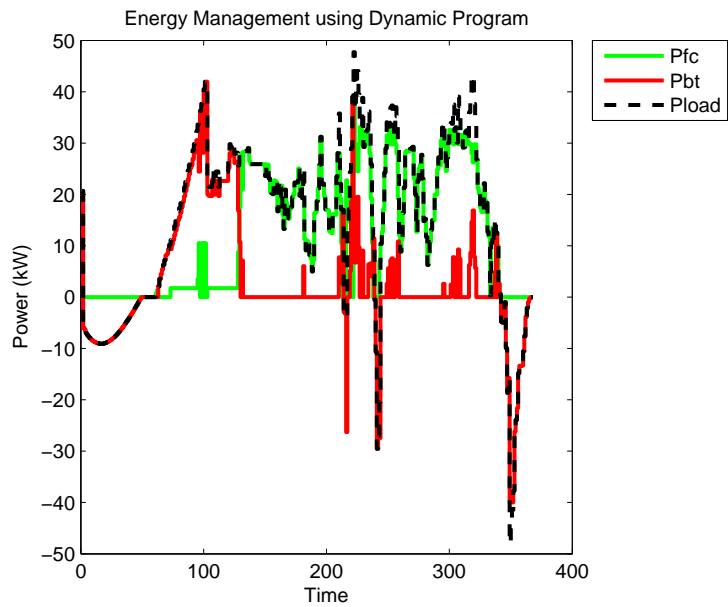


Figure 5.18: The Power Behavior During the Episode Occurrence.

in this case is not known, however the time length of the cycle is speculated. The cycle can be approximated from environmental, traffic or road conditions. The

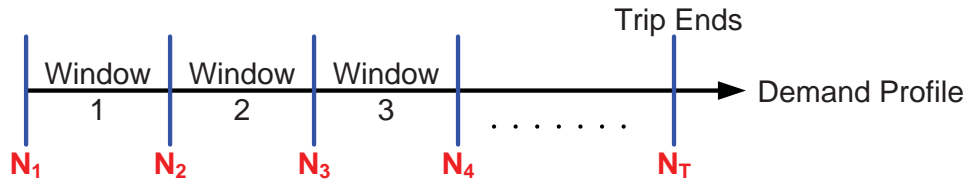


Figure 5.19: Looping Method.

technique opens the window to apply the IDP in smaller chunks targeting real time optimization. In essence, this method can help applying an optimization algorithm during real time optimization for a certain small fore-casted driving cycle.

Figure 5.19 shows a simple sketch to clarify the procedure for implementing the looping strategy. The horizontal arrow in the figure represents the load demand which is unknown in this case. However, it can be assumed that this demand is for a certain period of time. Then, the demand is split into chunks depending on the selected sample time. For example, if a 50 seconds sample time is selected, then the windows that are indicated in figure 5.19 each have a duration of 50 seconds. The nodes ($N_1, N_2 \dots N_T$) fragment the windows. When the trip is identified and before the vehicle starts accelerating, the power demand during window 1 is approximated and fed to the off-line IDP algorithm to obtain the optimal power allocation matrix. At N_1 the first optimal power allocation matrix which corresponds to window 1 is fed to the system and so the vehicle can start to accelerate accordingly. While the vehicle is accelerating through window 1, the power profile of window 2 is estimated based on traffic and road conditions. During the motion in window 1, the off-line IDP algorithm provides another optimal power allocation for the system sources and feeds it to the system at node 2. When the vehicle reaches node 2, it can accelerate based on the provided optimal matrix derived from the optimal IDP. This is repeated until the trip ends. For each window the vehicle is in, the power demand of the next window is approximated and then fed to the off-line IDP optimization tool. The result from the latter is fed to the initial node of the next window. When the vehicle ends the current window and reaches the node of the next window, it will be accelerating using the optimal allocation matrix fed at that node.

To test the feasibility of this method, a 200 seconds sample from the highway driving cycle is considered. The method is tested against a known driving cycle to validate the results. The known cycle is selected and then treated as if it is unknown. It is split into several windows and the program assumes that the cycle is fore-casted during each window. The looping algorithm is validated when compared against the whole selected cycle before splitting it.

The most important thing to consider when dealing with the looping IDP

algorithm is the battery SOC at the end of each window. Each window considers a small sample of the load demand. The proposed IDP algorithm tends to discharge the battery in-order to decrease the hydrogen fuel usage and thus lowers the system cost. This is important when considering the whole driving cycle, because the IDP can locate the sub-optimal positions of the battery discharge periods based on the location of the battery charges using regenerative braking. This is not the case when considering only small windows of the cycle when it is not known. For this reason, the amount of battery energy used for discharge should be identified prior to the cycle. This guarantees that the battery can continue to aid the fuel cell throughout the trip. Moreover, the battery can benefit from the regenerative braking during the unknown trip. To clarify this with an example, a 200 second of the highway driving cycle is considered. This is sampled into 50 seconds intervals and results in four windows for the power demand. The looped IDP algorithm is executed for each interval and the IDP algorithm is simulated for the 200 second cycle. The comparison between the two results determines the efficiency and efficacy of the model.

First, the 200 seconds of the highway driving cycle is split into 4 windows and 5 corresponding nodes. Each window considered the power demand for a duration of 50 seconds. The initial battery SOC considered is 0.8 and the amount of drop in this SOC during each window is 0.1. Therefore, at node N_1 and before the cycle starts, the load demand through window 1 is fed to the IDP algorithm to get the optimal matrix of power allocation. The vehicle starts accelerating based on this matrix which contains the split of power between the fuel cell and battery. During window 1, as if the cycle is unknown, the control system of the vehicle receives the necessary signals to estimate the next driving cycle of window 2. The approximated driving cycle is fed to the IDP algorithm. Now the initial SOC that was used during window 1 is changed to the final approximated SOC at the end of window 1. Thus at a rate of 0.1 decrease in SOC for each window, the approximate final SOC for window 1 and the initial SOC for window 2 is 0.7. The derived optimal allocation matrix of the power demand of window 2 is fed to node 2 before the cycle of window 2 starts. The vehicle continues its acceleration through window 2 following the updates received at node 2. Similarly the case for window 3 and window 4. The final SOC estimated at node 4 is 0.4.

The IDP algorithm is simulated simultaneously for the 200 seconds driving cycle. The initial battery SOC is considered to be 0.8 and the final battery SOC is approximated at 0.4. Comparison is carried out between the looping technique performed in windows of 50 seconds on the 200 seconds highway cycle, to the whole 200 seconds of the highway. The SOC initial and final limits for both cycles are the same. The significance of this comparison is in monitoring the behavior of the system sources during the windowed cycle versus the normal cycle. Definitely, it is not expected to have the same source power profiles but what is noticed is that the two runs had the same hydrogen consumption levels. Therefore, the fuel cell profiles are different but they have the same total energy

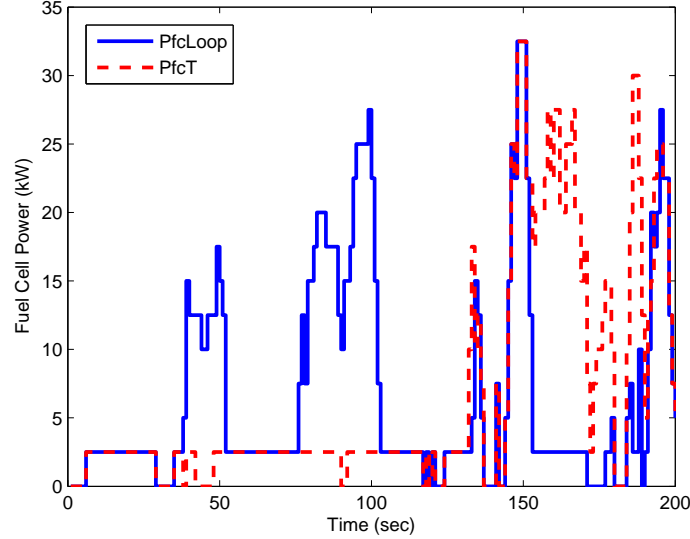


Figure 5.20: Fuel Cell Power Profile Comparison.

over the duration of both cycles. Figure 5.20 shows the fuel cell power profile where the blue curve is derived by the off-line simulation of the IDP algorithm in windows of 50 second duration. The red curve corresponds to the simulation of the IDP algorithm for the 200 seconds highway cycle. Although the two curves do not overlap, they have similar layouts at different intervals of time. The two power peaks shown in the blue curves during 40 to 120 seconds is comparable to the one shown by the red curve during 160 to 190 seconds. The total energy calculated under both of the fuel cell curves and thus the hydrogen consumption levels are the same. The SOC profiles for the two methods are shown in figure 5.21. The blue curve which corresponds to the looping method, discharges the battery in steps of 0.1 as specified by the program. If these steps were not identified, then the battery would have discharged most of its energy during the first window and thus exhaust the fuel cell and increase the hydrogen consumption levels for later windows. The two curves have the same initial and final SOC levels. The battery during the 200 second cycle is used more in the beginning while during the looping methodology it took more time to discharge it.

This comparison validates the efficiency of the looping methodology in terms of consuming the same amount of hydrogen energy. The choice of the permissible SOC level during each window is also vital for the simulations. The IDP algorithm has limited number of states at each level and thus does not consider all possible candidates. For this reason, if the selection of SOC limits is narrow, the program might go into infeasible states.

The whole highway driving cycle is tested under the looping methodology.

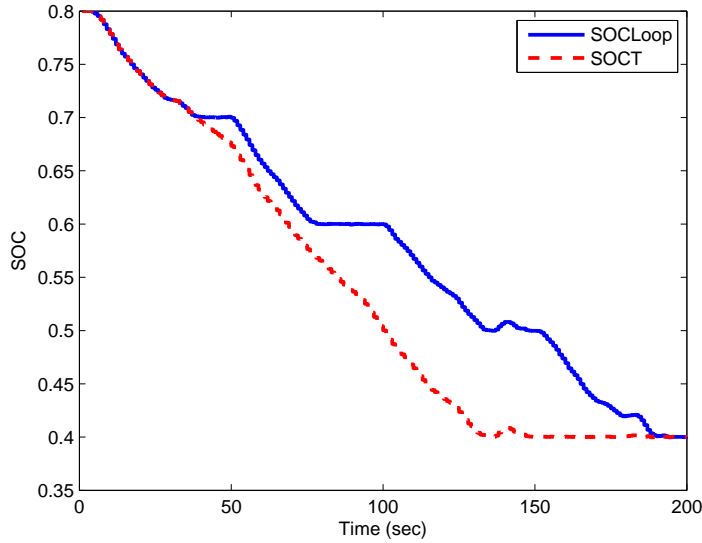


Figure 5.21: SOC Profile Comparison.

It is split into 13 windows with an approximate duration of one minute. The battery is considered to be fully charged with a SOC of 0.95. This makes use of battery energy by placing it in a charge depleting mode and therefore decrease hydrogen consumption levels. Figure 5.22, shows the fuel cell profile and the SOC profile while using the looping methodology. Another curve is overlaid on the figure which corresponds to the profiles without considering the looping methodology. It is noticed from both curves that the profiles can not be overlaid. However, by measuring the energy supplied under the two fuel cell power curves, it is noticed that the difference is less than 2 percent. Therefore, the looping methodology guarantees a minimum hydrogen consumption similar to the known cycles.

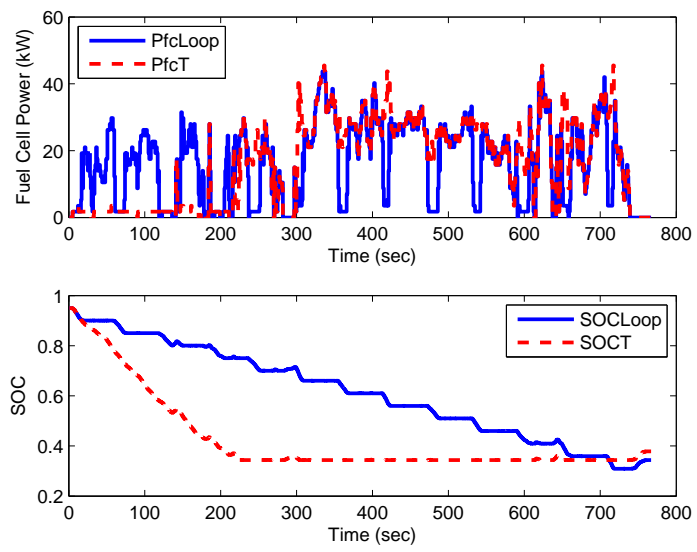


Figure 5.22: HW Profile Comparison.

Chapter 6

Real Time Testing

The validity of the power management strategy proposed is experimentally tested using a low cost hardware in the loop model. It emulates the power flow between the sources of the FCHV power train. The test bench is used to compare the effect of hydrogen consumption using the IDP and RB algorithms while cruising the highway or the urban driving cycles. The battery is the main driving source in the system. It gets charged from the fuel cell and from the negative load during regenerative braking.

Real time testing is a process to test the software algorithms in hardware. It would have been ideal to use an actual sprinter to test the IDP algorithm, however this was not available. For this reason, the stationary test bench is built in the University of Applied Sciences labs in an attempt to launch the testings. The system embeds a fuel cell, a battery, a power supply and an inverter. Labview model is used to provide an interface between the user and the system.

The goal behind testing in real time is to compare the results that are achieved during the off-line simulations and the ones resulting from the real time model. During the off-line simulations, the outcome is the power allocation matrix holding the values of the power from the fuel cell and battery for each sample of time for a given driving cycle. This matrix is obtained using the IDP algorithm which is proposed in this thesis or the state machine control based algorithm which is used for comparison. The off-line simulations also result in the hydrogen consumption levels for the IDP algorithm and the state machine rule based algorithm.

For each driving cycle, two matrices are obtained from the off-line simulations and two corresponding hydrogen consumption levels. The first one is acquired using the improved dynamic programming algorithm. It holds the sub-optimal power allocation between the fuel cell and the battery. It also embeds the SOC profile for the corresponding driving cycle while using the IDP method. The corresponding hydrogen consumption level is calculated and saved for the driving cycle under test. The second matrix holds the power split between the fuel cell and battery along with the SOC profile while undergoing an energy man-

agement system based on the state machine rule based algorithm. The hydrogen consumption level for the corresponding algorithm and driving cycle is stored.

These off-line matrices are fed to the real time system one at a time. For example, for the highway driving cycle, a certain off-line matrix is obtained along with the hydrogen consumption level. This matrix is fed to the real time system via the Labview interface. Moreover, the corresponding power demand is also fed to the real time system. This power is calculated as explained in previous chapters by taking into account the losses in the electric motor and transmission system. The demanded power is the power at the DC bus before the electric motor and inverter system. The real time system starts running by first turning on the fuel cell and then start feeding the load values. The fuel cell and battery system take the power values from the matrices so as to feed the load accordingly. In the end, the actual hydrogen level obtained from the real time simulation is noted down so as to compare it with the off-line one. This is similarly done to the other cycles and to the matrices based on the state machine rule based algorithm.

6.1 Real Time System Model

To carry out the real time simulations, a test bench model is developed for the FCHV equipped with a fuel cell, battery, inverter and power supply. The components of the model are interfaced using Labview. The difference between this real time system model and the Simulink model explained in the previous chapter lies in the system sizes. The size of the system in the Simulink model emulates the real hybrid sprinter values. For example, the Simulink model embeds a 70kW fuel cell, a 70kW electric motor and a 6.5 Ah battery. On the contrary, the real time system model addressed in this section is composed of small sized sources. It has a 1.2kW fuel cell, a 40Ah battery, a 320W power supply and a 2000W inverter as summarized in table 6.1.

The interface of the system components is build using Labview. In Labview, there is a user interface which is defined as the front pannel. The latter is tied to the development cycle. The front panel for our model is shown in figure 6.1. The layout shows the connection of the fuel cell and DC/DC converter. The output current and the output power of the fuel cell can be monitored through the interface via a potentiometer. Also, the output current and the output power of the DC/DC converter can be tracked. The DC/DC converter is manually designed to fit the application using an Arduino Uno controller. The DC/DC converter is connected to the battery. The latter supplies the electronic DC load and is charged by the fuel cell and the power supply. The electronic load current and power can be monitored from the interface. This load mimics the actual vehicle motoring load which in our case is a positive quantity. The power supply represents the negative load of the system which identifies recuperation. On the left tabs of the front panel, is the interface where the load profile and the power

Table 6.1: FCHV Test Bench Subsystems.

Subsystem	Description
FC System	PEM FC with a rated power of 1.2 kW
Battery System	Lithium ion battery with a nominal voltage 26V of and a capacity of 40Ah
DC/DC Two Way Converter	For the battery discharging and charging currents
Power Supply	Power Rating of 320W
Inverter	DC input power up to 2000W

allocation matrix are identified through spread sheets.

The second panel is for the fuel cell which is shown in figure 6.2. The fuel cell variables are measured, such as the stack temperature, voltage as well as the hydrogen consumption levels. The schematic panel shown in figure 6.3 shows the architecture of connection between the components. The flow of current as well as the nodal voltage can be monitored throughout the runs. The sources panel shown in figure 6.4 shows the power profile of the sources and the load throughout the period of testing. The latter is beneficial for the comparison between this real time testing and the off-line results obtained from the Matlab runs. National instruments also used Labview as an interface for the hardware in the loop simulation of a hybrid electric vehicle [91].

6.2 Fuel Cell System Model

Ballard power systems develop and manufacture PEM fuel cell systems [92]. They have shipped up to 150 MW of such fuel cells up until 2014. In this test bench, a nexa FC stack from Ballard sized to supply a 1.2 kW net output power is employed. The output voltage is a function of the power and ranges from 26 to 43 volts. In cases of failure or under unsafe conditions the FC shuts down immediately. The hydrogen is supplied and monitored by the FC system.

The Nexa FC system shown in figure 6.5, is composed of the hydrogen tank maintained between 0.7-17 bar, a 5V start/stop signal and the FC stack with cooling fan. The FC stack has a membrane electrode assembly structure where the membrane is a catalyst coating membrane with a gas diffusion layer. The air is not compressed in this FC and the natural air existing in the lab environment is used. The connection to a PC is done via a RS 486/232 serial communication bus. The display on the PC include the stack temperature, voltage, current, pressure, leak, consumption and power. All this data can be logged in a text file for processing. The FC stack depends on the temperature, so as the temperature

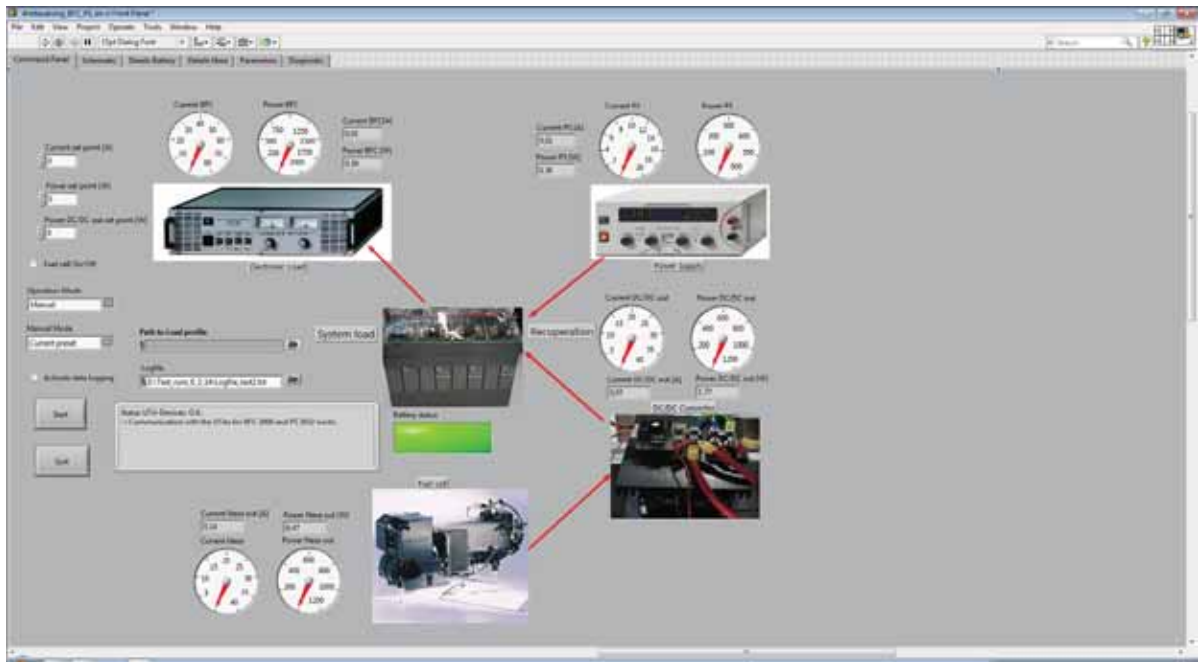


Figure 6.1: Labview Command Panel.

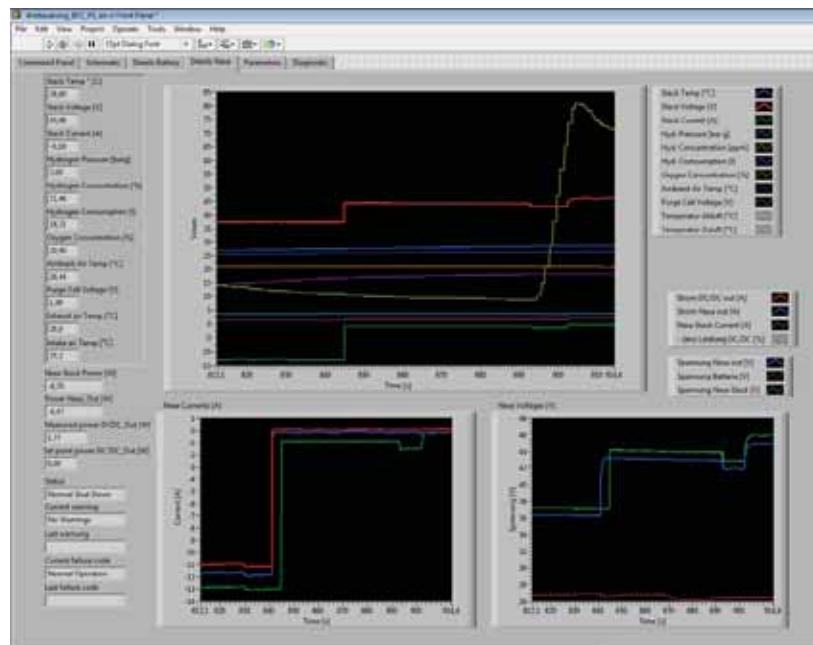


Figure 6.2: Labview Fuel Cell Panel.

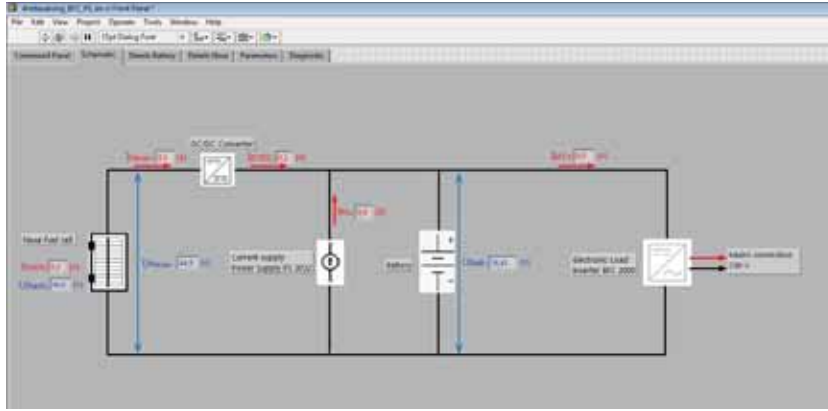


Figure 6.3: Labview Schematic Panel.

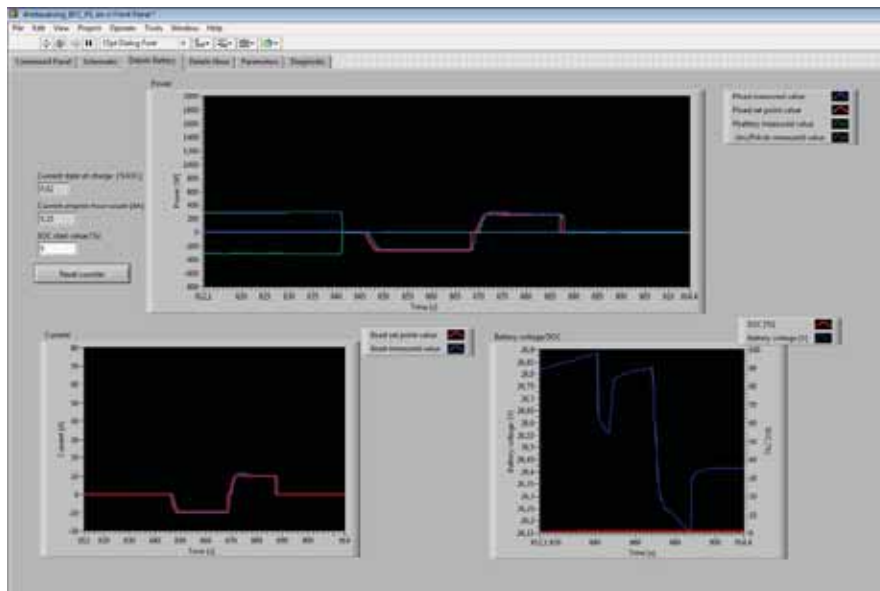


Figure 6.4: Labview Sources Panel.

increases the losses decrease because the reaction runs faster. However, this increase depends on the mechanical strength of the membrane. Usually in the smart car the FC runs at 55 degrees Celcius. The FC characteristics are shown in table 6.2.

6.3 Battery System Model

The battery system is specially manufactured for this application at Hyliontec development facility in Stuttgart [93]. It is a lithium ion phosphate battery with

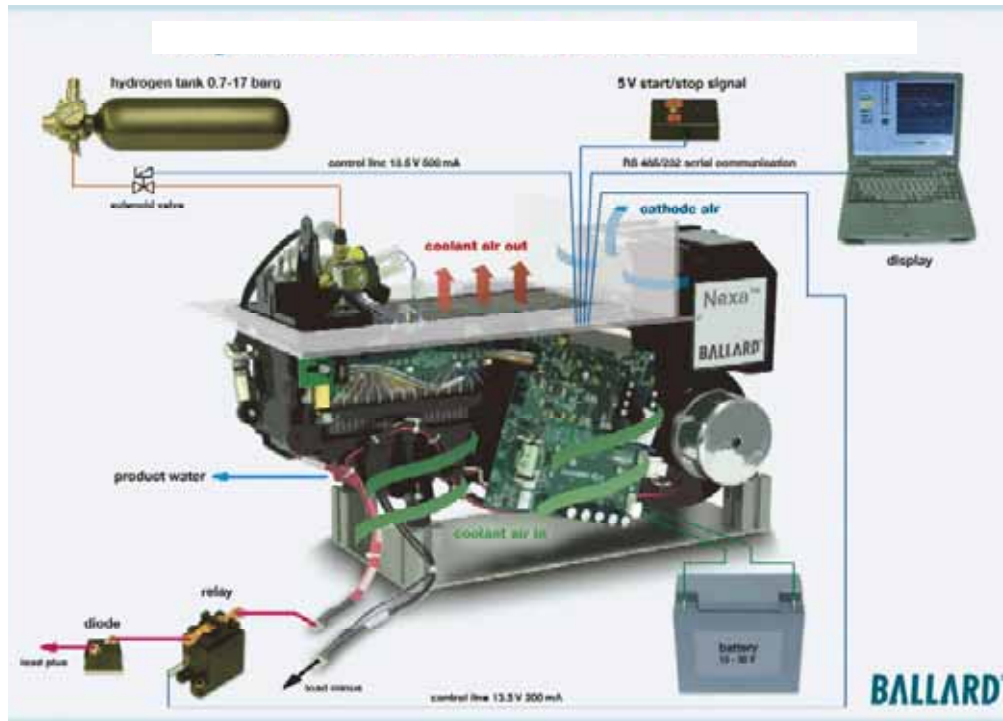


Figure 6.5: Ballard Nexa Fuel Cell.

approximately a straight line discharging curve. The advantage is that the battery exhibits a long lifetime and a better power density. In contrast, it has a constant power distribution; therefore one can not measure the SOC by measuring the voltage. The losses of this battery are measured and tested and approximated as 10% loss per 1000 cycle. When temperature rises by 10% the aging speed doubles. In vehicular applications and at ambient temperatures ranging from 20 to 25 degrees Celsius, the battery is considered dead when the SOC is at 80% full charge which implies after 2000 cycles. For other applications 50% is considered the limit for stationary power systems. Some dealers take batteries from vehicle industries that are considered dead (80% SOC) at zero prices and use them to build backup power systems. The battery system was simulated to derive its characteristics which are shown in table 6.3.

6.4 Inverter BFC2000

To emulate the system load demand at the DC bus, an electronic DC load inverter from ETSsystem [94] is used. The characteristics of the inverter are shown in table 6.4. It is connected in parallel with the battery system and consumes the power provided by the FC and battery. The power demand is specified by the

Table 6.2: Nexa Fuel Cell Characteristics.

Characteristic	Range
Rated Power	1200 W
Operating voltage range	22 V to 50 V
Voltage at Rated Power	26 V
Total system mass	13 kg
Minimum number of operating hours before End of Life	1500 hours
Temperature Range	3C-40C

Table 6.3: Serial Battery Characteristics.

Characteristic	Range
Nominal Capacity	40Ah at 0.3C Discharging
Minimum Capacity	40Ah at 0.3C Discharging
Nominal Voltage	3.2 V
Number of cells	8
Internal Resistance	1m
Recommended SOC Usage Window	10%-90%
Operation Thermal Ambient Charging	0C-45C
Operation Thermal Ambient Discharging	-20C-55C
Storage Humidity	less than 70%
Battery Weight	Around 1.4kg
Shell Material	Plastic

Table 6.4: Electronic Load Characteristics.

Characteristic	Range
DC input voltage	[0 60]V
DC input current	[0 80]A
DC input power	[0 2000]W
AC output	230 V, 50Hz

Table 6.5: Power Supply Characteristics.

Characteristic	Range
Power Supply Output Type	Adjustable
Power Rating	320W
Input Voltage Min	115VAC
Input Voltage Max	230VAC
Input Frequency	50Hz
Input Voltage	115V AC , 230V AC
Output Voltage Min	0V
Output Voltage Max	32V
Output Current Min	0A
Output Current Max	10A
Operating Temperature	40C
Power Supply Type	Voltage Converter
Weight	10kg

user through the labview interface and signals are sent to the inverter to apply these values. Thus the load limitations are between -0.44 and 2 kW.

6.5 Power Supply

The regenerative braking considers a negative load demand, thus a power supply is added to the configuration to emulate this phase. It is a 32V, 10A rated power supply by farnell [95]. The characteristics of this power supply is shown in table 6.5.

Table 6.6: Data Characteristics.

Characteristic	Range
FC maximum power (W)	800
FC minimum power (W)	60
Battery capacity (Wh)	40×26
Battery maximum power (W)	3200
Battery minimum power (W)	-440
Load maximum power (W)	2000
Load minimum power (W)	-440

6.6 Real Time System Characteristics

The real time system built in hardware and interfaced in Labview is constrained by size. The maximum power that can be supplied by the battery and the fuel cell at favorable conditions should not exceed 2 kW. The data for the components is shown in table 6.6. Although the Nexa fuel cell of the system is rated at 1.2 kW, it has lost its rated power by age. It was already existing and functional for several years in the University of Applied Sciences laboratory. For this reason, the maximum power that it can supply is 0.8 kW. The minimum supplied power by the fuel cell is 0.06 kW. This implies that the condition of shutting off the fuel cell is not available. Moreover, this minimum power is needed to run inner functionalities in the fuel cell system. The battery has power limits between -0.44 and 3.2 kW. These data were provided by the manufacturer of the battery who was attending the simulations and ensuring that the battery is supplying power when needed. The system load is limited between -4.4 and 2 kW.

The international cycles namely the highway, FUDS and NEDC, that were optimized in the previous sections have higher power demand than what the real time system can supply. In order to launch the testings, the known cycles power demand is scaled down to the maximum power demand that can be supplied by the real time system which is limited between -4.4 and 2 kW [87].

6.6.1 Load Profile Modification

To launch the testing on the system, two cycles were considered. These are the highway and the NEDC driving cycle. The power profiles of both cycles is scaled down to the system limitations. They are named the Hc and Uc cycles respectively. Hc cycle that has high speeds and slow dynamics like the highway

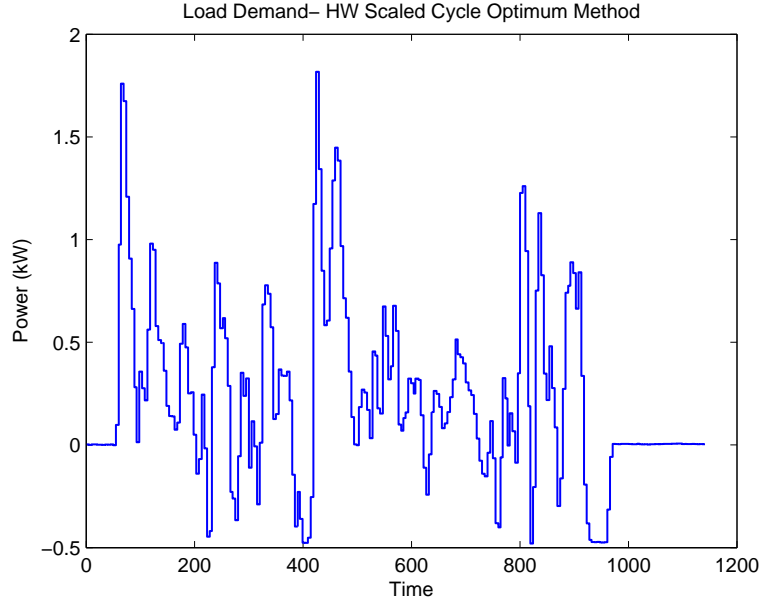


Figure 6.6: Load Curves for Hc Cycle.

cycle. Uc cycle with low speeds and fast dynamics like the urban cycles. The Hc and Uc cycle load curves are shown in figure 6.6 and figure 6.7.

6.6.2 Off-line Optimization Variables

The real time system needs the matrix derived from the off-line algorithms namely the IDP and RB. This matrix accommodates the power split between the fuel cell and battery as well as the battery SOC profile. To calculate this matrix using IDP method explained in chapter 3, the power coefficients of the cost function in equation 3.24 need to be updated.

The nexa FC is purchased at 5000\$/kW and has 1500 hours of operations. The hydrogen cost is still the same as discussed in chapter 3. The battery cost is considered around 70% of the FC cost. Nexa hydrogen consumption curve is shown in figure 6.8 calculated at standard liter per minute, measured at 1 atm, 0C. By using a basic curve fitting lambda is calculated at 0.22 g/Wsec. Therefore, the costs are updated according to equation 6.1.

$$\gamma_{FC} = 0.02\$/kWh \quad \gamma_{SL-FC} = 3.3\$/kWh \quad \gamma_{BT} = 0.7\gamma_{SL-FC} = 2.3\$/kWh \quad (6.1)$$

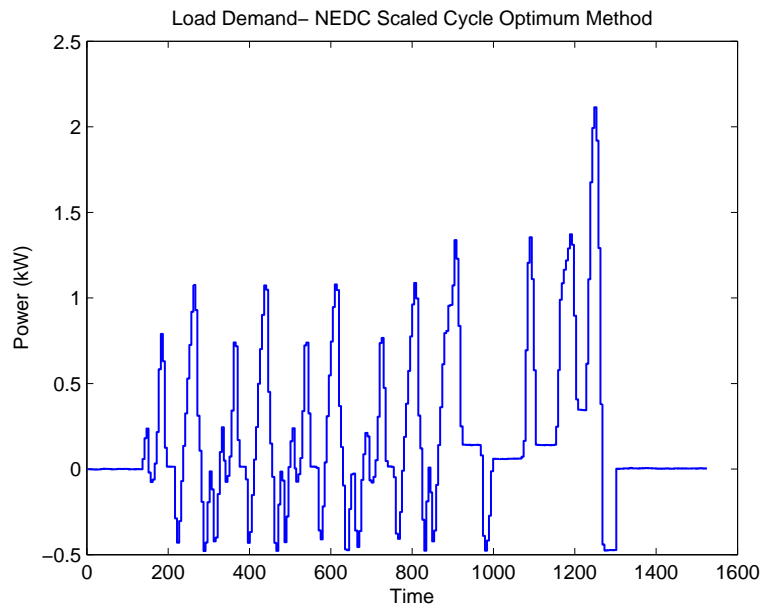


Figure 6.7: Load Curves for Uc Cycle.

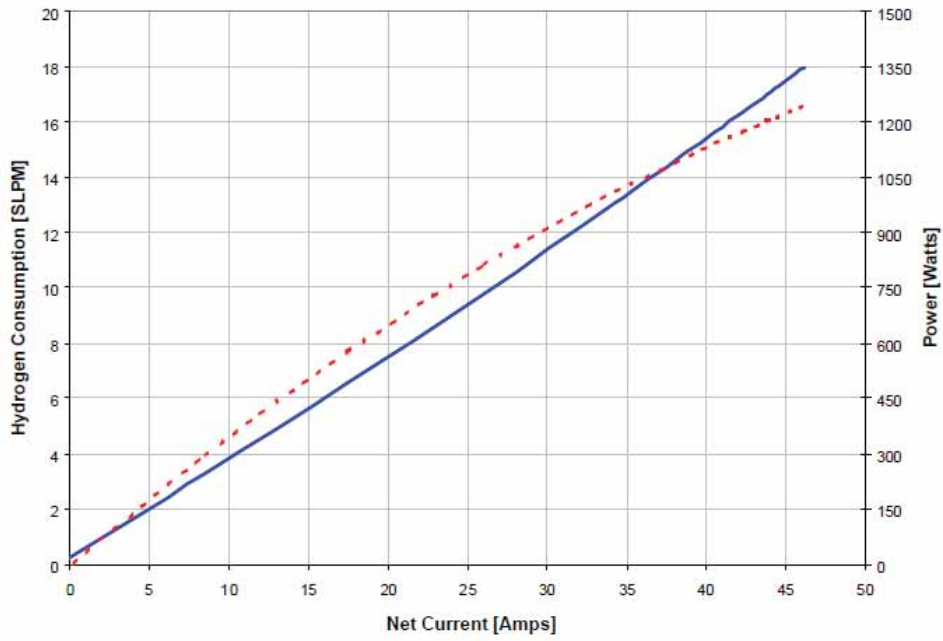


Figure 6.8: Nexa FC Hydrogen Consumption Curve.

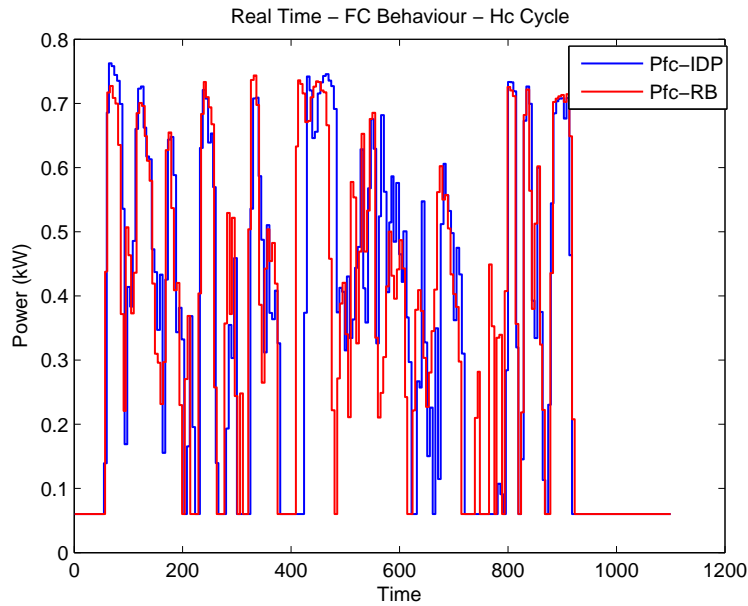


Figure 6.9: FC IDP/RB Comparative Curves during Online operation for Hc Cycle.

6.7 Real Time System Testing, Analysis and Results

The edited load profiles discussed in the previous section are embedded into the off-line Matlab based IDP algorithm as well as the RB algorithm. Four different matrices are ready for real time testing. These are the Hc cycle with power split obtained by IDP and RB method; the Uc cycle with the power allocation obtained by IDP and RB method. After these matrices are acquired, they are fed to the Labview interface of the real time simulation one after the other. With each matrix the Labview interface also takes the corresponding cycle demand. Comparisons include the power profile of the sources as well as the stresses on the sources. The latter is derived using the the standard deviation of the high frequency component of the haar wavelet transform as explained in previous chapters.

6.7.1 Real time Comparative Results

Figure 6.9 shows the behavior of the FC during the Hc cycle when using the IDP and RB algorithm. These two profiles are derived from the real time system. This means that the power allocation matrix derived from the off-line IDP runs is fed to the Labview interface. The real time system is simulated for a fixed period of

time depending on the corresponding driving cycle which is the highway scaled cycle in this case. Similarly, the power split matrix derived from the off-line RB is tested in real time system. The FC behavior in these two cases which is obtained after the real time simulation terminates is plotted in figure 6.9. In both cases the minimum fuel cell power is 60W as specified by the hardware limitations. The fuel cell is more exploited in the RB strategy. It is important to recall the characteristics of the highway cycle even the scaled one. It features high speeds and low vehicle dynamics. For this reason, it does not tend to exploit the battery charging and discharging capabilities using regenerative braking. The fuel cell is usually abused more during highway cycles. This is revealed here when using RB or IDP, the fuel cell is doing the job and supplying the power demand. By measuring the stresses on the fuel cell during the scaled highway cycle using the haar wavelet transform, it is noticed that more stresses are added on it using the RB method than while using the IDP method. The RB method does not exploit the resources in an optimum fashion so the program tends to add more stresses on them.

To clarify the fuel cell profiles more, a window of the figure 6.9 is shown in figure 6.10. The maximum fuel cell power is limited to 800W in both cases. The frequency of shifting is almost the same in both cases. However, the sudden transitions which are not beneficial for the fuel cell are more witnessed during the RB algorithm. This tends to show more stresses on the fuel cell via the haar wavelet transform.

It is noticed that using RB, the FC is exhausted more than while using the IDP method which increases the hydrogen consumption levels. The hydrogen consumption is measured in both cases for the corresponding highway scaled driving cycle. These measurements are read directly from the Nexa fuel cell Labview interface. The savings that can be achieved during the real time system are almost 13% in the hydrogen fuel consumption in favor of the IDP over the RB power allocation strategy. During off-line operation, before the power matrix is tested in the hardware in the loop method, the hydrogen fuel consumption savings between the IDP and RB strategies are 11% in favor for the IDP optimization algorithm. This discrepancy between the on-line and off-line hydrogen savings is based on the difference between the software simulations and the actual physical hardware. Mainly, the accuracy of the readings of the hydrogen consumption via the Labview interface is around 85%.

Figure 6.12 corresponds to the fuel cell profile during real time simulation while using the Uc cycle. The two tested strategies are the IDP and RB algorithms. These are the outcomes from the hardware system which sends the signals via the Labview model interface. It is observed that RB tends to exploit the FC much more than the IDP method. The Uc cycle is scaled down from the NEDC driving cycle. The characteristic of such a cycle is slow speeds and fast dynamics. The importance of the algorithmic strategy is to try to exploit the battery to preserve hydrogen fuel consumption as well as protecting the sources

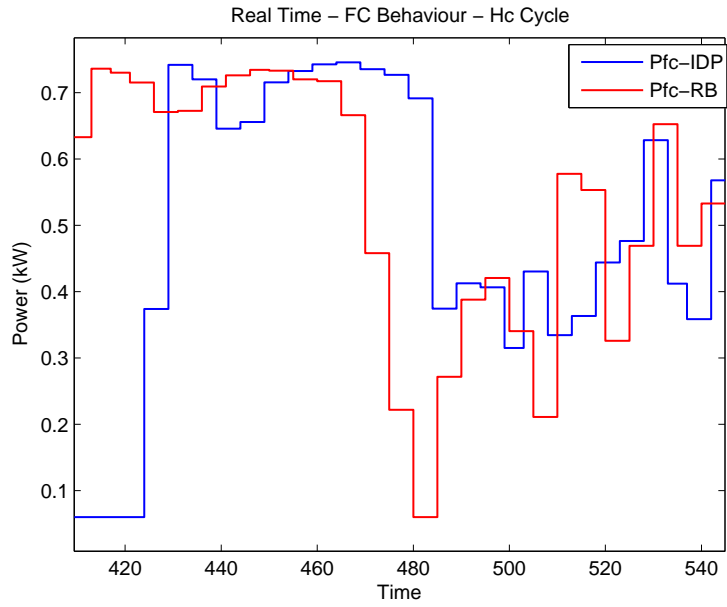


Figure 6.10: Window - FC IDP/RB Comparative Curves during Online operation for Hc Cycle.

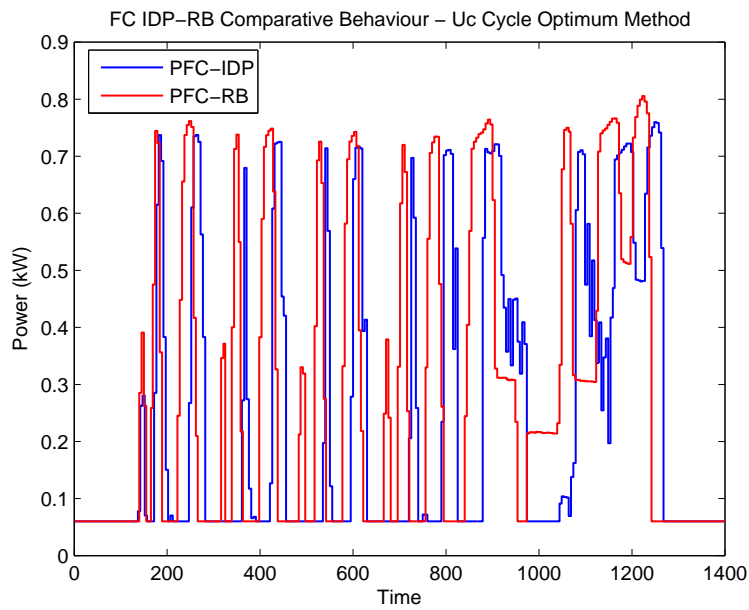


Figure 6.11: Window - FC IDP/RB Comparative Curves during Online operation for Uc Cycle.

from the fast dynamics of such a cycle. A window of the fuel cell behavior using the IDP and RB algorithms is shown in Figure 6.11. The RB algorithm is revealed to exploit the fuel cell more than the IDP algorithm. The latter tries to harness energy from the regenerative braking and supplies the system more efficiently. Using haar wavelet transform, the stresses on the fuel cell are calculated using the two algorithms. The RB algorithms exerts 8% more stresses on the fuel cell rather than the IDP algorithm. This tends to decrease the life of the fuel cell. The existing fuel cell has already been extensively used in the UAS labs which limited it from supplying the maximum output power of 1.2kW and only supplying a maximum of 0.8kW. By using the RB algorithm this tends to limit the fuel cell maximum power more and thus deteriorate it.

The hydrogen consumption savings is derived for both power allocation strategies. During the real time simulations the savings in the consumption is up to 21% in advantage to the IDP optimization strategy. This percentage is higher than that for the highway scaled cycle one. It is expected because in urban cycles the battery is exploited more due to the fast dynamics that characterize the cycle. This relaxes the fuel cell more and thus lowers down the hydrogen consumption. The hydrogen savings achieved from the off-line simulations of the IDP and RB strategies mark a 30% saving in favor of the IDP method. This discrepancy in savings between the real time simulations and the off-line simulations results from the errors in the actual model of the hardware. Moreover, the technique used to supply the fuel cell with the actual hydrogen could not be perfectly modeled. The hydrogen consumption curve for the fuel cell adopted from the data sheet corresponds to a new fuel cell and the one available was abused as shown from its maximum power limits.

Another obstacle arising from the hardware in the loop system is the failure of reading the battery output power from the system. The battery output power is calculated based on the balance of the power equation. Using the fuel cell power levels and the load demand, the battery output power can be concluded. The battery SOC could also be estimated. This was enough to compare the behavior of the battery during the real time simulations and the off-line runs.

The battery power profile for the IDP and RB algorithms based on the highway scaled and NEDC scaled driving cycles is shown in figures 6.13 and 6.14. These are derived from the Labview interface during the real time system simulation. The IDP method in both scenarios tends to exploit the battery more so as to lower the hydrogen consumption levels. The battery is kept between its limits so as not to violate the system constraints. The stresses on the battery are 7% more when using the IDP method over the RB method for the urban cycle. This percentage is lowered down to 3% during highway scaled cycle. This is one of the trade-offs between the IDP and RB methods. Savings in hydrogen consumption is more notable while using the IDP optimal power allocation strategy while a slight increase in the battery stresses is witnessed. The stresses on the battery while driving the urban cycle increase to 7% with IDP. The cycle has

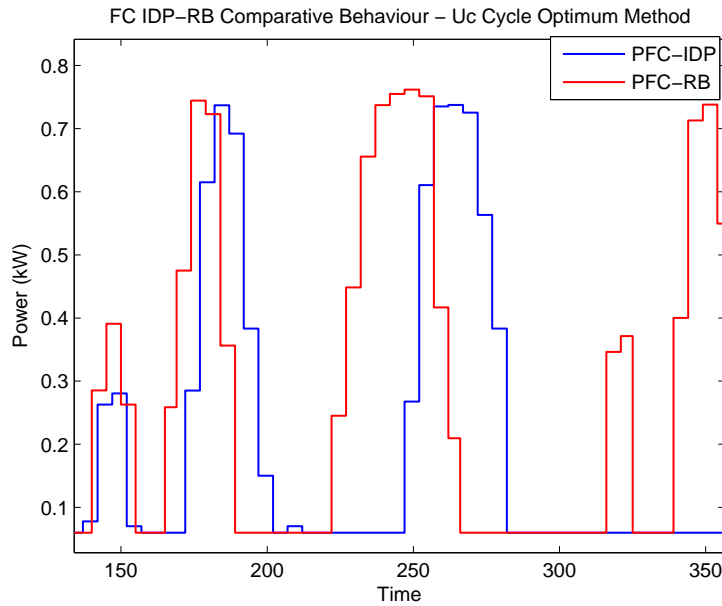


Figure 6.12: FC IDP/RB Comparative Curves during Online operation for Uc Cycle.

high dynamics which make the IDP algorithm exploit the battery more so as to save hydrogen fuel.

6.7.2 Real time/Off-line Comparative Results

The real time system is built to verify the results obtained from software simulations. The fuel cell power profile, the battery power profile and the battery SOC profile that are derived during the off-line runs of the IDP algorithm need to match those derived from the real time hardware in the loop model with the Labview interface. The degree of matching between the off-line and real time system results depend on several factors. First, the efficiency of the off-line models. The fuel cell and battery models used in the off-line simulations emulated the actual ones. However, software models can never exactly mimic the actual behavior of the components. For example, in the off-line model of the fuel cell, the hydrogen consumption curve provided by the fuel cell manual is used. In reality, the life of the fuel cell has decreased due to extensive use. This is revealed from the maximum output power that the fuel cell is supposed to supply which is 1.2kW and the actual one supplied which is 800W. Second, the errors in reading the actual values from the real time system. The battery is manually designed and several factor can not be read because they are not software interfaced and for this reason manual calculations were performed. Finally, losses in the system

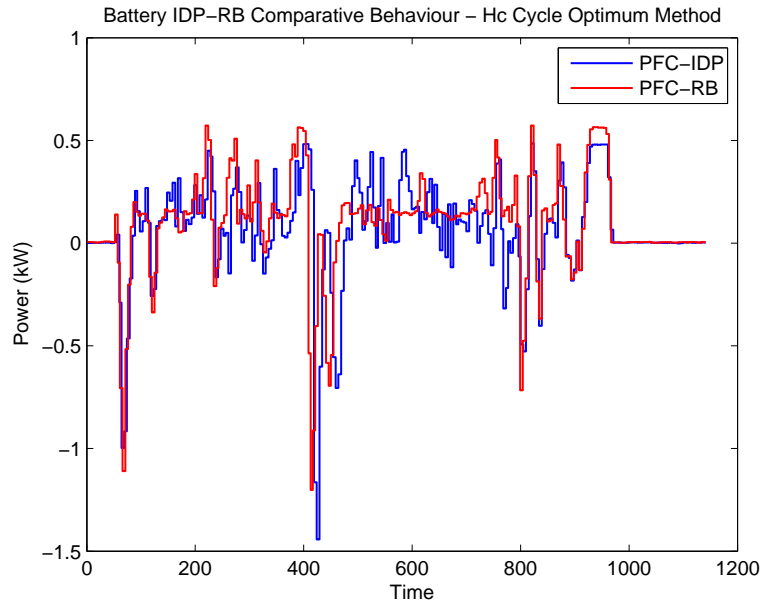


Figure 6.13: Battery IDP/RB Comparative Curves during Online operation for Hc Cycle.

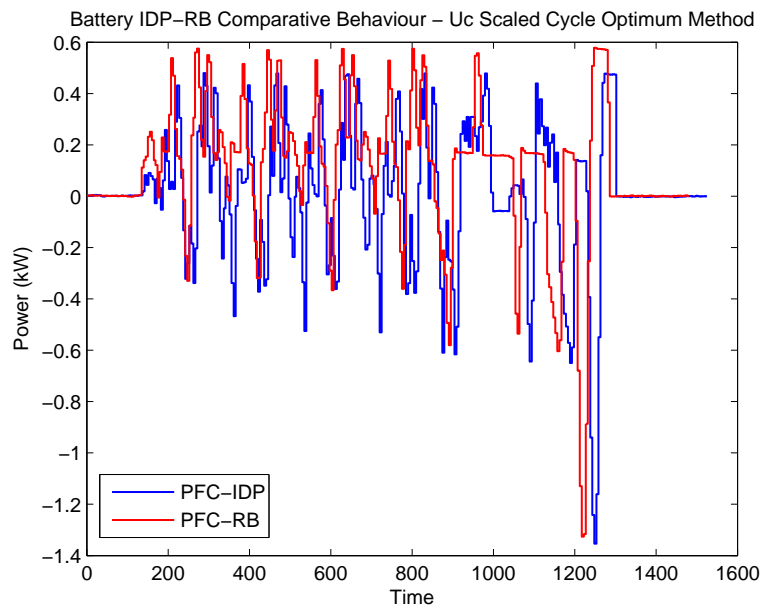


Figure 6.14: Battery IDP/RB Comparative Curves during Online operation for Uc Cycle.

sources even if modeled based on the measured data can not emulate the actual real time losses. However, within a certain tolerance, the results tend to match as discussed below.

The comparison between the off-line and real time curves is based on the root mean square error (RMSE). This method is often used to quantify the difference between the values predicted by a model (x) and the values experimentally observed (\hat{x}) over a number of samples N . The equation used for such a calculation is shown in equation 6.2. The lower the value of this error the better is the system model.

$$RMSE = \sqrt{\frac{\sum_1^N (x - \hat{x})^2}{N}} \quad (6.2)$$

Figure 6.15 compares the fuel cell profiles derived from the off-line and real time runs of the IDP power allocation strategy while incorporating the highway scaled driving cycle. The IDP algorithm is simulated for the respective load and then feeds the values of the power levels of the FC and battery to the on-line system through the Labview model interface. There is an approximate match between the real time and off-line results. Using the software the maximum power of the FC is limited to 0.8kW because it is presumed that this is the maximum power that the FC can supply. Although the FC is rated at 1.2kW, it's frequent usage by the university labs shaved its rated power to 0.8kW. However, sometimes it can still provide a bit higher than the rated value. Moreover, errors might occur in the readings because the FC might have a sudden unexpected purge voltage loss which was noticed while running the tests for several times. It is calculated that the error in matching the real time and off-line FC power curves is 0.36 for Hc cycle which is an acceptable value.

Similarly for the urban cycle, the fuel cell power profile comparison between the real time and off-line simulations while using IDP is shown in figure 6.16. The degree of match is high, however there were some errors that occurred during the measurements because of the cycle dynamics which tend to overuse the fuel cell and battery. The error of mismatch is found to be 0.3 which is fairly good for the system.

The behavior of the state of charge of the battery during real time and off-line simulations is also compared. The SOC curves for the Hc and Uc cycles are shown in figures 6.17 and 6.18. Losses are added cumulatively to the battery SOC at each step at a rate of 6μ . The matching between the off-line and on-line SOC for the two methods is approximately perfect giving a RMSE of 0.004 for the Hc cycle and 0.005 for the Uc cycle. This verifies that the battery power curves have some errors in their reading and not their SOC results.

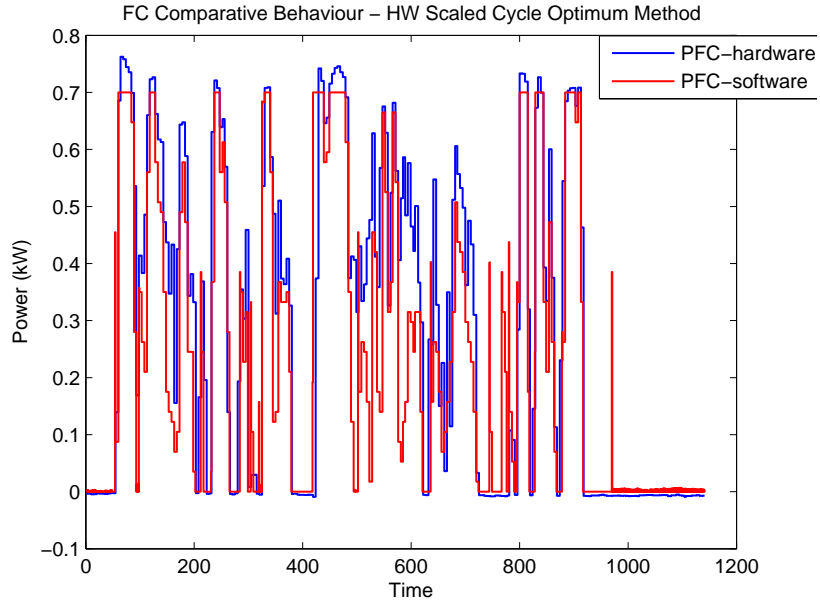


Figure 6.15: FC IDP online/offline Comparative Curves for Hc Cycle.

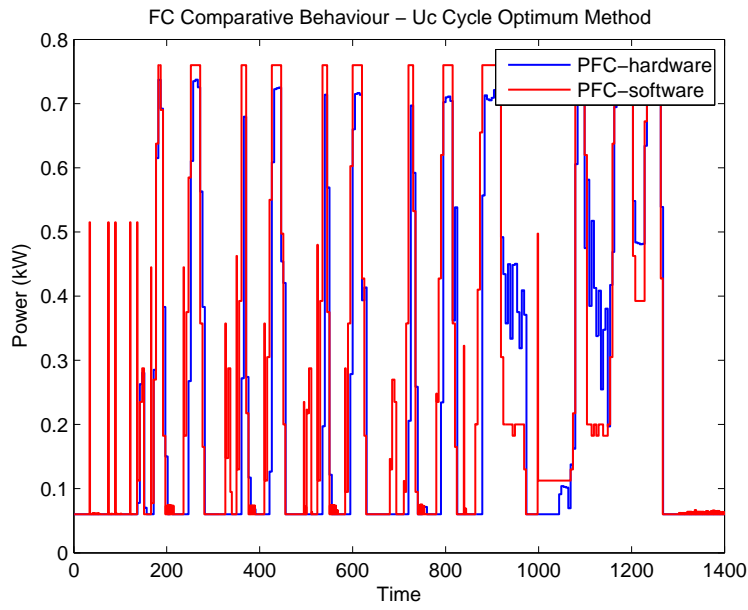


Figure 6.16: FC IDP online/offline Comparative Curves for Uc Cycle.

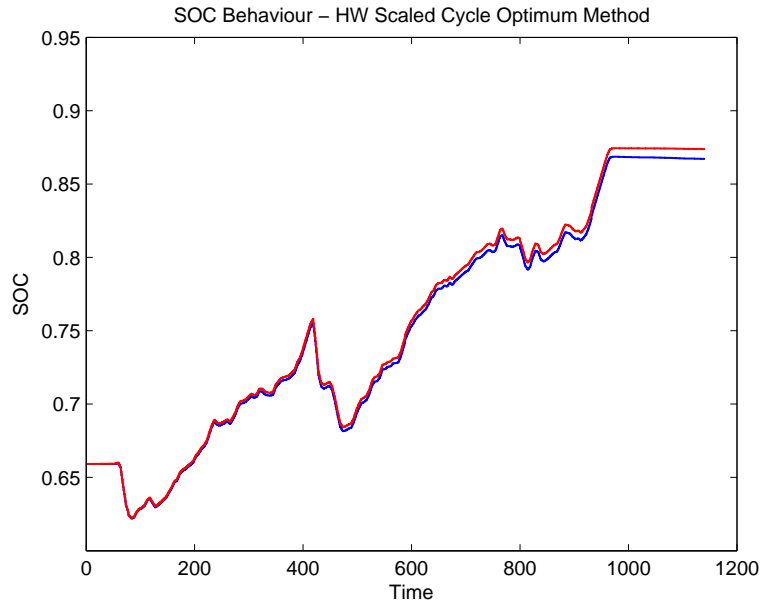


Figure 6.17: SOC IDP online/offline Comparative Curves for Hc Cycle.

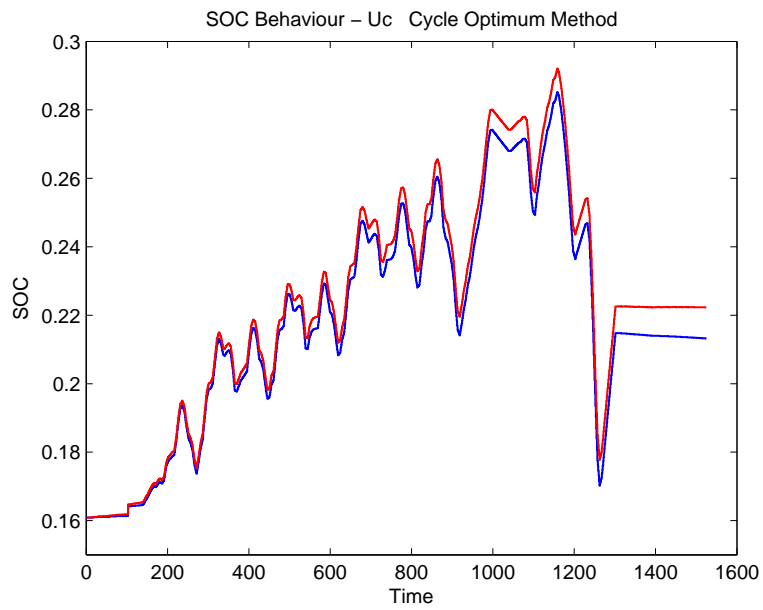


Figure 6.18: SOC IDP online/offline Comparative Curves for Uc Cycle.

6.8 Summary

The objective of this chapter is to validate the results achieved during the off-line runs using Matlab. A real time, low cost hardware in the loop model is built for this purpose. It emulates the power flow between the sources in the power train of the FCHV. The system has limited supply of power so the power profiles of the known driving cycles are scaled down to be used for testing. The outcomes are summarized in the bullets below:

- The IDP proved superiority over the RB method in real time simulations as well as the off-line runs. Real time savings in hydrogen consumption while running the scaled highway and urban cycles are 13 percent and 21 percent respectively.
- The experimental validations aim at testing the degree of matching between the profiles of the fuel cell and battery SOC. For the IDP optimal power allocation strategy, there is a high match between the fuel cell curves which are achieved in the real time simulations and off-line runs. The root mean square error is calculated to be less than 0.4 for highway scaled and urban cycles. This error is due to the fuel cell mechanics and its purge voltage losses which results in a higher power consumption.
- The SOC profiles exhibit a better match between the off-line and real time simulations, with RMSE error of less than 0.005. The profiles are compared for the real time and off-line simulations of both the scaled highway and urban cycles.

Chapter 7

Conclusions

This dissertation presented a methodology to optimize the controller of FCHV based on an improved dynamic programming technique. The problem formulation took into account the life-cycle cost of the system components and considers minimizing hydrogen usage along with operational cost. Detailed Simulink model of the vehicle subsystems is built. Test simulations were performed on driving cycles. The objective is to develop a conceptual approach for an energy optimization which is able to consider a wide range of constraints and targets. The simulations in this dissertation served to explain and to prove the process. Comparison against a rule based EMS indicated that the system cost can be reduced depending on the driving cycle.

7.1 Contributions

The novelty and contribution of the dissertation is through formulating and executing the improved dynamic programming technique. Out of the other techniques presented, it proves superiority over LP and DP in achieving a fast and feasible sub-optimal solution for the off-line resource allocation problem. The Simulink model that is developed and edited to accommodate for the sub-optimal off-line results, succeeded in emulating the actual vehicle performance. The estimation of the driving cycle presented a new method for optimizing the vehicle performance even when the cycle is not known. In essence, the technique is applied in smaller chunks targeting real time optimization. A summary of the main contributions of this dissertation are stated.

- Studying the optimal conditions for a FCHV energy management system. Four algorithms are discussed, linear programming, linear improved dynamic programming, improved dynamic programming and state control based EMS. First linear programming is formulated using linear constraints and simulated for highway and urban cycles to achieve the global optimum. Then linear improved dynamic programming is explained, formulated and

simulated for the mentioned cycles. Comparison between the LP and linear IDP validates the improved dynamic programming algorithm. This is due to the fact that linear IDP is formulated based on the known tunnel dynamic programming as well as personal expertise in the corresponding driving cycles and due to the fast dynamics of the urban cycles. Next, the IDP is formulated which considers the non-linear hydrogen consumption curve of the FC and the non-linear battery Q-maps which is adopted for this dissertation. Battery weights are added to the cost function to tune the battery behavior between charge depleting, charge sustaining and charging modes.

- The second consideration is to account for analogous, unknown and special event driving cycles. For analogous cycles, a stochastic approximation of the driving cycle is calculated using a transition probability matrix for known power demands. Then a stationary probability distribution is developed and the driving cycle is approximated based on vehicle speed, speed limit and traffic coefficient. IDP is used for two such cycles. For unknown cycles a looping methodology is applied based on a 50 second window and a known cycle. The looping technique is performed using the IDP algorithm as well as the state control rule based algorithm. Results prove the lower levels of hydrogen consumption that could be achieved. Finally, the special events that occur during known driving cycles are also considered. The optimal allocation is updated before the incident happens and benefits from any vehicle deceleration occurring for energy recuperation.
- The FCHV Simulink model built at the University of Applied Sciences in Germany is fully comprehended in-order to launch the testing for the FCHV system under study. The energy management system block is completely changed to fit the design proposed in this dissertation. Results show the actual FC current performance as well as the battery SOC profile. On-line monitoring of the vehicle performance is achieved using classic PI controller.
- A system built as hardware in the loop using Labview is tested against the state control rule based model and IDP. Comparative savings witnessed on the system measuring the difference in on-line hydrogen consumption when the IDP algorithm is applied and the RB algorithm is applied.

The performance criteria are based on the overall operational cost as well as the hydrogen consumption per trip. Savings in cost and hydrogen consumption are witnessed in the highway cycle and FUDS cycle as compared to state space rule based methods. The savings in hydrogen consumption are 0.06% and 0.3% for the highway and FUDS cycles respectively. However, the runtime of the latter is lower. So mainly, it is a trade-off between cost and runtime. The stresses on the FCHV subsystem sources are approximated based on a wavelet transform

of instantaneous power of the system sources. More stresses are added on the battery in urban cycles than on highway cycles. The simulations indicate that the proposed method leads to savings in hydrogen consumption levels and costs.

7.2 Future Work

The work discussed in this dissertation could be extended in different areas. There are several open ended questions that could be addressed in-order to develop a general purpose optimal algorithm for hybrid fuel cell vehicles.

One suggestion would be to develop a prototype for the controller of a real FCHV and test it on the developed IDP algorithm proposed in this thesis. The integration of the algorithm into a real hybrid vehicle evaluates the actual on-line performance of the algorithms [96]. Moreover, the possibility of installing an optimization console on an actual vehicle will give rise to the limitations faced. This might tend to tweak or change some parts of the algorithm.

Secondly, it is important to link the IDP with sizing optimization algorithm to arrive at an overall optimized vehicle. This becomes like an optimal looping methodology. The size setting can be one multi-objective optimization problem, the EMS could be another optimization problem. The two problems are linked together via efficiency, performance and requirement analysis. A similar technique was applied to a stationary hybrid renewable energy system [97]. The optimal sizes of the system components are derived using linear programming. The sizes are then applied to the on-line system that is running and feeding the load. The sizes are evaluated based on the total cost of the system.

Thirdly, forecast of the road data is required to train and build unknown driving cycles. Such a forecast requires a collection of data. This combines the traffic data, population capacity, employment rate, trip rate, travel costs, weather data and political situations. These data can be extended more in-order to provide estimates of future road traffic. The road is usually segmented similar to the idea behind chapter 5, and typically the fore-cast will be for the next infrastructure in question.

Another proposal is to investigate the possibility of using neural networks as a learning algorithm. After incorporating the vehicle optimal sizes, the IDP algorithm and the cycle fore-cast, a neural network that can be trained based on these data. This can present a framework in-order to acquire the knowledge behind size optimization, EMS optimization and cycle fore-cast for a certain vehicle [96].

Appendix A

Abbreviations and Notations

A.1 Abbreviations

FCHV: Fuel cell hybrid vehicles
HEV: Hybrid electric vehicles
ICE: Internal combustion engine
EMS: Energy management system
EEMS: Efficient Energy management system
FC: Fuel cells
PEM: Proton exchange membrane
SOC: Battery state of charge
ECMS: Equivalent fuel consumption minimization strategy
DP: Dynamic programming
LP: Linear programming
IDP: Improved dynamic programming
LIDP: Linear Improved dynamic programming
WIDP: Weighted improved dynamic programming
SDP: Stochastic dynamic programming
UAS: University of applied sciences
RB: State machine rule based technique
Cons.: Consumption
RMSE: Root Mean Square Error
CDM: Charge Depletion Mode
CSM: Charge Sustaining Mode
CM: Charging Mode

A.2 Notations

Notation	Definition
----------	------------

P_{FC}	FC Power request (kW)
P_{BT}	Battery Power request (kW)
P_L	Load Demanded Power (kW)
\dot{m}_{H_2}	Flow rate of reacted hydrogen (g/s)
\dot{m}_{air}	Flow rate of air (g/s)
M_{H_2}	Molar mass of Hydrogen (g/mol)
M_{O_2}	Molar mass of Oxygen (g/mol)
λ_{O_2}	Oxygen Excess Ratio (g/mol)
λ_{H_2}	Hydrogen Excess Ratio (g/mol)
n_{st}	Number of cell in the FC system
F	Faraday number (C/mol)
I_{st}	FC stack current (C/s)
V_{st}	FC stack voltage (V)
I_{FC-req}	FC cell current request (A)
I_{FCmax}	Maximum FC cell current request (A)
P_{fc-aux}	Power consumed by the FC auxiliaries (kW)
w_{O_2}	Molar fraction of oxygen in air
$P_{FC-losses}$	Losses in the fuel cell system (kW)
P_{FC-req}	FC power request (kW)
P_{FCmax}	FC maximum power request (kW)
P_{FCmin}	FC minimum power request (kW)
V_{FC}	FC polarization voltage (V)
$R_{down-fc}$	FC ramp down power (kW)
R_{up-fc}	FC ramp up power (kW)
n	number of electrons
η_m	Motor Efficiency
τ_m	Motor Torque (Nm)
ω_m	Motor rotational speed (rpm)
P_{motor}	Motor power request (kW)
P_{loss}	Motor power losses (kW)
I_{BT}	Battery current (A)
R_{BT}	Battery internal resistance (Ohm)
C_{BT}	Battery nominal capacity (Ah)
OCV	Battery open circuit voltage (V)
V_{BT-oc}	Battery open circuit voltage (V)
V_{BT-oc0}	Initial Battery open circuit voltage (V)
V_{BT-min}	Battery Minimum voltage (V)
V_{BT-max}	Battery Maximum voltage (V)
U_{BT}	Battery voltage (V)
β_{BT}	Battery damping factor
α_{OCV}	Battery temperature coefficient for OCV (V/K)
α_{R-SOC}	Battery resistive-SOC dependency coefficient
α_{R-T}	Battery resistive-temperature dependency coefficient

T_{BT}	Battery temperature (degrees Celsius)
T_{amb}	Ambient temperature (degrees Celsius)
n_{BT}	Number of cell in the Battery system
H_{BT}	Battery heat capacity of battery (J/K)
δ_{siBT}	Entropy of cell reaction (J/(A.s. K))
SOC	Battery state of charge
P_{BT}	Battery power (kW)
Q_{BT}	Battery power with losses (kW)
P_{BTmax}	Battery maximum power request (kW)
P_{BTmin}	Battery minimum power request (kW)
$R_{down-bt}$	Battery ramp down power (kW)
R_{up-bt}	Battery ramp up power (kW)
SOC_{min}	Battery SOC minimum level
SOC_{max}	Battery SOC maximum level
η_{BT}	Battery Efficiency
$I_{BT-ch-max}$	Battery maximum permissible charging current (A)
$I_{BT-disch-max}$	Battery maximum permissible discharging current (A)
V_{bus}	Voltage on the DC bus (V)
V_{RegB}	Regenerative braking Voltage (V)
η_{buck}	Efficiency of the buck converter
η_{boost}	Efficiency of the boost converter
i_{dc-in}	Converter input current (A)
i_{dc-out}	Converter output current (A)
H_a	Actual Vehicle height (m)
H_{in}	Initial Vehicle height (m)
v_a	Actual Vehicle speed (m/sec)
P_a	Actual Vehicle pressure (atm)
P_{in}	Initial Vehicle pressure (atm)
g	9.8 m per seconds square
M	Molar mass of Earth's air
R_{air}	Universal gas constant
V	Volume of hydrogen in the tank (l)
R_w	Tyre radius (m)
F_{trac}	Tractive force (Nm)
F_{res}	Driving resistance force (Nm)
F_{brake}	braking force (Nm)
θ_t	Total vehicle moment of inertia
θ_w	Wheel moment of inertia
θ_m	Motor moment of inertia
F_r	Rolling resistance force (Nm)
m_v	Vehicle mass (kg)
α_s	slope angle
f_{rol}	rolling resistance factor

F_w	Air drag force (Nm)
C_D	Drag coefficient
A	Frontal area (square meter)
ρ_{air}	Air density
τ_{br}	Rear braking torque (Nm)
τ_{bf}	Frontal braking torque (Nm)
τ_{req}	Torque request(Nm)
k_p	PID Controller proportional factor
k_i	PID Controller integral factor
k_d	PID Controller derivative factor
e	PID Controller error signal
a_w	PID Controller overflow factor
τ_T	Transmission system output torque (Nm)
g_r	Gear Ratio
P_{Tloss}	Transmission system power losses (kW)
ω_T	Transmission system rotational speed (rpm)
S_{FC}	FC on/off signal
γ_{FC}	The cost of hydrogen consumption (\$/kWh)
γ_{SL-FC}	The initial cost of FC system (\$/kWh)
γ_{BT}	The cost of Battery system (\$/kWh)
λ	Consumption rate of hydrogen molecules per kW (g/kWh)
MH_o	Initial mass of hydrogen in the tank (g)
δt	Sample duration time (seconds)
N_{iu_j}	Node Representation
C_{iu_j}	Node Cost
R_{u_k,iu_j}	Transition Cost
V_{iu_j}	Fitness function
g_{u_k,iu_j}	Transition function
v_h, v_u, v_e	Speed vectors for highway, urban and European cycles
w_a, w_b, w_c	IDP weights
w_h, w_u, w_e	Transition matrix cycle weights
v_{hs}	Two minutes highway cycle speed
v_{us}	Two minutes urban cycle speed
v_{hs-max}	Two minutes highway cycle maximum speed
v_{us-max}	Two minutes urban cycle maximum speed
$Splim$	Speed limit
ρ_{Tr}	Traffic coefficient
$\hat{v}_{m,k:1 \rightarrow N}$	Loop IDP: Current window speed forecast
$\hat{v}_{k:N+1 \rightarrow 2N}$	Loop IDP: Next window speed forecast
$\hat{P}_{L,k:1 \rightarrow N}$	Loop IDP: Forecasted power demand of the current window
SOC_f	Loop IDP: Final state of charge of the battery per window
$\hat{P}_{FC,k:1 \rightarrow N}$	Loop IDP: Forecasted fuel cell power demand of the current window

$\hat{P}_{BT,k:1 \rightarrow N}$	Loop IDP: Forecasted battery power demand of the current window
$P_{L,k:1 \rightarrow N}$	Loop IDP: Power demand of the current window
ΔP	Loop IDP: Error in power measure
$\hat{P}_{FC-req,k:1 \rightarrow N}$	Loop IDP: Power requested from the fuel cell system
$P_{FC,k:1 \rightarrow N}$	Loop IDP: Fuel Cell power demand of the current window
$P_{BT,k:1 \rightarrow N}$	Loop IDP: Battery power demand of the current window
$P_{BT-req,k:1 \rightarrow N}$	Loop IDP: Power requested from the battery system
$P_{br,k:1 \rightarrow N}$	Loop IDP: Braking power demand of the current window
P_{wheels}	Power demand at the level of the wheels
P_m	Power demand at the level of the electric motor
V_{req}	Vehicle reference speed
V_{act}	Vehicle measured speed

Bibliography

- [1] D. Greene, H. Baker, and S. Plotkin, “Reducing greenhouse gas emissions,” *Prepared for the Pew Center on Global Climate Change*, Jan 2011.
- [2] J. V. Mierlo, G. Maggetto, and P. Lataire, “Which energy source for road transport in the future? a comparison of battery, hybrid and fuel cell vehicles,” *Energy Conversion and Management*, vol. 47, no. 17, pp. 2748 – 2760, 2006.
- [3] K. Bayindir, M. A. Gozukucuk, and A. Teke, “A comprehensive overview of hybrid electric vehicle: Powertrain configurations, powertrain control techniques and electronic control units,” *Energy Conversion and Management*, vol. 52, no. 2, pp. 1305 – 1313, 2011.
- [4] M. Abu mallouh, B. Surgenor, B. Denman, and B. Peppley, “Analysis and validation of a powertrain system analysis toolkit model of a fuel cell hybrid rickshaw,” *International Journal of Energy Research*, vol. 35, no. 15, pp. 1389–1398, 2011.
- [5] M. J. Khan and M. T. Iqbal, “Modelling and analysis of electro-chemical, thermal, and reactant flow dynamics for a pem fuel cell system,” *Fuel Cells*, vol. 5, no. 4, pp. 463–475, 2005.
- [6] P. Ksiazek and M. Ordonez, “Swinging bus technique for ripple current elimination in fuel cell power conversion,” *IEEE Transactions on Power Electronics*, vol. 29, no. 1, pp. 170–178, 2014.
- [7] D. Zhao, F. Gao, D. Bouquain, M. Dou, and A. Miraoui, “Sliding-mode control of an ultrahigh-speed centrifugal compressor for the air management of fuel-cell systems for automotive applications,” *IEEE Transactions on Vehicular Technology*, vol. 63, no. 1, pp. 51–61, 2014.
- [8] Y. Zheng, Z. Y. Dong, Y. Xu, K. Meng, J. H. Zhao, and J. Qiu, “Electric vehicle battery charging/swap stations in distribution systems: Comparison study and optimal planning,” *IEEE Transactions on Power Systems*, vol. 29, no. 1, pp. 221–229, 2014.

- [9] F. Ju, J. Li, G. Xiao, N. Huang, and S. Biller, "A quality flow model in battery manufacturing systems for electric vehicles," *IEEE Transactions on Automation Science and Engineering*, vol. 11, no. 1, pp. 230–244, 2014.
- [10] B. Whitaker, A. Barkley, Z. Cole, B. Passmore, D. Martin, T. McNutt, A. Lostetter, J. Lee, and K. Shiozaki, "A high-density, high-efficiency, isolated on-board vehicle battery charger utilizing silicon carbide power devices," *IEEE Transactions on Power Electronics*, vol. 29, no. 5, pp. 2606–2617, 2014.
- [11] B. Vural, S. Dusmez, M. Uzunoglu, E. Ugur, and B. Akin, "Fuel consumption comparison of different battery/ultracapacitor hybridization topologies for fuel-cell vehicles on a test bench," *IEEE Journal of Emerging and Selected Topics in Power Electronics*, no. 1, p. 1, 2014.
- [12] M. Pahlevaninezhad, D. Hamza, and P. Jain, "An improved layout strategy for common-mode emi suppression applicable to high-frequency planar transformers in high-power dc/dc converters used for electric vehicles," *IEEE Transactions on Power Electronics*, vol. 29, no. 3, pp. 1211–1228, 2014.
- [13] Z. Amjadi and S. Williamson, "Digital control of a bidirectional dc/dc switched capacitor converter for hybrid electric vehicle energy storage system applications," *Smart Grid, IEEE Transactions on*, vol. 5, no. 1, pp. 158–166, 2014.
- [14] P. Xuewei and A. Rathore, "Novel bidirectional snubberless naturally commutated soft-switching current-fed full-bridge isolated dc/dc converter for fuel cell vehicles," *Industrial Electronics, IEEE Transactions on*, vol. 61, no. 5, pp. 2307–2315, 2014.
- [15] A. Dalvi and M. Guay, "Control and real-time optimization of an automotive hybrid fuel cell power system," *Control Engineering Practice*, vol. 17, no. 8, pp. 924 – 938, 2009.
- [16] J. Ryu, Y. Park, and M. Sunwoo, "Electric powertrain modeling of a fuel cell hybrid electric vehicle and development of a power distribution algorithm based on driving mode recognition," *Journal of Power Sources*, vol. 195, no. 17, pp. 5735 – 5748, 2010.
- [17] Q. Ning, D. Xuan, and Y. Kim, "Modeling and control strategy development for fuel cell electric vehicles," *International Journal of Automotive Technology*, vol. 11, no. 2, pp. 229–238, 2010.
- [18] P. Pisu, K. Koprubasi, and G. Rizzoni, "Energy management and drivability control problems for hybrid electric vehicles," in *44th IEEE Conference on Decision and Control*, pp. 1824–1830, 2005.

- [19] O. Erdinc and M. Uzunoglu, “Recent trends in {PEM} fuel cell-powered hybrid systems: Investigation of application areas, design architectures and energy management approaches,” *Renewable and Sustainable Energy Reviews*, vol. 14, no. 9, pp. 2874 – 2884, 2010.
- [20] S. Motapon, L. Dessaint, and K. Al-Haddad, “A comparative study of energy management schemes for a fuel-cell hybrid emergency power system of more-electric aircraft,” *IEEE Transactions on Industrial Electronics*, vol. 61, no. 3, pp. 1320–1334, 2014.
- [21] M. J. Kim and H. Peng, “Power management and design optimization of fuel cell/battery hybrid vehicles,” *Journal of Power Sources*, vol. 165, no. 2, pp. 819–832, 2007.
- [22] A. Ravey, B. Blunier, and A. Miraoui, “Control strategies for fuel-cell-based hybrid electric vehicles: From offline to online and experimental results,” *IEEE Transactions on Vehicular Technology*, vol. 61, no. 6, pp. 2452–2457, 2012.
- [23] E. T. Stephen and S. P. Boyd, “Finding ultimate limits of performance for hybrid electric vehicles,” *SAE Paper*, 2000.
- [24] A. Brahma, Y. Guezennec, and G. Rizzoni, “Optimal energy management in series hybrid electric vehicles,” in *Proceedings of the American Control Conference*, vol. 1, pp. 60–64, 2000.
- [25] M. Gielniak and Z. Shen, “Power management strategy based on game theory for fuel cell hybrid electric vehicles,” in *IEEE 60th Vehicular Technology Conference*, vol. 6, pp. 4422–4426, 2004.
- [26] A. Piccolo, L. Ippolito, V. ZoGaldi, and A. Vaccaro, “Optimisation of energy flow management in hybrid electric vehicles via genetic algorithms,” in *IEEE/ASME International Conference on Advanced Intelligent Mechatronics*, vol. 1, pp. 434–439, 2001.
- [27] I. Sarioglu, O. Klein, H. Schroder, and F. Kucukay, “Energy management for fuel-cell hybrid vehicles based on specific fuel consumption due to load shifting,” *IEEE Transactions on Intelligent Transportation Systems*, vol. 13, no. 4, pp. 1772–1781, 2012.
- [28] S. Delprat, J. Lauber, T. Guerra, and J. Rimaux, “Control of a parallel hybrid powertrain: optimal control,” *IEEE Transactions on Vehicular Technology*, vol. 53, no. 3, pp. 872–881, 2004.
- [29] B. Geng, J. Mills, and D. Sun, “Two-stage energy management control of fuel cell plug-in hybrid electric vehicles considering fuel cell longevity,” *IEEE Transactions on Vehicular Technology*, vol. 61, no. 2, pp. 498–508, 2012.

- [30] H. D. Lee and S. K. Sul, “Fuzzy-logic-based torque control strategy for parallel-type hybrid electric vehicle,” *IEEE Transactions on Industrial Electronics*, vol. 45, no. 4, pp. 625–632, 1998.
- [31] J. Moreno, M. Ortuzar, and J. Dixon, “Energy-management system for a hybrid electric vehicle, using ultracapacitors and neural networks,” *IEEE Transactions on Industrial Electronics*, vol. 53, no. 2, pp. 614–623, 2006.
- [32] C. Y. Li and G. P. Liu, “Optimal fuzzy power control and management of fuel cell/battery hybrid vehicles,” *Journal of Power Sources*, vol. 192, no. 2, pp. 525 – 533, 2009.
- [33] W. Greenwell and A. Vahidi, “Predictive control of voltage and current in a fuel cell 2013;ultracapacitor hybrid,” *IEEE Transactions on Industrial Electronics*, vol. 57, no. 6, pp. 1954–1963, 2010.
- [34] J. Torreglosa, P. Garcia, L. Fernandez, and F. Jurado, “Predictive control for the energy management of a fuel-cell battery supercapacitor tramway,” *IEEE Transactions on Industrial Informatics*, vol. 10, no. 1, pp. 276–285, 2014.
- [35] W. S. Lin and C. H. Zheng, “Energy management of a fuel cell/ultracapacitor hybrid power system using an adaptive optimal-control method,” *Journal of Power Sources*, vol. 196, no. 6, pp. 3280 – 3289, 2011.
- [36] N. Sadegh, B. Khan, and J. Meisel, “Optimization of the fuel consumption of a parallel hybrid electric vehicle,” in *IEEE/ASME International Conference on Advanced Intelligent Mechatronics*, pp. 128–133, 2005.
- [37] J. Gao, F. Sun, H. He, G. Zhu, and E. Strangas, “A comparative study of supervisory control strategies for a series hybrid electric vehicle,” in *Power and Energy Engineering Conference*, pp. 1–7, March 2009.
- [38] P. Pisu and G. Rizzoni, “A comparative study of supervisory control strategies for hybrid electric vehicles,” *IEEE Transactions on Control Systems Technology*, vol. 15, no. 3, pp. 506–518, 2007.
- [39] O. Hegazy and J. Van Mierlo, “Particle swarm optimization for optimal powertrain component sizing and design of fuel cell hybrid electric vehicle,” in *Conference on Optimization of Electrical and Electronic Equipment*, pp. 601–609, 2010.
- [40] P. Thounthong and S. Rael, “The benefits of hybridization,” *IEEE Industrial Electronics Magazine*, vol. 3, no. 3, pp. 25–37, 2009.

- [41] P. Thounthong, S. Rael, and B. Davat, "Control strategy of fuel cell and supercapacitors association for a distributed generation system," *IEEE Transactions on Industrial Electronics*, vol. 54, no. 6, pp. 3225–3233, 2007.
- [42] Z. Amjadi and S. Williamson, "Power-electronics-based solutions for plug-in hybrid electric vehicle energy storage and management systems," *IEEE Transactions on Industrial Electronics*, vol. 57, no. 2, pp. 608–616, 2010.
- [43] X. Zhang, C. C. Mi, A. Masrur, and D. Daniszewski, "Wavelet-transform-based power management of hybrid vehicles with multiple on-board energy sources including fuel cell, battery and ultracapacitor," *Journal of Power Sources*, vol. 185, no. 2, pp. 1533 – 1543, 2008.
- [44] J. Hasikos, H. Sarimveis, P. Zervas, and N. Markatos, "Operational optimization and real-time control of fuel-cell systems," *Journal of Power Sources*, vol. 193, no. 1, pp. 258 – 268, 2009.
- [45] P. Garcia, L. Fernandez, C. Garcia, and F. Jurado, "Energy management system of fuel-cell-battery hybrid tramway," *IEEE Transactions on Industrial Electronics*, vol. 57, no. 12, pp. 4013–4023, 2010.
- [46] K. Jin, X. Ruan, M. Yang, and M. Xu, "A hybrid fuel cell power system," *IEEE Transactions on Industrial Electronics*, vol. 56, no. 4, pp. 1212–1222, 2009.
- [47] A. Phillips, M. Jankovic, and K. Bailey, "Vehicle system controller design for a hybrid electric vehicle," in *IEEE International Conference on Control Applications*, pp. 297–302, 2000.
- [48] L. M. Fernandez, P. Garcia, C. A. Garcia, and F. Jurado, "Hybrid electric system based on fuel cell and battery and integrating a single dc/dc converter for a tramway," *Energy Conversion and Management*, vol. 52, no. 5, pp. 2183 – 2192, 2011.
- [49] Y. Zhu, Y. Chen, Z. Wu, and A. Wang, "Optimisation design of an energy management strategy for hybrid vehicles," *Int. J. Alternative Propulsion*, vol. 1, no. 1, pp. 47–62, 2006.
- [50] Q. Zeng and J. Huang, "The design and simulation of fuzzy logic controller for parallel hybrid electric vehicles," in *IEEE International Conference on Automation and Logistics*, pp. 908–912, Aug 2007.
- [51] S. Caux, W. Hankache, M. Fadel, and D. Hissel, "On-line fuzzy energy management for hybrid fuel cell systems," *International Journal of Hydrogen Energy*, vol. 35, no. 5, pp. 2134 – 2143, 2010.

- [52] A. Rajagopalan, G. Washington, G. Rizzoni, and Y. Guezennec, “Development of fuzzy logic control and advanced emissions modeling for parallel hybrid vehicles,” technical report, NREL report, 2003.
- [53] P. Rodatz, G. Paganelli, A. Sciarretta, and L. Guzzella, “Optimal power management of an experimental fuel cell/supercapacitor-powered hybrid vehicle,” *Control Engineering Practice*, vol. 13, no. 1, pp. 41 – 53, 2005.
- [54] X. Liangfei, H. Jianfeng, L. Xiangjun, L. Jianqiu, and O. Minggao, “Distributed control system based on can bus for fuel cell/battery hybrid vehicle,” in *IEEE International Symposium on Industrial Electronics*, pp. 183–188, 2009.
- [55] G. Paganelli, T. Guerra, S. Delprat, J. Santin, M. Delhom, and E. Combes, “Simulation and assessment of power control strategies for a parallel hybrid car,” *Proceedings of the Institution of Mechanical Engineers Part D Journal of Automobile Engineering*, vol. 214, no. 1, pp. 705–717, 2000.
- [56] A. Sciarretta, M. Back, and L. Guzzella, “Optimal control of parallel hybrid electric vehicles,” *Control Systems Technology, IEEE Transactions on*, vol. 12, pp. 352–363, May 2004.
- [57] Z. Yu, D. Zinger, and A. Bose, “An innovative optimal power allocation strategy for fuel cell, battery and supercapacitor hybrid electric vehicle,” *Journal of Power Sources*, vol. 196, no. 4, pp. 2351 – 2359, 2011.
- [58] P. Garca, J. Torreglosa, L. Fernandez, and F. Jurado, “Viability study of a fc-battery-sc tramway controlled by equivalent consumption minimization strategy,” *International Journal of Hydrogen Energy*, vol. 37, no. 11, pp. 9368 – 9382, 2012.
- [59] R. Dinnawi, D. Fares, R. Chedid, S. Karaki, and R. Jabr, “Optimized energy management system for fuel cell hybrid vehicles,” *IEEE MELECON 2013 conference*, 2013.
- [60] A. J. Wood and B. F. Wollenberg, *Power Generation Operation and Control-2nd Ed.* Wiley New York, 1996.
- [61] R. Bellman, “Dynamic programming,” *Princeton*, 1957.
- [62] J. Rurgladdapan, K. Uthaichana, and B. Kaewkham-ai, “Li-ion battery sizing and dynamic programming for optimal power-split control in a hybrid electric vehicle,” in *International Conference on Electrical Engineering/Electronics, Computer, Telecommunications and Information Technology*, pp. 1–5, 2012.

- [63] E. Vinot, R. Trigui, Y. Cheng, A. Bouscayrol, and C. Espanet, “Optimal management and comparison of sp-hev vehicles using the dynamic programming method,” in *IEEE Vehicle Power and Propulsion Conference*, pp. 944–949, 2012.
- [64] L. Xu, M. Ouyang, J. Li, and F. Yang, “Dynamic programming algorithm for minimizing operating cost of a pem fuel cell vehicle,” in *IEEE International Symposium on Industrial Electronics*, pp. 1490–1495, 2012.
- [65] H. Dokuyucu and M. Cakmakci, “Concurrent design of energy management and vehicle stability algorithms for a parallel hybrid vehicle using dynamic programming,” in *American Control Conference (ACC), 2012*, pp. 535–540, 2012.
- [66] L. V. Prez, G. R. Bossio, D. Moitre, and G. O. Garca, “Optimization of power management in an hybrid electric vehicle using dynamic programming,” *Mathematics and Computers in Simulation*, vol. 73, no. 14, pp. 244 – 254, 2006.
- [67] C. Shen and X. Chaoying, “Optimal power split in a hybrid electric vehicle using improved dynamic programming,” in *Power and Energy Engineering Conference (APPEEC), 2010 Asia-Pacific*, pp. 1–4, 2010.
- [68] A. Boyali and L. Guvenc, “Real-time controller design for a parallel hybrid electric vehicle using neuro-dynamic programming method,” in *IEEE International Conference on Systems Man and Cybernetics*, pp. 4318–4324, 2010.
- [69] C. C. Lin, H. Peng, and J. Grizzle, “A stochastic control strategy for hybrid electric vehicles,” in *Proceedings of the American Control Conference*, vol. 5, pp. 4710–4715, 2004.
- [70] A. Schell, H. Peng, D. Tran, E. Stamos, C. Lin, and M. J. Kim, “Modeling and control strategy development for fuel cell electric vehicles,” *Annual Reviews in Control*, vol. 29, no. 1, pp. 159–168, 2005.
- [71] S.M.M. Ansarey and M. Shariatpanahi and H. Ziarati and M.J. Mahjoob, “Optimal Energy Management in a Dual-Storage Fuel-Cell Hybrid Vehicle using Multi- Dimensional Dynamic Programming,” *Journal of Power Sources*, vol. 250, no. 1, pp. 359–371, 2013.
- [72] “U.s. department of energy, energy efficiency & renewable energy eere information center,” *www.eere.energy.gov*, Feb, 2011.
- [73] J. Spendelow and J. Marcinkoski, “Fuel cell system cost 2013,” *DOE Fuel Cell Technologies Office*, October 16, 2013.

- [74] K. W. Suh and A. Stefanopoulou, “Coordination of converter and fuel cell controllers,” in *Proceedings of the 2005 IEEE International Symposium on Intelligent Control*, pp. 563–568, 2005.
- [75] F. Savoye, P. Venet, M. Millet, and J. Groot, “Impact of periodic current pulses on li-ion battery performance,” *IEEE Transactions on Industrial Electronics*, vol. 59, no. 9, pp. 3481–3488, 2012.
- [76] L. O. Valen and M. I. Shoesmith, “The effect of phev and hev duty cycles on battery and battery pack performance,” *Plug-in Highway Electric Vehicle Conference*, June, 2010.
- [77] H. Kohler, “Our commitment to commercialization of fuel cell vehicles and hydrogen infrastructure, fuel cells and hydrogen,” *Joint Technology Initiative, 3rd Stakeholders General Assembly*, www.fch-ju.eu 2010.
- [78] C. C. Lin, H. Peng, J. Grizzle, and J. M. Kang, “Power management strategy for a parallel hybrid electric truck,” *IEEE Transactions on Control Systems Technology*, vol. 11, no. 6, pp. 839–849, 2003.
- [79] Sanyo, “Overview of lithium ion batteries,” 2014.
- [80] A. E. Mehrdad Ehsani, Yimin Gao, “Modern electric, hybrid electric, and fuel cell vehicles: Fundamentals, theory and design,” *CRC*, vol. Second edition, 2010.
- [81] A. S. Lino Guzzella, “Vehicle propulsion systems,” *Springer*, vol. Second edition, 2007.
- [82] “Department of energy, doe hydrogen program record,” *United States of America*, 2010.
- [83] *Hydrogen Economy*, *Wikipedia The Free encyclopedia*, 2013.
- [84] “Swing 5300 rechargeable lithium-ion cell,” *Boston Power*, 2012.
- [85] “Battery prices for electric vehicles fall 14 percent,” *Bloomberg*, 2013.
- [86] “Cost of advanced lithium-ion batteries for evs,” *Treehugger*, 2013.
- [87] J. Bernard, S. Delprat, T. Guerra, and F. Bchi, “Fuel efficient power management strategy for fuel cell hybrid powertrains,” *Control Engineering Practice*, vol. 18, no. 4, pp. 408 – 417, 2010.
- [88] F. Panik, “Simulation studies concerning a fuel cell hybrid bus,” *SAE Technical Paper 2009-36-0402*, 2009.

- [89] I. Daubechies, “Ten lectures on wavelets,” *CBMS-NSF conference series in applied mathematics*, 1992.
- [90] S. Mallat, “A theory for multiresolution signal decomposition: the wavelet representation,” *IEEE Pattern Analysis and Machine Intelligence*, vol. 11, no. 7, pp. 674–693, 1989.
- [91] A. Martin, I. Iglesias, A. Goti, J. L. Calvo, and J. Valera, “Case study: Using the adaptable pxi test bench, we used model-based design methodology, which simplified and increased speed and efficiency of the prototyping and validation stages of the project using huil,” *Developing a Test Bench for a Design Based on a Hybrid Electric Vehicle Model*, National Instruments, 2013.
- [92] “Ballard power systems, <http://www.ballard.com/>,” *Putting Fuel Cells to Work*, 2014.
- [93] “Development, production and sales of battery systems, <http://www.hyliontec.com/imprint.html>,” *HylionTec*, 2014.
- [94] ETSYSTEM, “<http://www.et-system.de>,” *The world of power*, 2014.
- [95] Farnell, “<http://uk.farnell.com/>,” 2014.
- [96] Y. Murphey, J. Park, L. Kiliaris, M. Kuang, M. Masrur, A. Phillips, and Q. Wang, “Intelligent hybrid vehicle power control part ii online intelligent energy management,” *IEEE Transactions on Vehicular Technology*, vol. 62, pp. 69–79, Jan 2013.
- [97] D. Fares, S. Karaki, and R. Chedid, “Design and simulation of a hybrid renewable energy system,” in *IEEE Power and Energy Conference at Illinois (PECI)*, pp. 1–7, IEEE, 2011.